ETH zürich

PAUL SCHERRER INSTITUT
PSI

Developement of *operando* diagnostics for Li-ion cathodes by Raman spectroscopy

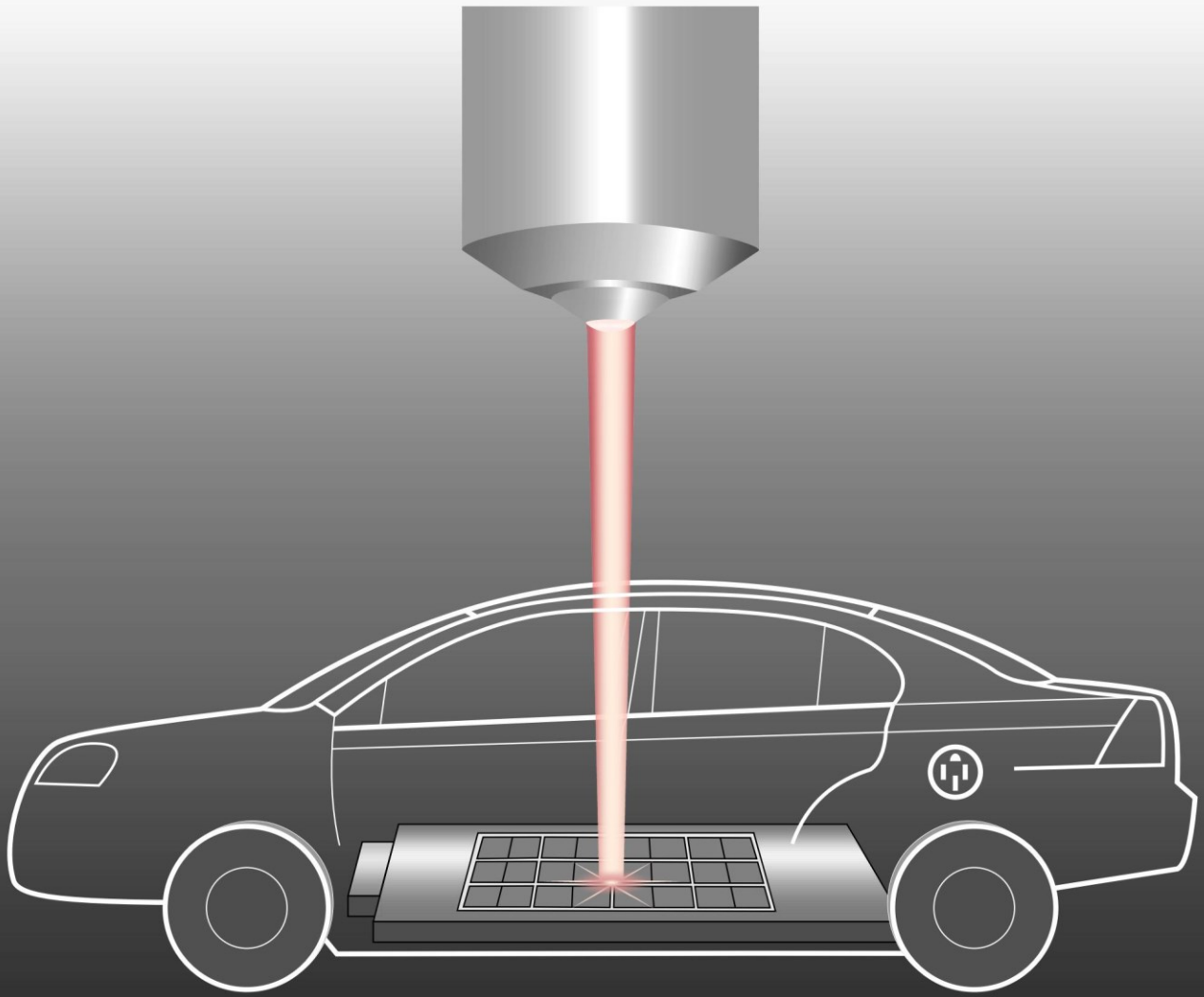

Eibar Joel Flores Cedeño

ETH Dissertation Nr. 26045

DISS. ETH NO. 26045

Development of operando diagnostics for Li-ion cathodes by Raman spectroscopy

A thesis submitted to attain the degree of

DOCTOR OF SCIENCES of ETH ZURICH

(Dr. sc. ETH Zurich)

presented by

Eibar Joel Flores Cedeño

M.Sc., Université de Picardie Jules Verne

born on 10 January 1990

citizen of Panama

accepted on the recommendation of

Prof. Dr. Petr Novák
Prof. Dr. Renato Zenobi
Prof. Dr. Erik J. Berg

2019

Dedicated to my family the Cedeño-Sánchez, especially to *mamita* Rosario.

"*No dejes camino real por vereda*"

Los tres consejos.

Acknowledgements

Hiking towards the end of this PhD has been at times challenging and exhausting, but also exciting and edifying. At the end, as in the Swiss Alps, the view from the top is overwhelming. The difficult trails seem smaller from afar but remind me of those who were close, offering a hand, teaching and encouraging. I am humbly grateful to all of them.

I firstly acknowledge the Swiss National Science Foundation (SNSF) under the "Ambizione Energy" scheme (Grant 160540) for funding.

I hold a deep gratitude to my supervisors, those with the map indicating the path. Thanks to Dr. Erik Berg who shared his knowledge, believed in my work and transmitted his ambition for searching scientific truth. With a balanced combination of scepticism and trust, Erik's supervision was instrumental for developing my research ideas and skills to complete this project successfully. Thanks to my doctoral father Prof. Dr. Petr Novák for the opportunity to work at PSI and for his excellent academic guidance. I am very grateful to Dr. Sigita Trabesinger for her selfless assistance during thesis writing and for her empathic and warm support.

Thanks to my collaborators who provided the technical assistance along the way up. Dr. Nathalie Vonrüti and specially Prof. Dr. Ulrich Aschauer are kindly acknowledged for their scientific contributions with DFT phonon calculations and fruitful (and fun!) discussions. The assistance from Mr. Hermann Kaiser, Dr. Aurelie Guéguen, Dr. Lucien Boulet-Roblin and Dr. Bing Sun are also acknowledged. I particularly appreciate the always friendly aid from Dr. Daniel Streich since my very first day at PSI.

I met many hikers aiming at the same cusp, which became valuable companions at different stages of the track. Because of them I had a great and stimulating working environment: Sebastian, Guilio, Hai-Jung, Minglong, Mario, Juliette, David, Laura Höltschi, Leiting, Steven and specially the Germans: Paul, Fabian, Max, Simon (Matlab) and Marta (si, anche tu). I was lucky for being surrounded by such a unique group of friendly, multicultural, open-minded and intelligent people. I enjoyed our conversations during coffee breaks and beer evenings, ranging from battery research and global socioeconomic issues, all the way down to lab gossips and awkward topics (my favourite). From them Leanza and Bolli became family: I am the most grateful to you two for your contagious good energy, advice and sincere friendship in the fun and difficult times.

With my social-mates and fitness-mates I resupplied the energies to keep going: Mark, Irene, Frankie, Vicky, Pablito, Muriel, Simon (hiking), Samuel (previously known as Samy), Mateusz, Joel, Laura Maurel, Ian, Ricardo. Thanks also to my friends back home Oscar, Manuel, Moyano, Samuel and Ingemary. Along the way we shared work-related frustrations, lazy board-game evenings, parties, mammoths, hikes, beer and with it both serious and foolish chats. I'm sure wherever I will be I will look back at this adventure and smile, treasuring all the fun moments we shared.

To my family in Panama: Les debo todo. Les dedico este trabajo porque culmina un sueño que ustedes me entrenaron para lograr y me convencieron de que era posible. Gracias a abuelita Margarita y a mama Elisa por todos todo su esfuerzo para sacar nuestra familia adelante y por transmitirnos el valor de la familia, de la humildad y la importancia de ser agradecido. A mis tíos Vlado, Juan-K., Lucho y más recientemente Yadira: gracias por cuidarme, enseñarme y hacerme reír; donde sea que estoy en el mundo el recuerdo de ustedes sentados a la mesa almorzando y compartiendo me sobrecoge. Mi más profunda gratitud será siempre hacia mi mamita Rosario. Con sus 15 horas al día de viaje y trabajo me ofreció mi educación, y su amor a tiempo completo me dio la convicción y el entusiasmo para superarme. Gracias mamita por sacarme a ver las estrellas, por hacerme curioso y por confiar en mí. Y a los nuevos miembros de mi familia Camila, Carlitos y Valentina: van a descubrir que el mundo que comienzan a vivir, desafortunadamente, no les debe nada. Pero ese mundo también está lleno de oportunidad, de lugares que descubrir, de metas que alcanzar. Ante el reto les testifico, ahora convencido, que los sueños se cumplen.

Debora, grazie a te in particolare per sostenermi, ascoltarmi, per avermi reso più forte e per aver deciso di condividere il tuo percorso con me. Tra vino, cibo, risate e musica sei diventata la migliore compagna di “escursioni” o meglio di avventure che potessi desiderare. Grazie a te ho incontrato una nuova famiglia in Italia: Marilena, Fabio, il piccolino Alessio, Luca, gli zii Anna, Sandro, Patri, Vittorio; principalmente Marialuisa e Roberto che mi hanno accolto, si sono presi cura di me e mi hanno voluto bene da subito come un membro della famiglia. Debora ti ringrazio profondamente per avermi insegnato che ogni avventura ha senso solo se si contempla la vista, e se il carico del viaggio e lo stupore della cima sono condivisi.

Abstract

The ever increasing demand for better-performing Li-ion batteries (LIBs) motivates substantial research efforts into the understanding of the working principles of every battery component, particularly of the cathode because it is the performance-limiting component in LIBs. The lithium-transition-metal oxides ($LiMO_2$) with layered structure are the state-of-the-art cathode active materials for LIBs but many aspects of their operation are not fundamentally understood and, thus, leave a room for significant improvements. From the large portfolio of techniques available for characterizing LIB electrodes, only a handful are capable of investigating the materials at the individual particle level and *operando*, i.e. within their working environment and while they operate. One of them is Raman spectroscopy, a versatile technique for studying condensed phases based on their intrinsic normal modes of vibration. Despite the advantages of this technique, it has been rarely applied to $LiMO_2$ due to multiple challenges related to the limitations of the *operando* measurements: the cell designs, the inherently weak Raman signals of the oxides, the limited time resolution and the lack of fundamental understanding about the origin of the spectral features.

This work reports the development of a new spectro-electrochemical cell and multiple data-analysis tools for recording and analysing the *operando* Raman spectra of electrode materials. A cell design, mindful of multiple optical and electrochemical constraints, yields a device enabling superior spectral quality, time resolution, and electrochemical performance comparable to commercial-like cells. Instead of analysing only few sample spectra, several Matlab-based routines have been developed for the automated analysis of all hundreds of spectra resulting from an *operando* experiment. The resulting trends are analysed as a function of the electrode potential and the state of lithiation (SOL) of the oxide during cycling. The developed methodology is applied for the investigation of several commercially-relevant $LiMO_2$ cathode materials, which are currently used in portable and automotive applications: $LiCoO_2$ (portable electronics), $LiNi_{0.33}Co_{0.33}Mn_{0.33}O_2$ (BMW electric vehicles), $LiNi_{0.6}Co_{0.2}Mn_{0.2}O_2$, $LiNi_{0.8}Co_{0.1}Mn_{0.1}O_2$ and $LiNi_{0.8}Co_{0.15}Mn_{0.05}O_2$ (Tesla electric vehicles).

The relationships between spectral features and material properties are established by comparing the experimental findings to various models, formulated based on crystallographic symmetry, classical electrodynamics, DFT calculations and complementary experiments. These spectrum–property relationships are utilized for supporting the accurate interpretation of the Raman spectra and their evolution during cycling, and in turn enable the identification of features intrinsic to the structure and dynamics of $LiMO_2$. The spectral trends reveal the occurrence and nature of structural and electronic phase transitions, surface reactions and degradation processes limiting the electrochemical performance of the oxide-based cathodes.

This work demonstrates the diagnostic capability of *operando* Raman spectroscopy for elucidating physical and electrochemical phenomena of LIB electrodes. The holistic approach towards cell development, data analysis and spectrum interpretation had enabled

establishing a methodology able to elucidate the properties and dynamics of electrode materials, which carries great potential for further investigating complex processes within the batteries, and for eventually formulating design principles and identifying new strategies for improving LIB performance.

Riassunto

La crescente domanda di batterie agli ioni di litio (LIBs) con prestazioni sempre migliori continua a motivare sostanziali sforzi nella ricerca dei principi di funzionamento di ogni componente della batteria, in particolar modo del catodo, a causa del suo ruolo decisivo nel limitare la prestazione complessiva di LIB. Gli ossidi di metallo di transizione e litio $LiMO_2$ con struttura stratificata sono i materiali attivi convenzionalmente usati per il catodo nelle LIBs, ma ci sono molti aspetti del loro funzionamento che rimangono sconosciuti e per cui si prospetta un margine di miglioramento. Dal vasto insieme di tecniche disponibili per caratterizzare elettrodi LIB, solo alcune sono in grado di indagare i materiali a livello di singole particelle e in *operando*, cioè all'interno del loro ambiente di lavoro e durante il loro ciclo. Uno di questi è la spettroscopia Raman, una tecnica versatile utilizzata per studiare le fasi solide in base ai loro modi di vibrazione caratteristici. Nonostante i vantaggi di questa tecnica, sono state riscontrate raramente applicazioni a $LiMO_2$ a causa di molteplici sfide legate alle limitazioni delle misure *operando*: il design delle celle, i segnali Raman intrinsecamente deboli degli ossidi, la risoluzione temporale limitata e la mancanza di comprensione sull'origine delle caratteristiche spettrali a livello fondamentale.

Questo lavoro riporta lo sviluppo di una nuova cella spettro-elettrochimica e degli strumenti di analisi dei dati utilizzati per registrare e analizzare in *operando* gli spettri Raman dei materiali che compongono gli elettrodi. Il design di una cella che tiene conto dei molteplici vincoli ottici ed elettrochimici risulta in un dispositivo che consente una qualità spettrale superiore, una migliore risoluzione temporale e prestazioni elettrochimiche paragonabili a quelle di tipo commerciale. Invece di focalizzare l'analisi unicamente su alcuni spettri campione, lo sviluppo di diverse routine basate su Matlab ha permesso l'analisi automatizzata di tutte le centinaia di spettri risultanti da un esperimento *operando*. Le tendenze spettrali risultanti sono state studiate in funzione del potenziale dell'elettrodo e dello stato di litiazione (SOL) dell'ossido durante il ciclo. La metodologia sviluppata è stata applicata per studiare diversi materiali catodici $LiMO_2$ già utilizzati in applicazioni portatili e automobilistiche: $LiCoO_2$ (elettronica portatile), $LiNi_{0.33}Co_{0.33}Mn_{0.33}O_2$ (veicoli elettrici BMW), $LiNi_{0.6}Co_{0.2}Mn_{0.2}O_2$, $LiNi_{0.8}Co_{0.1}Mn_{0.1}O_2$ e $LiNi_{0.8}Co_{0.15}Mn_{0.05}O_2$ (veicoli elettrici Tesla).

Le relazioni tra caratteristiche spettrali e proprietà dei materiali sono state stabilite confrontando i risultati sperimentali con vari modelli formulati sulla base della simmetria cristallografica, dell'elettrodinamica classica, dei calcoli DFT (teoria della densità funzionale) e di esperimenti complementari. Queste correlazioni sono state adoperate per supportare un'accurata interpretazione degli spettri Raman e la sua evoluzione durante i multipli cicli di litiazione/delitiazione, che a loro volta consentono l'identificazione di caratteristiche intrinseche della struttura e della dinamica di $LiMO_2$. Le tendenze spettrali rivelano il verificarsi di transizioni di fase strutturali ed elettroniche, reazioni superficiali e processi di degradazione che limitano le prestazioni elettrochimiche dei catodi a base di ossidi.

Questo lavoro dimostra la capacità diagnostica della spettroscopia Raman operando per chiarire i fenomeni fisici ed elettrochimici degli elettrodi LIB. L'approccio olistico verso lo sviluppo delle cellule, l'analisi dei dati e l'interpretazione dello spettro ha permesso di stabilire una metodologia in grado di chiarire le proprietà e le dinamiche degli elettrodi, che offre un grande potenziale per approfondire i processi complessi all'interno delle batterie e per formulare principi di progettazione e identificare nuove strategie per migliorare le performance di LIB.

Contents

Chapter 1 Introduction

Human-induced climate change is recognized worldwide as a major threat to the sustainability of mankind. Most countries have committed to reduce their CO_2 emissions below the limits where climate change becomes irreversible.[1] Accordingly, major economies are progressively shifting towards the use of renewable energy sources and electric mobility, technologies that rely on the storage of electrical energy.[2] Lithium-ion batteries (LIBs) are one of the best performing electrochemical energy storage systems available: they are the technology of choice for portable electronic devices, are increasingly used for stationary energy storage applications, and are now transforming the transportation sector by enabling the introduction of hybrid and electric vehicles.[3–5]

1.1 How Li-ion batteries work

A lithium-ion cell is built by stacking two electrode materials — an anode and a cathode — separated by a membrane wetted with an electrolyte. The cell is typically assembled in the discharged state, that is, with a Li-containing cathode material and a Li-free anode material. Most commercially-relevant Li-ion electrode materials operate by the intercalation mechanism, that is, the Li^+ intercalant is reversibly inserted/removed from particular sites of a host lattice (Figure 1.1).[6]

During charging — when electrical energy is stored — the Li-ion cell works as an electrolytic cell, that is, the external voltage drives the non-spontaneous (de)intercalation of Li^+ out of the cathode and their insertion into the anode. Simultaneously, the cathode oxidizes and the released electrons reduce the anode, so as to balance the variations on positively charged Li^+ and thus keep both electrodes charge-neutral. The electrolyte is chosen to be Li-conducting and an electronic insulator, such that Li^+ is transported through it but electrons are forced to travel via an external circuit.[7] During discharge — when electrical energy is retrieved — the Li-ion cell behaves as a galvanic cell: Li^+ spontaneously return to the cathode where there is a lower chemical potential, while the associated orderly flux of electrons through the external circuit represents the electricity produced.

Electrodes are fabricated as composites of active material, carbon conductive additives and a polymer binder to warrant a good electronic conduction and mechanical stability of the electrode. The particle size of active material and the resulting electrode morphology are carefully controlled in order to provide access to the electrolyte and to reduce the Li^+ diffusion path.[8]

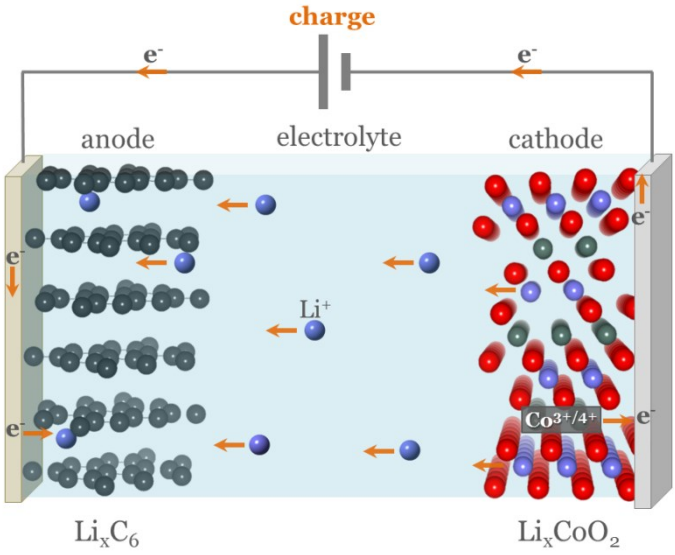

Figure 1.1. Schematic representation of a typical Li-ion cell during charge. The cell is a stack of a graphite anode, a $LiCoO_2$ cathode and a Li^+ containing electrolyte. The external voltage drives out Li^+ and electrons from the cathode into the anode. Electrons are released from the oxidation of cobalt in the cathode (Co^{3+} -> Co^{4+}).

Most research efforts today focus on the improvement of the cathode due to its decisive role in delimiting the overall LIB performance.[9] This is because, unlike the commonly used graphite anode, most cathode materials i) are constrained to operate using only a fraction of their theoretical specific charge to avoid degradation, thus becoming the limiting factor for the overall cell's energy density;[9,10] and ii) feature unstable interphases that reform in each cycle, irreversibly consuming Li^+, leaving deleterious side-products and resulting in a progressive decay of specific charge.[11–13] As a consequence, established and state-of-the-art cathode chemistries are being extensively researched in the search for enhanced chemical compatibility with the electrolytes and higher storage capacity delivered over longer lifetimes.[12,14]

1.2 Commercially-relevant cathode materials

The family of layered, stoichiometric transition metal oxides $LiMO_2$ offers the most attractive cathode materials for LIBs.[15] Their development was triggered after $LiCoO_2$ was found to reversibly react with Li^+ and was successfully commercialized for portable electronics applications.[14] Since then, several M substituted versions have been explored and higher capacity, higher operating voltage, longer lasting, and cheaper Li-ion cathodes have been developed. However, each layered oxide feature limitations inherent to its composition, electronic and atomic structure, and interfacial properties, which restrain their performance metrics and thus their suitability for a particular application.

$LiCoO_2$ (LCO). $LiCoO_2$ is rather easy to synthesize and features remarkable cycling stability if restricted to operate between 3.0 and 4.2 V *vs*. Li^+/Li. Within such limits LCO delivers ~150 mAh/g, which represents around half of its theoretical specific charge.[16] Cycling positive to 4.2 V triggers multiple undesired processes that, individually or collectively, result in the significant loss of specific charge and rapid cell death.[17–20] In addition to an inherently limited specific charge, the high cost and toxicity of cobalt make LCO unsuitable to be extensively produced for high–energy applications such as electric vehicles.

$LiNiO_2$ (LNO). A complete substitution of cobalt by nickel preserves the layered structure and enables Li^+ (de)intercalation; thus, $LiNiO_2$ was intensely investigated as an alternative to $LiCoO_2$, since the greater abundance of nickel promised a cheaper and more environmentally-benign cathode material.[21] More importantly, given its lower (de)intercalation potential $LiNiO_2$ delivers close to 200 mAh/g within the same 3.0–4.2 V window, a comparatively higher fraction of its theoretical specific charge.[22] However, accessing these high storage capacities requires synthesizing $LiNiO_2$ under carefully controlled conditions.[23] Even if a highly stoichiometric $LiNiO_2$ is successfully synthesized, the material features an inherent structural instability that results into a steep loss in specific charge during cycling.[24,25]

$LiNi_{0.8}Co_{0.15}Al_{0.05}O_2$ (NCA). The partial substitution of nickel by cobalt improves the structural stability and electrochemical reversibility of the oxide compared to the end members $LiCoO_2$ and $LiNiO_2$ but at the expense of reduced energy density.[26,27] In addition, aluminium incorporation as a non-redox active dopant enhances the power performance of the cathode material by reducing the cell impedance growth.[28] Extensive research into the Ni-Co-Al solid solutions found the $LiNi_{0.8}Co_{0.15}Al_{0.05}O_2$ (NCA) composition to offer the best trade-off between energy density and cycle life. NCA has been implemented by Panasonic and SAFT as Li-ion cathode material for electric vehicles (e.g., Tesla).[29] NCA cycles reversibly between 3.0 and 4.3 V *vs.* Li^+/Li delivering up to 215 mAh/g,[30,31] but its thermal instability on overcharge conditions is a major safety concern.[32–34]

$LiMnO_2$ (LMO): The use of manganese instead of cobalt and nickel could potentially yield a cheaper and more environmental-friendly cathode material. However, the synthesis of layered and stoichiometric $LiMO_2$ is difficult, and even if successful, the oxide is not able to preserve the layered structure after Li^+ deinsertion.[35,36] $LiMnO_2$ undergoes an irreversible phase transition to a spinel $LiMn_2O_4$ phase,[37,38] which features superior thermal stability in comparison to other layered oxides[39] but delivers low specific energy (140 mAh/g) that eventually fades due to structural and surface degradation.[40,41]

$LiNi_{1-a-b}Co_aMn_bO_2$ (NCM). The mixing of nickel, cobalt and manganese in $LiMO_2$ has been widely explored as a strategy for exploiting the beneficial traits of the end members, i.e. the high practical specific charge of $LiNiO_2$, the rate capabilities of $LiCoO_2$ and the improved

thermal stability of $LiMnO_2$.[42,43] The Ni-Co-Mn solid-solutions result into $LiMO_2$ oxides described by the general formula $LiNi_{1-a-b}Co_aMn_bO_2$, typically referred to as NCMs. The oxide with an equal Ni-Co-Mn proportion, $LiNi_{0.33}Co_{0.33}Mn_{0.33}O_2$ (NCM111), features superior cycling stability when limited to operate between a safe 3.0-4.3 V *vs*. Li^+/Li window, however, yielding a modest specific charge of 170 mAh/g.[44–46] Operation at higher voltages provides access to larger specific charge but at the expense of reduced cycling lifetime.[47]

Ni-enrichment serves as an alternative way for improving the specific charge supplied within safe voltage windows. More specifically, NCMs deliver more than 180 and 200 mAh/g when the nickel content is increased to 60% ($LiNi_{0.6}Co_{0.2}Mn_{0.2}O_2$ - NCM622) and 80% ($LiNi_{0.8}Co_{0.1}Mn_{0.1}O_2$ - NCM811), respectively.[45,48,49] Such improved energy outputs and the potentially cheaper manufacturing costs associated to lower cobalt contents situate the Ni-rich $LiMO_2$ as one of the most promising Li-ion cathode materials for automotive applications.[50]

The scientific and practical challenge of Ni-rich oxides — both NCA and NCMs — lies on stabilizing the safe delivery of high specific charge for lifetimes of technological relevance.[51,52] This is because when Ni composition approaches 100%, the oxides become increasingly susceptible to the same deleterious processes that lead to the irreversible degradation of LNO's electrochemical performance.[48,53,54]

1.3 Characterization of cathode materials

Major efforts on $LiMO_2$ research are directed i) to understand their fundamental working mechanisms, ii) to unravel the causes behind their degradation, and iii) to formulate and assess strategies to improve their electrochemical performance. To this end, it is necessary to accurately characterize these materials and their interfaces at multiple scales — in time and space — and in multiple conditions — before, during, after cycling.

Diffraction techniques are the most widely used since they provide comprehensive insights into the structural features of the oxides. $LiMO_2$ structures are firstly characterized using x-ray and/or neutron diffraction i) before cycling to assess the purity of the as-synthesized material, ii) during cycling to explore the (de)lithiation mechanism of the oxide, and iii) after multiple cycles to examine their long-term stability. In particular, advanced electrochemical cells enable recording diffraction patterns continuously while the material cycles, providing key insights into cycling-dependent phase transformations, the appearance of transient phases, and the growth of undesired (electrochemically inert) phases.[55,56] However, some other phases might be overlooked either because they are crystallographically indistinguishable or because they exist in highly localized domains. In addition, many functional and undesired processes have a minor influence on the long-range structure of the oxide and thus remain invisible to diffraction techniques.[55,57–59]

A more comprehensive exploration of $LiMO_2$ properties, cycling behaviour and stability is usually achieved by using complementary characterization techniques, monitoring the oxide's bulk electronic and coordination structures (e.g. X-ray absorption/emission/scattering and nuclear magnetic resonance), and its composition (e.g. electron spectroscopies) before, during and after cycling.[60–64] However, for commercial-like cells these advanced characterization techniques are mostly or solely applied *ex situ*, that is, the oxides are analysed before and/or after electrochemical cycling because of inherent experimental restrictions, such as sample preparation procedure, the destructive nature of the analytical probes, high vacuum and/or confined geometries.

Although *ex situ* measurements provide a first approach and often guide more specialized experiments, there are serious limitations. First, most dynamic information of processes occurring during cycling is lost due to thermodynamic relaxation of the oxides during sample preparation. Second, *ex situ* measurements carry an inherent risk of contamination and surface modification during transfer/washing. Last, composition-dependent *ex situ* measurements are constrained by how precise the preparation conditions and sampling intervals can be controlled and reproduced on various electrodes. Therefore, key features and processes of $LiMO_2$ are only reliably analysed when probing the material *operando*, that is, within its working environment and while it cycles.[65]

Figure 1.2 classifies conventional characterization techniques according to what they probe (single atoms, coordination environment, long-range ordering and morphology), their sampling level (sub-particle, individual particles or the whole electrode) and their suitability for *operando* studies using cells closely resembling the conditions found in commercial cells. For instance, diffraction techniques have been widely applied *operando* but only provide average electrode information, and are only sensitive to phenomena influencing the long-range order of the oxide. The short-range order and electronic structure at the particle and sub-particle levels can be explored with absorption spectroscopies and transmission electron microscopy, respectively; however, these techniques can be applied mostly *ex situ*.

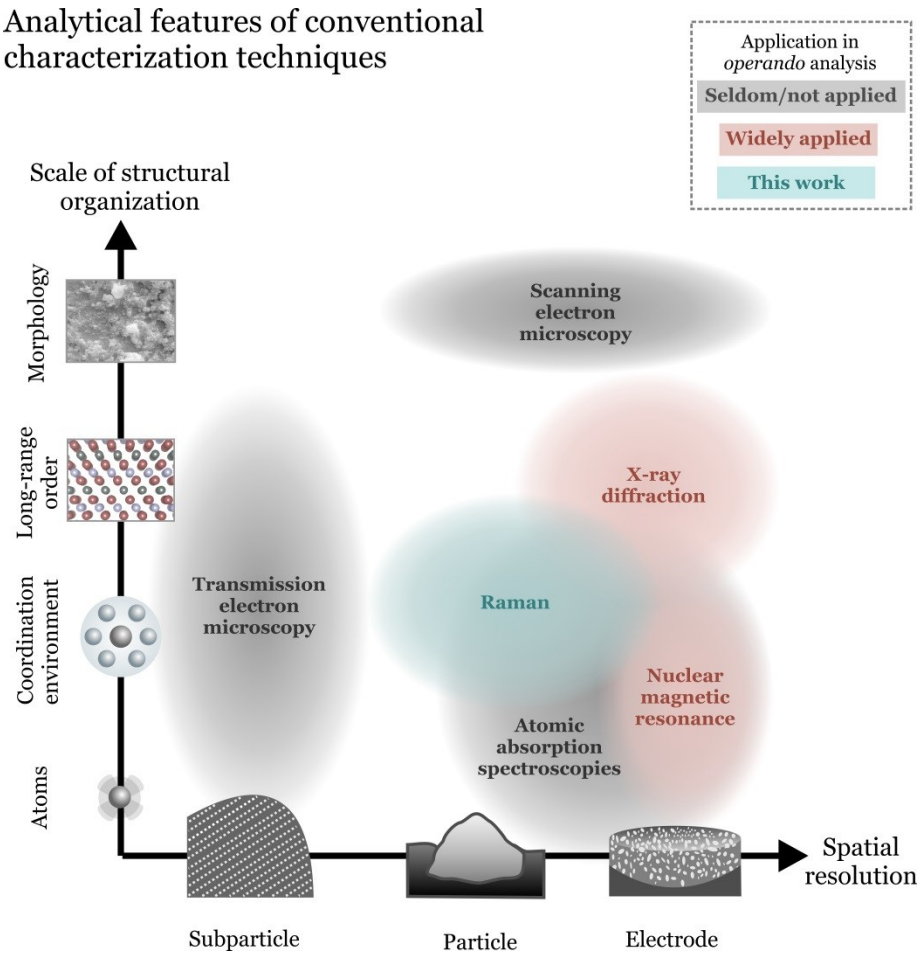

Figure 1.2. Analytical features of techniques conventionally used to characterize electrode materials for Li-ion batteries. The abscissa axis classifies the spatial resolution according to whether the techniques characterize the whole electrode, distinguish individual particles or resolve sub-particle features. The ordinate axis spans the levels of structural organization probed by the techniques. The colour code highlights those techniques that are widely used for *operando* characterization of electrode materials.

1.4 Raman spectroscopy: *operando* characterization of $LiMO_2$

Raman spectroscopy is a highly versatile technique, widely used to characterize electrode materials via their inherent atomic vibrations.[66] These vibrations are characteristic of $LiMO_2$ bonding and local structure. Furthermore, the optical nature of the analytical probe provides Raman spectroscopy with inherent advantages for *operando* and spatially-resolved characterization of electrode materials, including:

i. The analyte requires minimum sample preparation; hence, electrode materials can be characterized within their working environment.

ii. The light probe can be used non-destructively.

iii. Individual particles of the oxide within the composite electrode can be studied by coupling the spectrometer to an optical microscope with a (sub-) micrometre lateral resolution.

iv. The air and moisture sensitive cell components can be safely studied *operando* within gas-tight environments, since common window materials, transparent to visible light, can be implemented in the development of spectro-electrochemical cells.

v. The spectrum acquisition time scales available in standard instrumentation — in the order of seconds — enable sufficient time resolution.

vi. Strong infrared absorbers such as electrolyte solvents display moderate Raman signals and thus enable to discern vibrations from inorganic oxide particles.

Given the previously described experimental features, Raman spectroscopy sits in a unique place in the analytical landscape illustrated in Figure 1.2. First, its ability to resolve single particles permits the identification of spatial heterogeneities within the composite electrode. Second, its sensitivity to coordination environments complements the structural information derived from diffraction techniques and further reveals unexplored details about the material's local and electronic structure. Third, its suitability for *operando* characterization enables the investigation of processes inherently dynamic and within narrow intervals of Li^+ composition in Li_xMO_2.

Despite these advantages, *operando* Raman measurements on $LiMO_2$ have proven difficult due to multiple challenges limiting the descriptive power of the technique. To begin with, providing optical access to the cycling electrode is challenging, and often requires compromises in cell design leading to i) sub-optimal electrochemical performance that complicates the accurate estimation of Li^+ composition, and/or ii) poor spectral quality that makes band assigning and interpretation problematic. In addition, the Raman activity of most $LiMO_2$ materials is inherently weak, so recording high-quality spectra requires long exposure times that reduce time-resolution.

Even if the instrumental challenges are successfully addressed and the measurements yield time-resolved spectra, their individual data-treatment becomes an increasingly tedious task as the number of spectra per cycle increases. Hence, many researchers settle for analysing and reporting only a few sample spectra per cycle, at the risk of overlooking relevant phenomena occurring within narrow Li^+ composition intervals. Finally, the Raman features — number of bands, their frequencies, widths and intensities — are difficult to interpret given the manifold sources influencing the spectrum. In the absence of clear spectrum-property relations, most authors struggle to identify the fundamental origins of

the cycling-dependent spectral trends, and typically resort to phenomenological interpretations that might be inaccurate and/or not informative.[67]

1.5 Scope and structure of thesis work

The primary goals of this thesis work are i) to develop a reliable set of tools for recording, analysing and interpreting the evolution of the Raman spectra of electrode materials while they cycle within commercially-relevant conditions, and ii) to demonstrate the descriptive potential of the methodology by applying it to gain new insights into the cycling behaviour and degradation processes inherent to several commercially-relevant $LiMO_2$ cathodes for Li-ion batteries.

The properties of $LiMO_2$ (Chapter 2) and the basic principles of Raman spectroscopy (Chapter 3) are firstly reviewed, in order to layout the fundamental concepts guiding the development of the cell and the interpretation of the spectra. The developed cell, the data analysis tools and their application for *operando* Raman measurements are described in detail in Chapter 4. Chapter 5 presents a critical discussion into the interpretation of the spectra of fully-lithiated $LiMO_2$, focused on the implementation of physical models able to relate the spectral features to crystallographic and electronic structure of the oxides. The developed methodology and the established models are applied to acquire, analyse and interpret the Raman spectra of several $LiMO_2$-based cathodes while they cycle. In the remaining chapters, the cycling-dependent spectral trends of Li_xCoO_2 (Chapter 6), Ni-rich oxides (Chapter 7) and other NCMs (Chapter 8) are discussed. The main findings demonstrating the diagnostic capability of the technique are summarized in Chapter 9, along with proposed directions for future work.

Chapter 2 Physico-chemical properties of $LiMO_2$

2.1 Properties of the lithiated oxide

Most commercially-relevant $LiMO_2$ oxides share the same α-$NaFeO_2$ structure, best described by a rhombohedral lattice (Figure 2.1a) featuring the symmetry characteristics of the $R\bar{3}m$ (# 166) space group. In it oxygen atoms (6c sites) assemble into a face-centred cubic sublattice that accommodates both Li (3a) and M (3b) in octahedral sites, forming alternated layers. From a functional perspective, oxygen atoms build the stable framework hosting both the Li^+ intercalant and the redox-active species M. Since the oxygen sublattice is based on a hexagonal close-packed structure, it can be described as forming an ABC stacking.[6] Delmas et al. classify this structure as "O3", since Li occupy octahedral "O" sites in a unit cell that requires three "3" MO slabs for a complete description.[68]

The topological characteristics of the layered structure are ideal for a fast and reversible (de)insertion of Li^+. First, the 2D dimensionality of the layered structure enables fast Li^+ bulk diffusion compared to other structures featuring unidirectional and tridimensional diffusion paths.[69] Second, the MO_6 octahedra share edges and the resulting direct M-M interaction predicts high electronic conductivity.[70] Third, Li^+ can be (de)intercalated topotactically, i.e. without major modifications of the host structure.[71] Many transition metal oxides build lithiated layered oxide structures but only few of them are able to preserve it during cycling.[71] Mn, Co and Ni are of particular interest since they are not only structurally stable, but also feature low atomic weights that maximize the overall gravimetric energy density of the oxide-based battery.[43,72,73]

Given the conventional valences of Li (+1), O (-2), and the multivalent nature of M, the transition metal is formally considered to be in a trivalent state in the lithiated material and oxidize to a tetravalent state upon delithiation. However, this formal picture might not be accurate due to the quantum-mechanical nature of the electronic structure of the oxide. From a fundamental perspective, deintercalating Li^+ from $LiMO_2$ requires withdrawing electrons from its highest occupied electronic state, i.e. its Fermi level F_E. The electronic structure of $LiMO_2$ in the vicinity of F_E is predominantly shaped by the valence orbitals of M (*3d, 4s, 4p*) and O (*2s*). These atomic orbitals overlap with oxygen orbitals if they feature compatible symmetries and comparable energies. Note that not all M *3d* orbitals are equivalent in energy: the octahedral crystal field surrounding M split these orbitals into a three-fold t_{2g} orbital (d_{xy}, d_{xq}, d_{yz}) and a two-fold e_g orbital (d_{x2-y2}, d_{z2}); the t_{2g}-e_g^* energy gap is also known as the octahedral-field splitting gap Δ_O.[74] All these states assemble periodically in the lattice and result into the electronic band structure represented in Figure 2.1b.[75,76] Generally, the transition metal is significantly less electronegative than oxygen so the M-O interaction is largely ionic. As a consequence, bonding states have predominantly O-character while anti-bonding and non-bonding states

are mostly of M-character (Figure 2.1b).[77] The bonding states of all $LiMO_2$ are completely filled, so M-*d* electrons occupy the non-bonding t_{2g} and antibonding e_g^* states (Figure 2.1b). As a result, the particular valence electron count of M define the location of F_E,[75] and electron withdrawal from F_E — located at electronic bands of predominantly M-character — occurs via the oxidation of the transition metal, a picture well matching the formal description of transition metal redox.

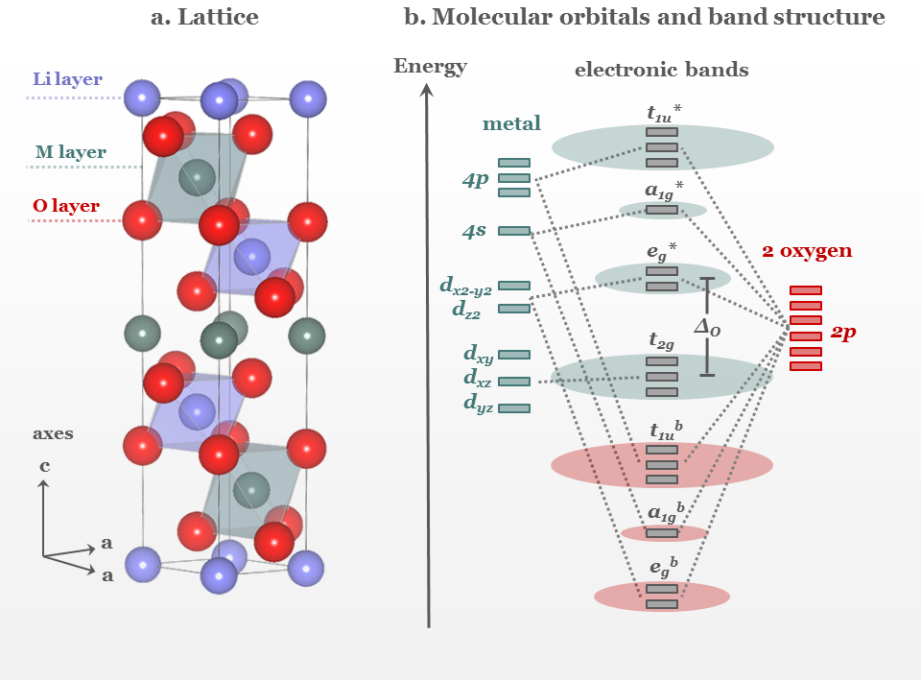

Figure 2.1. **a.** Schematic representation of the $LiMO_2$ unit cell, where Li (purple) oxygen (red) and transition metal (dark green) assemble into parallel layers forming a lattice described in the $R\bar{3}m$ space group. **b.** Atomic orbitals of M (dark green) and O (red) and the resulting band structure of the $LiMO_2$ oxide.[75,76] The bands are labelled with the Schoenflies notation according to their symmetry properties relative to the O_h point group.[74] The gap between t_{2g} and e_g^* states is denoted as the octahedral-field splitting gap Δ_O. Bonding bands have predominantly oxygen character (red ellipses) while non-bonding and antibonding bands feature transition metal character (green ellipses).

2.1.1 Valence electron count of M diversify the properties of $LiMO_2$

Given that most commercially relevant $LiMO_2$ share a common lattice structure, their properties and cycling behaviour differ due to their individual electronic configurations. For instance, Co^{3+} has 6 *d*-electrons that in $LiCoO_2$ assemble into a low-spin configuration fully occupying the three-fold t_{2g} band; this configuration is expressed as $[t_{2g}]^6[e_g]^0$ (the antibonding nature of the e_g^* band is implicit). In $LiNiO_2$ the formally-trivalent nickel (7 *d*-electrons) adopts a low-spin $[t_{2g}]^6[e_g]^1$ electron configuration. Since the e_g electron in $LiNiO_2$ is located at higher energy (easier to extract) than t_{2g} electrons in $LiCoO_2$, $LiNiO_2$ is expected and observed to be oxidized at lower electrode potentials.[78]

In addition, the $[t_{2g}]^6[e_g]^1$ configuration of $LiNiO_2$ is degenerate, i.e. the single electron located at the two-fold e_g can occupy two orbitals with the same energy. Degenerate ground states in non-linear molecules are unstable,[79] so these systems are predicted to undergo degeneracy removal mechanisms such as the Jahn-Teller distortion of the NiO_6 octahedron or charge disproportionation of Ni^{3+} into non-degenerate Ni^{2+} and Ni^{4+} species.[80] Therefore, the electronic configuration of Ni^{3+} causes intrinsic lattice instability in $LiNiO_2$.

The electronic configuration also determines the propensity of an oxide to involve oxygen in charge-compensation processes such as thermally-induced oxidation and (de)lithiation. First-principles calculations show that the *d*-orbitals of some transition metals align in energy to oxygen orbitals and provide significant oxygen character to the eg^* state in Figure 2.1b.[81] Hence, electron withdrawal could involve depletion of charge from oxygen atoms instead of the transition metal, if the degree of oxygen admixture of the bands at F_E is significant. In particular, the calculated electronic bands of $LiNiO_2$ at F_E feature a dominant oxygen character that explain its experimentally observed instability towards oxygen oxidation.[81–83]

In mixed transition metal oxides ($LiMO_2$ M=Ni, Co, Ni) each M contributes its own *d*-orbitals to the electronic structure of the material, and these orbitals differ in energy. Hence, electrons from one transition metal might be transferred to the empty orbitals of another transition metal lying at lower energy.[53,84] In $LiMO_2$ any M is formally expected to adopt a trivalent state; however, high-lying manganese orbitals transfer electrons to nickel such that the former adopts a tetravalent state while the latter a divalent state. As a result, Mn^{4+} and Ni^{2+} feature a one-to-one proportion for most nickel/cobalt/manganese compositions.[45,85,86]

2.2 Properties of the delithiated oxide: electrode potential

During charge, an external voltage drives the extraction of Li^+ from $LiMO_2$, which occurs simultaneously with the oxidation of the oxide to preserve electroneutrality. Likewise, the insertion of Li^+ into the anode is concomitant to its electrochemical reduction. Therefore, the cell voltage ΔU that electrons build at the ends of the external circuit is related to the chemical potential difference that Li^+ experiences in the two electrodes. Under equilibrium conditions:

$$\Delta U(x)_{Eq} = \frac{\mu_{anode}(x) - \mu_{cathode}(x)}{e} \qquad \text{Equation 2.1}$$

where e is the elementary unit of charge, μ the chemical potential of Li^+ in the electrode hosts (per mol of host) and x the fraction of Li^+ per mol of host. In general, both chemical potentials are a function of the host's Li^+ content x, hence ΔU varies in the course of the reaction and outlines a characteristic potential profile.[7]

Under non-equilibrium conditions — when (de)intercalation proceeds at non-zero rate — a fraction of the thermodynamic cell voltage defined in Equation 2.1 is consumed by multiple kinetic processes necessary to keep the cell operating at the reaction rate imposed. These deviations from $\Delta U(x)_{Eq}$ are called overpotentials (η in V), and are typically classified into ohmic, mass-transport and charge-transfer according to their origin. Overpotentials increase at higher cycling rates following distinct functional relations that are illustrated in Figure 2.2.[69,87] Since charging the cell requires $\Delta U_{charge} = \Delta U_{Eq} + \eta_{charge}$, and discharging delivers $\Delta U_{discharge} = \Delta U_{Eq} - \eta_{discharge}$, the charge-discharge curves feature an overpotential gap of magnitude $\Delta U_{charge} - \Delta U_{discharge} = \eta_{charge} + \eta_{discharge}$.[88]

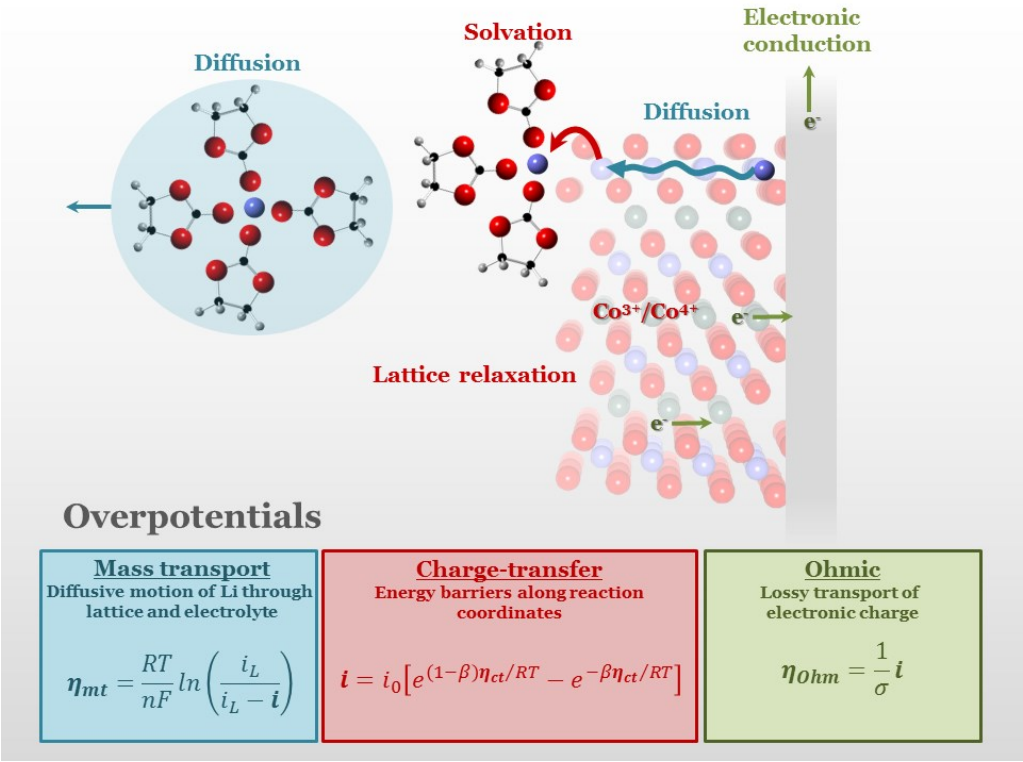

Figure 2.2. Origin of cell overpotentials. Mass transport overpotentials drive the diffusion of bare Li^+ through lattice sites and solvated Li^+ through the electrolyte. Charge-transfer overpotentials assist the overcoming of energy barriers associated to transferring Li^+ through the electrode-electrolyte interface, namely (de)solvation, lattice relaxation, transition metal redox, among others. Ohmic overpotentials drift electronic charges against deflective collisions within their path towards the electrodes.

2.3 Properties of the delithiated oxides: phase transformations

The properties of the host lattice (volume, lattice constants, electronic structure) unavoidably evolve during the extraction/insertion of the Li^+ intercalant. These transformations can be readily identified from the functional relation between the cathode's electric potential and Li^+ composition.

In experiments where lithium metal is used as anode and reference electrode ($\mu_{anode}(x)$ is constant), the variations in cell voltage originate exclusively from the cathode's electrode potential $E(x)$, and Equation 2.1 can be re-written as:

$$\Delta U(x)_{Eq} = -\frac{\mu_{cathode}(x)}{e} \equiv E(x) \qquad \text{Equation 2.2}$$

Equation 2.2 can be used to express the relation between the chemical potential of the cathode host to its Gibbs free energy g (per formula unit):

$$-eE(x) = \mu_{cathode}(x) = \frac{\partial g(x)}{\partial x} \qquad \text{Equation 2.3}$$

which means that the measurable $E(x)$ intercalation profile is proportional to the slope of the $g(x)$ function.[89]

2.3.1 Phase stability

An important consequence of Equation 2.3 is that $E(x)$ enables monitoring the stability of Li_xMO_2 against phase separation via its relationship with $g(x)$. A particular Li_xMO_2 composition will spontaneously separate into a fraction of $Li_\alpha MO_2$ and a fraction of $Li_\beta MO_2$, if the combined free energy of the two-phase system is lower than the free energy of the Li_xMO_2 one-phase (solid-solution) system. In other words, phase separation is favourable when:

$$g_{two-phase} < g_{sol}$$

$$\frac{(\alpha - x)}{\alpha - \beta} g(\alpha) + \frac{(x - \beta)}{\alpha - \beta} g(\beta) < g_{sol} \qquad \text{Equation 2.4}$$

where $g(\alpha)$ and $g(\beta)$ are the Gibbs free energies of $Li_\alpha MO_2$ and $Li_\beta MO_2$ composing the two-phase system, and g_{sol} the Gibbs free energy of the one-phase (solid-solution) Li_xMO_2 system.[90]

Figure 2.3a illustrates an example of functional variation of $g(x)$, where phase stability can be graphically assessed. In regions where g_{sol} is convex, every possible $g_{two-phase}$ line (left side of Equation 2.4) lies above g_{sol}, so Li_xMO_2 is stable against phase separation. In these regions Li^+ is completely miscible within the host, and (de)intercalation proceeds as a continuous phase transformation. Equation 2.3 anticipates that $E(x)$ will feature a smooth sloping curve (Figure 2.3b).[89,90]

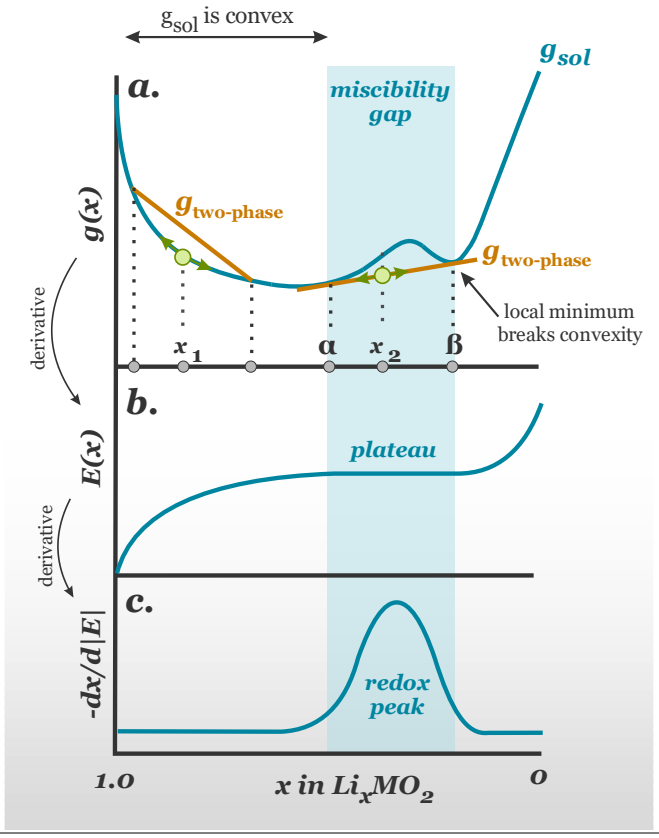

Figure 2.3. Phase stability of $LiMO_2$ as a function of Li^+ composition and its effects on common electrochemical observables. **a.** Functional variation of g_{sol} (blue profile). In compositional intervals where g_{sol} is convex (e.g. around x_1) the system stabilizes as a solid solution (green dot). In contrast, when a stable phase generates a local minimum able to break convexity, $g_{two\text{-}phase}$ lines below g_{sol} are possible, and so the system stabilizes as a set of two immiscible phases (e.g. around x_2). The two-phase coexistence interval —also known as miscibility gap — is set between the stable compositions α and β sharing a common tangent line. **b.** The electrode potential profile $E(x)$, proportional to the slope of $g(x)$ (Eqn. 2.3). In regions where $LiMO_2$ forms a solid solution (e.g. around x_1) the slope of $g(x)$ and so $E(x)$ evolve smoothly. Within the miscibility gap (e.g. $\alpha > x_2 > \beta$) the slope of $g(x)$ and the electrode potential remain constant. **c.** Differential charge profile highlighting plateau-like regions in $E(x)$.

In contrast, g_{sol} loses convexity when the presence of a particularly stable phase generates a local minimum. The loss of convexity implies the existence of a $g_{two-phase}$ line below g_{sol} (Figure 2.3a), predicting thus a spontaneous phase separation of Li_xMO_2. The stable compositions $Li_\alpha MO_2$ and $Li_\beta MO_2$ are those for which $g_{two-phase}$ (left side in Equation 2.4) is minimum, which graphically translates into finding the values α and β sharing a common tangent line. (De)intercalation through the $\alpha<x<\beta$ compositional region, also known as the miscibility gap, proceeds as a discontinuous (first order) phase transition. A key feature of the miscibility gap is that $g_{two\text{-}phase}$ depends linearly on x (left side in Equation 2.4), so its derivative, i.e. $E(x)$ in Equation 2.3, remains constant. In other words, the electrode's potential profile $E(x)$ features plateau-like behavior within regions of two-phase coexistence.[89–91]

The miscibility gap of intermediate phases is narrow, and so their corresponding plateaus can be difficult to discern in the potential profile. However, the fine structure of $E(x)$ can be clearly identified by computing its numerical derivative against lithium composition, where plateau-like regions of $E(x)$ appear as well-defined derivative peaks (Figure 2.3c).[6,92] The $E(x)$ derivative can be conveniently expressed as $-dx/d|E|$, since plateaus during charge and discharge are expressed as positive and negative peaks, respectively; hence, with this convention, the derivative profile becomes comparable to those from cyclic-voltammetry experiments.

2.3.2 Forces driving phase separation

In an ideal solid solution, g_{sol} is convex through the whole compositional range since it is solely influenced by the entropic contribution of Li^+ mixing. However, strong electrostatic and electronic interactions of Li^+ with the host (reflected in the enthalpy of mixing) stabilize the intermediates driving phase separation.[90] Ceder and Van der Ven noted that in $LiMO_2$ the physical origin of phase separation can be classified into:[93]

Configurational: When intralayer Li^+–Li^+ interactions are strong, Li^+ and its vacancies tend to assemble into ordered configurations that minimize their electrostatic repulsions. At certain compositions x, the energy benefit of ordering drives phase separation into ordered/disordered phases with distinct Li^+ configurations.[94,95]

Electronic: dilute concentrations of Li^+ vacancies promote the localization of electron holes in the host and this interaction, if strong, stabilize an intermediate insulator phase.[96] In addition, transition metals undergoing degeneracy removal mechanisms (e.g. low-spin Ni^{3+}, high-spin Mn^{3+}) promote atomic distortions that might become cooperative and result in the growth of lower-symmetry versions of the $LiMO_2$ lattice.[80]

Structural: Lithium ordering and other atomic interactions might drive displacive rearrangements of the sublattice host, stabilizing phases with stacking sequences other than the ideal ABC stacking of the $R\bar{3}m$ structure .[93,97]

The presence of regions with two-phase coexistence in the compositional landscape of Li_xMO_2 might have deleterious consequences on its electrochemical performance. For instance, cycling Li_xMO_2 through thermodynamically different phases requires surpassing consecutive energy barriers that slow down the kinetics of the intercalation reaction.[98] More importantly, the discontinuous nature of these phase transitions implies severe and potentially irreversible lattice changes, which are detrimental for the long-term stability of the electrode material.[99]

2.4 Irreversible degradation of electrochemical performance

The general aspects of $LiMO_2$ and its cycling serve as a starting point for understanding the mechanisms degrading their electrochemical performance. Degradation embodies all the undesired processes that result into the progressive and irreversible loss of specific charge, increased cell impedance and the risk of thermal runaway. These processes are highly interrelated, so it is difficult to establish their relative contributions to the decline of electrochemical performance, but for conceptual purposes they are separated in the literature according to their fundamental origins.[99–101]

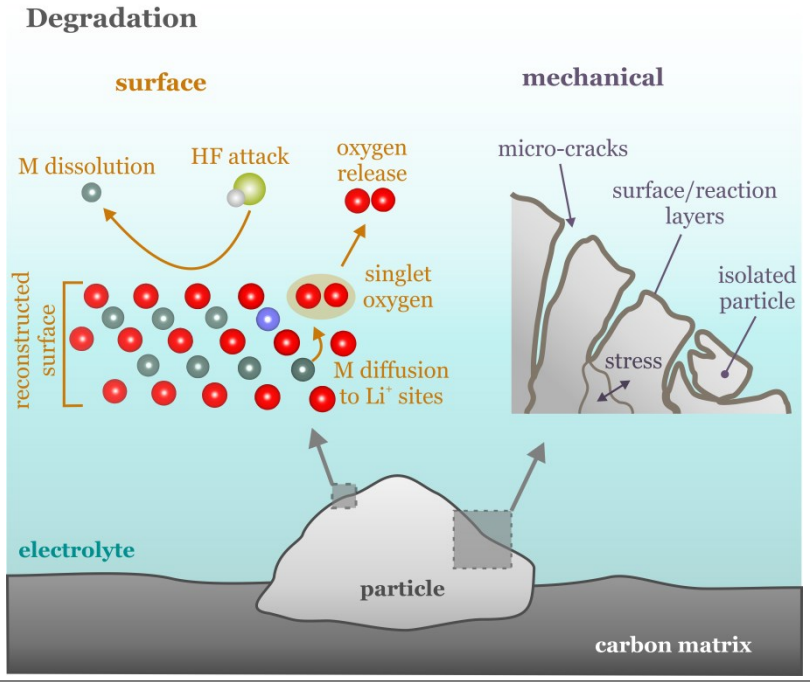

Figure 2.4. Representation of the main processes leading to the degradation of $LiMO_2$.

2.4.1 Surface reconstruction and oxygen oxidation

On delithiation of the layered structure, M tends to diffuse and occupy the lithium sites left vacant. When the proportion of these anti-site defects becomes significant the lattice transforms to spinel and/or rock-salt phases. Even if thermodynamically favourable, these transformations are kinetically hindered in the oxide's bulk by the sluggish diffusion of trivalent transition metals.[102] However, oxygen atoms at the oxide's surface — left unstable due to their participation in charge compensation — can easily escape the lattice and electrochemically reduce the transition metals. The resulting M^{2+} cations, more mobile than their trivalent counterparts, readily diffuse to vacant lithium sites and drive the structural transformation of the layered phase at its surface (Figure 2.4).[82,103]

The consequences of this process are two-fold. First, the oxides develop reconstructed spinel and rock-salt surfaces that block electron conduction and lithium diffusion, and result in an overall increase of electrode impedance. Second, the released oxygen species react with the electrolyte yielding i) by-products that consume Li^+ irreversibly and ii) heat potentially triggering thermal runaway.[82,83,104,105]

Ni-rich oxides are particularly susceptible to those processes since divalent nickel easily diffuses to vacant lithium sites due to their comparable Shannon radii ($r_S[Ni^{2+}]$=69 pm, $r_S[Li^+]$=76 pm).[106,107] At the particles surface, these $[Ni_{Li}]^\bullet$ point defects (expressed in Kroger-Vink's notation[108]) are coupled with oxygen release and surface reconstruction.[103] In the bulk, $[Ni_{Li}]^\bullet$ impede Li^+ diffusion through the lattice.[109] Moreover, the significant hybridization of oxygen and Ni bands at F_E predicts instability against oxygen oxidation and release it from the lattice.[81]

2.4.2 Reactions with electrolyte

The reactivity at the cathode-electrolyte interface is believed to be mostly triggered by HF left from the hydrolysis of the electrolyte's anion and other F-containing species.[110,111] HF attacks the electrode surface, dissolving transition metal species and forming Li-consuming reaction layers.[111] The electrode surfaces might also oxidize the electrolyte electrochemically via multiple electron transfer processes, resulting in organometallic M complexes soluble in the electrolyte.[112] In addition, the oxygen species lost from the lattice can be highly reactive and trigger further decomposition of the electrolyte (Figure 2.4).[113,114]

These deleterious processes introduce many undesired consequences to electrochemical performance. First, the reaction products are unstable and reform continuously, hence irreversibly consuming Li^+ cycle after cycle and leading to capacity fade. Second, these undesired products form layers that are potentially Li-blocking, impeding Li^+ diffusion and increasing the cell's impedance. Furthermore, the reaction products might trigger the same deleterious processes on the anode side, since the dissolved transition metals diffuse there and diminish the ability of the counter-electrode to form a stable interphase. Last, the gaseous products and heat released from these reactions increase the risk of triggering the violent decomposition of the cell.

2.4.3 Mechanical deterioration

Both continuous and discontinuous phase transformations that $LiMO_2$ experiences during cycling are accompanied by periodic volume changes that introduce internal stresses within the particles of active material. These stresses build up from highly anisotropic volume changes,[48,115] coherency strains at miscibility gaps,[99] surface reconstruction[116] and concentration gradients resulting from high-rate cycling.[31,117] Stresses are then relieved by

the formation of dislocations and, eventually, particle fragmentation (Figure 2.4). As a consequence, the specific charge of the active material is irreversibly lost when cracked particles — electrically insulated from the electrode matrix — become electrochemically inactive. Also, the freshly-created surfaces endure further surface reconstruction and reactions with the electrolyte, along with the corresponding deleterious effects already discussed.[48,118,119]

Mechanical deterioration is the leading cause degrading the performance of LCO when cycled above 4.2 V. At *x*=0.5 LCO undergoes a configurational phase transition accompanied by the monoclinic distortion of the lattice,[17] which causes the mechanical fracture of particles of active material and the irreversible loss of specific charge.[115,119] Similarly, LNO and Ni-rich oxides undergo a phase transition at *x*=0.2 accompanied by the abrupt contraction of the rhombohedral lattice along the *c*-axis.[47,120] The mechanisms driving the phase transition are still poorly understood, but the anisotropic nature of the volume change introduces mechanical strain and failure of the particles,[118] leading ultimately to rapid capacity fading during cycling.[48]

2.5 Summary

Most commercially-relevant $LiMO_2$ cathode materials share a common layered structure described in the $R\bar{3}m$ space group, which enables fast and reversible Li^+ (de)intercalation. The electronic structure of the oxide is mostly defined by the valence electron count of the transition metal, and influences the electrode potential, the charge compensation mechanism and predicts intrinsic structural instabilities. Once Li_xMO_2 is cycled, its electrode potential follows a characteristic $E(x)$ curve determined by the thermodynamics of the intercalation reaction and influenced by kinetic processes. $E(x)$ is the foremost indicator of the (de)intercalation mechanism of $LiMO_2$, since plateau-like regions in the potential profile occur within Li^+ compositions where Li_xMO_2 separates into two stable phases. Phase separation of Li_xMO_2 is driven by configurational, electronic and structural effects, and (de)lithiation through these miscibility gaps proceeds as a first-order phase transition. First order phase transitions, among other properties of $LiMO_2$, predict their susceptibility to undergo multiple and highly interrelated side-processes that result in capacity fading, impedance increase and risk of thermal runaway. The existence of miscibility gaps, changes in electronic structure, undesired chemical species and structural deterioration are all potential indicators of degradation phenomena.

Chapter 3 Basic principles of Raman spectroscopy

Raman spectroscopy is a technique to study the atomic vibrations of matter via the influence these vibrations have in scattered electromagnetic radiation. The properties of atomic vibrations are determined by the geometric arrangement of atoms and the interatomic forces keeping atoms together. Hence, a comprehensive analysis of monochromatic light scattered from a sample provides information about the content, state and dynamics of the sample. The basic concepts of vibrations are here presented, followed by a description of how these vibrations interact with electromagnetic radiation via the Raman scattering effect. Last, the Raman spectrum is introduced as a tool for studying the Raman interaction and identifying fundamental properties of the sample.

3.1 Vibrations

3.1.1 Classical description

Vibrations are periodic displacements of atoms around their equilibrium coordinates. At non-zero temperature atoms move disorderly due to thermal motion. As atoms form bonds, their thermal motion is restored by the interatomic interactions keeping them together (e.g. covalent, coulombic, Van der Waals interactions, etc.). Hence, atoms continuously oscillate around their equilibrium positions. Atomic vibrations feature characteristic amplitudes (how far atoms move), frequencies (how many oscillations per second), and energies, determined by the way the interatomic potential energy V reacts to the displacement q of atoms. For these complex interactions V can be treated analytically by applying a Taylor expansion series near the equilibrium position of atoms $q = 0$, which, for small displacements, can be truncated in the quadratic term. As a result, the potential energy can be modelled as a simple harmonic oscillator: [121]

$$V(q) = \frac{1}{2}\left(\frac{d^2V}{dq^2}\right)_0 q^2 \equiv \frac{1}{2}kq^2 \qquad \text{Equation 3.1}$$

where the constant k is the second derivative of the potential energy at $q = 0$. Graphically this means that the potential energy of atoms at the vicinity of $q = 0$ is parabolic (Figure 3.1a), and thus exhibits the Hook-type behaviour characteristic of simple springs.[122] The constant k — also called spring constant — represents the steepness of the potential energy well around $q = 0$ (Figure 3.1a), and measures how rigidly the spring-like force restores atomic motion.

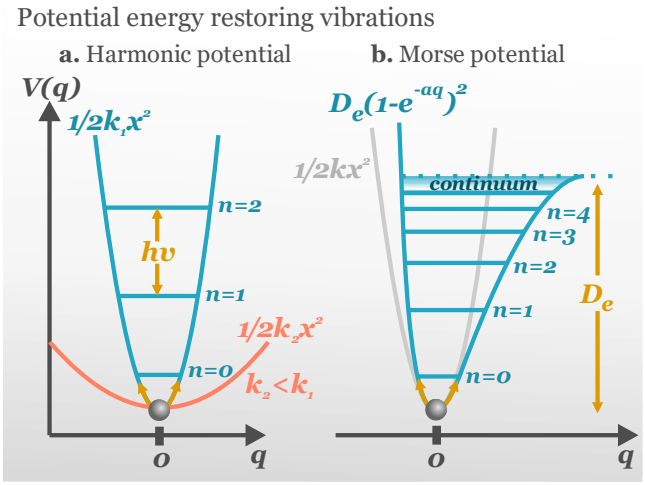

Figure 3.1. Potential energy restoring atomic vibrations. **a.** The harmonic potential features a parabolic shape around the equilibrium position characterized by a constant k. Smaller k values render wider parabolas that restore displacements loosely. The quantized energy levels n_1, n_2, n_3... are equally spaced from each other by $h\nu$. **b.** Morse potential describing analytically deviations from the harmonic approximation. The energy levels become less spaced from each other as n increases. The constant D_e represents the dissociation energy of the bond.

Solving the equations of motion based on the potential energy in Equation 3.1, results in an oscillation frequency ν_m that is related to the atom's mass m and the steepness of the parabolic potential energy well k according to:

$$\nu_m = \frac{1}{2\pi}\sqrt{\frac{k}{m}} \qquad \text{Equation 3.2}$$

Equation 3.2 implies that light atoms restored by stiff potentials vibrate at high frequencies. The classical description of vibrations is limited because atoms are not allowed to change their vibrational energy to any arbitrary value, as predicted by Equation 3.1. Instead, vibration energies are constrained to change in discrete steps called quanta.[123] Therefore, vibrations need to be described quantum-mechanically.

3.1.2 Quantum mechanical description

In the quantum-mechanical description of vibrations, the classical harmonic oscillator is redefined as finding the quantum-mechanical wavefunction satisfying the Schrödinger equation for a harmonic potential. Solving the equation with appropriate boundary conditions results in vibrational energies that increase in integer n steps according to:

$$E = \left(n + \frac{1}{2}\right) h\nu_m \qquad \text{Equation 3.3}$$

where h is Plank's constant and n *(*$n = 0,1,2,3 \ldots$) defines the vibrational energy levels (Figure 3.1a). Equation 3.3 has two main implications. First, in the lower, fundamental energy level ($n = 0$*)* vibrations still carry an energy $E = 1/2\, hv_m$, which is a consequence of the uncertainty principle. Second, energy levels are equally spaced in hv_m energy steps. Transitions to these higher vibrational levels ($\Delta n > 1$) might result in overtone bands.[124]

3.1.3 Vibrations in real systems

The assumptions leading to Equation 3.2 and Equation 3.3 might fail in real systems due to multiple reasons. First, vibrations in many-body systems involve a collection of atoms that interact with each other; hence, the mass m used in Equation 3.2 is replaced by an effective mass and the modes are treated with weighted displacement coordinates.[7] Second, when atomic displacements are large they experience non-parabolic potentials, i.e. they become anharmonic. As a consequence, the vibrational energy levels are no longer defined as in Equation 3.3. The anharmonic potential energy can be modelled using a Morse potential (Figure 3.1b), which accounts for experimentally observed phenomena associated to anharmonicity, namely the fact that the overtone frequencies are not equally spaced and the possibility of bond dissociation at large atomic displacements (Figure 3.1b).

3.2 Normal modes

The apparently random vibrations of large systems can always be described as a superposition of simpler vibrations called normal modes. A normal mode is an independent vibration (i.e. it is not influenced by other vibrations), where all atoms involved move in phase and at the same frequency.

3.2.1 Number of normal modes

An ensemble of a number *N* of bonded atoms (like in molecules and condensed phases) cannot translate in space independently, as the motion of each atom is constrained to keeping constant their average bonding distances. Instead, bonded systems can be translated as a whole in the three spatial directions (3 translations) and rotated as a whole around the three perpendicular axes (3 rotations, 2 for linear molecules). The remaining *3N-6* degrees of freedom (*3N-5* for linear molecules) manifest as normal modes of vibration.

3.2.2 Properties of normal modes

Each normal mode features a distinctive displacement pattern that can be represented as a set of vectors, determining which atom moves and where to. In addition, each normal mode oscillates at a characteristic frequency and associated energy determined — in first approximation — by Equation 3.2 and Equation 3.3, respectively. In some cases two or more

normal modes oscillate at the same frequency because they involve displacing the same atoms against similar interatomic forces. These normal modes are said to feature degenerate frequencies. In addition, normal modes are being constantly promoted to higher/demoted to lower energy states (Figure 3.1) as atoms exchange kinetic energy. Hence, the probability p_m of finding a normal mode at a particular energy level with frequency v_m depends on the temperature T of the system, subjected to a Boltzmann distribution (k_B is the Boltzmann constant):

$$p_m \propto e^{-hv_m/k_BT} \qquad \text{Equation 3.4}$$

3.2.3 Symmetry-based classification of normal modes

The properties of normal modes depend on the geometric arrangement of atoms, so symmetry becomes crucial for describing and predicting displacement patterns.[125] The symmetry of a material is the property of its particular atomic arrangement to remain invariant under geometrical operations (e.g. rotation around an axis, reflection from a plane, inversion through a point, etc.). The set of symmetry operations that leave the atomic arrangement invariant constitute a mathematical group.

Point groups are the most widely used tool to describe systems with no translational repetition (i.e. molecules), and provides an approximated description of systems that repeat in space, like crystals. Point groups are ensembles of operations that leave a point (the centre of mass) fixed. The crystallographic restriction theorem[126] confines to 32 the number of possible crystallographic point groups and each is commonly labelled using the Schoenflies notation.[125,127]

Point groups enable a categorization of the displacement pattern of a normal mode according to how the pattern transforms under the symmetry operations of the group. The categories are called symmetry species, and the way each of them transforms under the operations is represented with numerical indexes denoted as characters. The symmetry species are represented by Mulliken symbols that carry information about i) the behaviour of the species with respect to some operation (either symmetric: leaves sign/direction unchanged, or antisymmetric: changes sign/direction), and ii) the symmetry degeneracy of the species, i.e. the number of functions (vectors/wavefunctions) with the same symmetry (see table 4-6 from reference[125]). All the properties defining the point group — its symmetry operations, elements, species and characters — are summarized in a character table.[125,127]

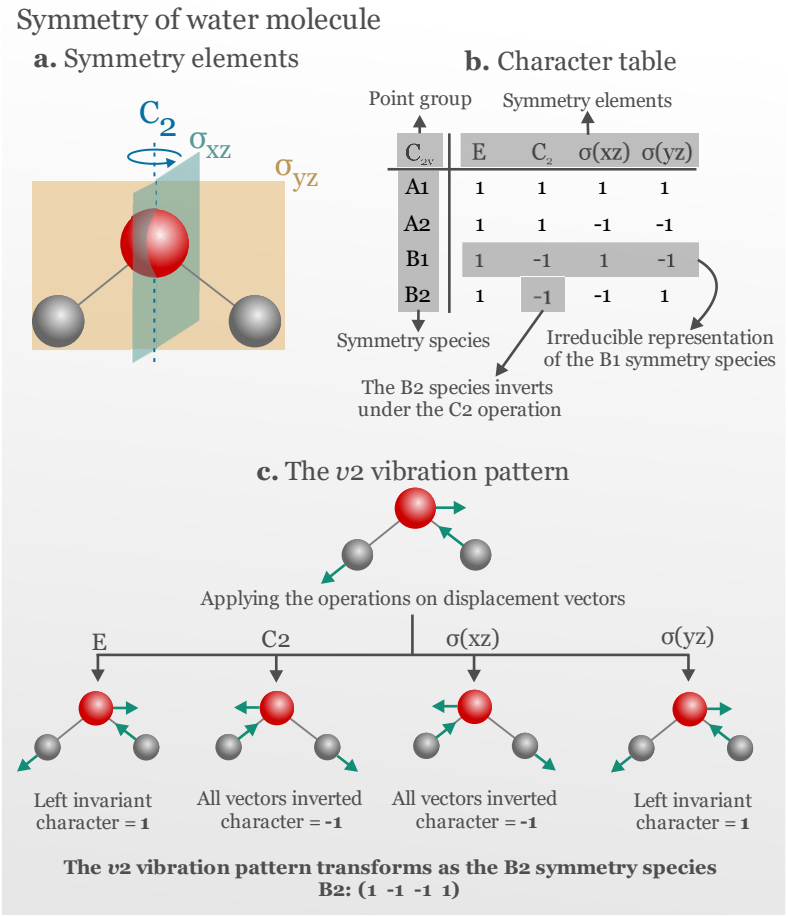

Figure 3.2. The symmetry properties of a water molecule. **a.** The spatial arrangement of the water molecule remains invariant under i) the identity operation *E*, ii) a 180° rotation C_2 around an axis passing through the oxygen atom and the centre of mass, iii) a reflection from a plane *σ(xz)* bisecting only the oxygen atom and the centre of mass, and iv) a reflection from a plane *σ(yz)* bisecting all atoms. As a consequence, the symmetry of water is described by the C_{2v} point group. **b.** The character table summarizing the symmetry properties of the C_{2v} point group. The table features the symmetry elements of the group, its symmetry species and the characters representing how those species transform under the operations associated to the symmetry elements. An irreducible representation is the set of simplest characters needed to fully describe the effects of each operation on a particular symmetry species. **c.** Analysing the symmetry of the ν_2 vibrational mode of water. The displacement vectors of the ν_2 normal mode of water are operated by each symmetry element of the group, and characters are assigned according to whether the vectors are inverted (character =-1) or they remain invariant (character = 1). By comparing the characters of each operation with the symmetry species in the character table, it is concluded that the ν_2 mode transforms according to the B2 symmetry species of the C_{2v} point group.

As an example, the symmetry properties of a water molecule are illustrated in Figure 3.2. The symmetry of water is described by the C_{2v} point group (Figure 3.2a), and all its corresponding symmetry properties are summarized in the character table (Figure 3.2b). This information is enough to characterize any possible displacement pattern of the atoms in the water molecule. To this end, the effect of each operation in particular displacement pattern is analysed and compared to the symmetry species of the point group. The example

in Figure 3.2c shows that the v_2 vibration of water transforms according to the B2 symmetry species. The mathematical framework of group theory enables to decompose any arbitrary set of displacement vectors of a molecule into the set of independent, symmetry-adapted displacement patterns that best describe the normal modes of vibration.

3.2.4 Vibrations in condensed phases

When molecules assemble to form larger units and condensed phases (e.g. liquids, solids), some normal modes remain localized and independent, i.e. involve only a small group of neighbouring atoms that are not affected by the environment. This is the case of vibrations from highly discrete molecular units (e.g. functional groups in an organic molecule) that are loosely coupled to the rest of the molecule. The vibrations of these units are identifiable in complex molecules, liquids and solids independently of the degree of structural ordering. In contrast, some other normal modes are influenced by the interactions and geometry of their complex environments. As a consequence, the point group symmetry is perturbed, and the frequency of the modes might shift and distribute broadly over an average value. In crystals, the translational periodicity enables some normal modes to couple to the motion of multiple neighbouring atoms, giving rise to phonons, i.e. collective vibrations that extend over the whole crystal lattice.[128]

The prediction and classification of normal modes in crystals require considering their translational symmetry elements in addition to the ones described in section 3.2.3; hence, their symmetry properties — and those of their normal modes — are described by space groups. However, the normal modes in crystals can be approximately evaluated from the symmetry features of an individual unit cell. To this end, the translational symmetry elements (glide planes and screw axes) belonging to the space group are omitted from the analysis, leaving a residual factor group. Crystallographic factor groups have a one-to-one correspondence (i.e. are isomorphic) to the 32 point groups; hence, the symmetry properties of normal modes in crystals can be classified using point groups in a similar manner as in section 3.2.3.[129,130] The factor group of each space group can be found in table 1.2 from reference [131]. The factor group analysis of a $LiMO_2$ crystal will be described in more detail in section 5.1.1.

Another feature of vibrations in crystals is the presence of soft vibrational modes. During the so-called displacive phase transitions, the lattice deforms to adopt the geometry of the new phase. The geometry change originates from the weakening of the interatomic forces keeping the initial phase together. If the deformation proceeds following the displacement pattern of a normal mode, the restoring forces of this mode are also weakened. As a consequence, the frequency of the normal mode — the soft vibrational mode — quickly decreases until reaching zero at the phase transition.[132]

3.2.5 Interactions of normal modes with electromagnetic radiation

Electromagnetic radiation travels as a wave of electric and a magnetic fields, oscillating perpendicular to the direction of propagation. The interaction of these fields with matter results in three main effects. First, radiation can be absorbed when the fields impart momentum and kinetic energy to electric charges, currents and magnetic spins existing in the material. Second, the radiation can induce electric dipoles that re-emit those fields in all directions; this process is known as scattering. Alternatively, in the absence of any interaction, radiation is transmitted unchanged.

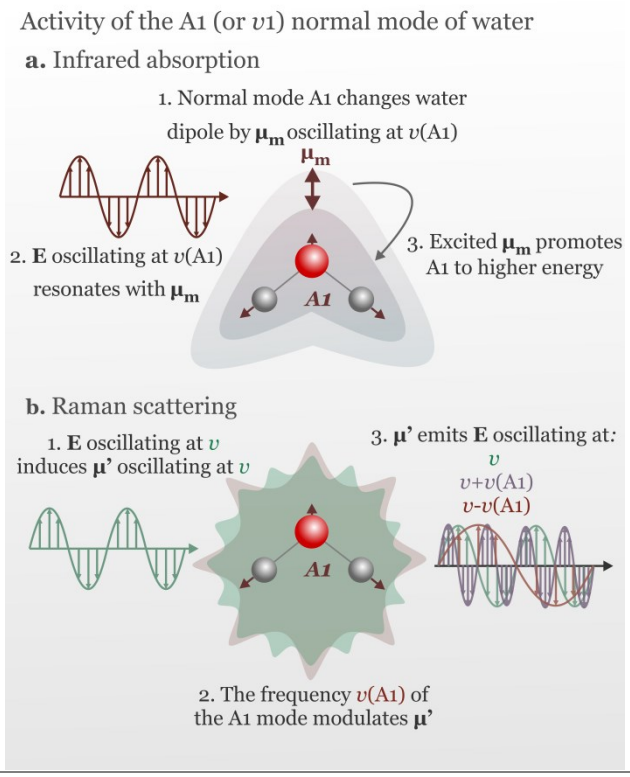

Figure 3.3. Main interactions of electromagnetic radiation with the A1 normal mode of water. **a.** Infrared absorption occurs if the incident radiation has the same frequency as the oscillation that the normal mode induces in the dipole moment. **b.** In the Raman scattering process the incident radiation induces a dipole moment that re-emits radiation. If the normal mode introduces a time-dependency in the polarizability of the molecule, its frequency modulates the oscillation of the induced dipole moment. As a result, the radiation re-emitted is modulated with the frequencies of the normal mode.

Electromagnetic radiation is able to interact with the periodic redistribution of charge accompanying atomic vibrations. As atoms oscillate following the pattern of a normal mode, their surrounding electric charge rearranges at the same frequency v_m of the normal mode, thus adapting to the geometry of the displaced configuration. Since v_m typically lies in the infrared range of the electromagnetic spectrum, the oscillating charge interacts with infrared radiation in two main ways: 1) If the oscillating charge modifies the electric dipole

of the molecule by $\boldsymbol{\mu_m}$, this dipole can absorb electromagnetic radiation of frequency v=v_m by exciting the associated normal mode (Figure 3.3a). In other words, displacements changing the dipole moment of the molecule are infrared-active. 2) The oscillating charge might interact with the dipole moment induced by an incident radiation. In this case, the oscillating dipole re-emits (i.e. scatters) radiation at a frequency modulated by the oscillation of the normal mode (Figure 3.3b). Displacements able to modulate the induced dipole moment are Raman-active.

3.3 The Raman Effect

The Raman effect is the frequency modulation of electromagnetic radiation after it is scattered from a material.

3.3.1 Classical description

Understanding the Raman scattering phenomenon requires evaluating how electromagnetic radiation induces electric dipoles in a molecule. The electric component of electromagnetic radiation $\boldsymbol{E}$ polarizes — i.e. deforms — a molecule and induces a dipole moment $\boldsymbol{\mu}'$ proportional to the magnitude of $\boldsymbol{E}$ (bold variables represent non-scalar properties):

$$\boldsymbol{\mu}' = \alpha \boldsymbol{E} \qquad \text{Equation 3.5}$$

where α is the polarizability of the molecule. From a molecular perspective, polarization occurs when an electric field displaces the electrons and nuclei of a molecule into opposite directions; α is a measure of the extent of such charge displacement.

Both α and $\boldsymbol{E}$ might change periodically in time. On one hand, $\boldsymbol{E}$ originates from an electromagnetic wave oscillating sinusoidally at an arbitrary frequency v. On the other hand, the atomic displacements of some normal modes might change α and introduce a time-dependence to the polarizability as well. In first approximation, α changes linearly with a small atomic displacement q, and the displacement itself might be assumed to vary sinusoidally with time t. As a consequence, the time-dependent polarizability acquires the form:

$$\alpha(q,t) = \alpha_0 + \left(\frac{d\alpha}{dq}\right)_0 q_0 cos(2\pi v_m t) \qquad \text{Equation 3.6}$$

where α_0 is the molecular polarizability at the equilibrium configuration, q_0 - the amplitude of the displacement, and v_m - the vibration frequency of the normal mode. The time variations of $\boldsymbol{E}(v)$ and $\alpha(v_m)$ can be inserted into Equation 3.5 to demonstrate how the

frequencies of the normal modes modulate the oscillation frequency of the induced dipole moment:[133]

$$\boldsymbol{\mu}'(t) = \alpha_0 \boldsymbol{E_0} cos(2\pi v t) + \left(\frac{d\alpha}{dq}\right)_0 q_0 \boldsymbol{E_0} [cos(2\pi(v + v_m)t) + cos(2\pi(v - v_m)t)] \quad \text{Equation 3.7}$$

Equation 3.7 implies that whenever a normal mode introduces a time-dependence to the molecular polarizability, the induced dipole moment $\boldsymbol{\mu}'$ oscillates at three distinct frequencies:

- At the same frequency v of the incident radiation (green in Equation 3.7). This component of the induced dipole precedes the so-called Rayleigh elastic scattering process.
- At a v_m frequency, shifted below that of the incident radiation v (red in Equation 3.7), preceding the so-called Stokes Raman inelastic scattering.
- At a v_m frequency shifted above that of the incident radiation v (violet in Equation 3.7), preceding the anti-Stokes Raman inelastic scattering.

The scattering process is completed when the induced dipole — which is itself a source of radiation — re-emits electromagnetic waves. Equation 3.7 emphasizes that Raman scattering processes occur when the displacement of a normal mode modifies the polarizability of the molecule, i.e. $(d\alpha/dq)_0 \neq 0$.

3.3.1.1 Orientation-dependent effects. The polarization of a molecule is anisotropic, i.e. it is orientation-dependent. In general, the electric field and the dipole moment induced do not point in the same direction. Hence the scalar polarizability introduced in Equation 3.5 needs to be algebraically defined as a rank-two tensor (Figure 3.4a), which establishes the mathematical relation between $\boldsymbol{E}$ and $\boldsymbol{\mu}'$.[134] Experimentally, the polarizability tensor behaves symmetrically, i.e. $\alpha_{ij} = \alpha_{ji}$; hence, only six of the nine components of the tensor are independent. These components are grouped into diagonal (*i=j*) and off-diagonal (*i≠j*) elements that can be used to quantify the anisotropy of the tensor.[133,135]

The re-emission of radiation from a dipole is also an anisotropic process. Considering the basic principles of classical electrodynamics[136], and the amplitude of the induced dipole $|\boldsymbol{\alpha E}_0|$ (Equation 3.5 updated with the tensor description in Figure 3.4a) oscillating at a frequency v, the time-averaged power $\bar{\rho}$ radiated at a distance r from the dipole can be expressed as:[133]

$$\bar{\rho} = \frac{\pi^2 v^4 |\boldsymbol{\alpha E_0}|^2 sin^2\theta}{2c^4 \varepsilon_0 r^2} \quad \text{Equation 3.8}$$

where ε_0 is the electric permittivity of vacuum. Equation 3.8 accounts for the two orientation phenomena described in Figure 3.4.

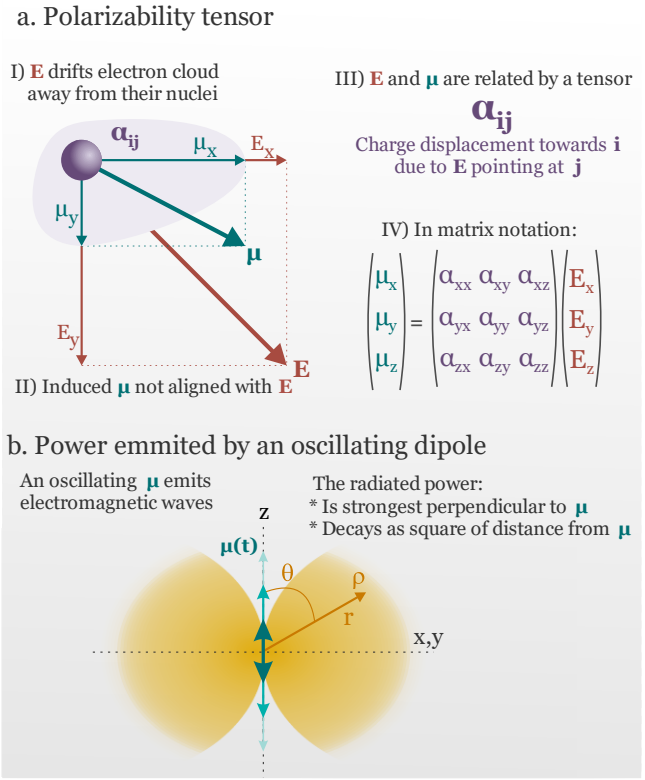

Figure 3.4. Orientation effects associated to the interaction and re-emission of electromagnetic radiation. **a.** The polarizability tensor. The electric charge surrounding the nuclei of the molecule is rigid against deformations in some directions, but more flexible to deform in other directions. Accordingly, the polarizability need to be algebraically defined as a rank-two tensor, which describes the extent of charge deformed in a direction due to an electric field pointing in another direction. **b.** The power emitted by an oscillating dipole. An oscillating electric dipole radiates more energy in some directions than in others, forming a characteristic lobe-shaped pattern, relative to the direction of the dipole moment.

In general, the orientation of the scattered electric field — as detected in an experiment — is influenced by both the anisotropy of the polarizability and the orientation-dependent re-emission of radiation. However, in special cases where the polarizability is isotropic (i.e. has negligible off-diagonal elements), the scattered electric field has the same direction as $\boldsymbol{E_0}$, independently of the orientation of the molecules in the sample. As a consequence, the scattered radiation is polarized, i.e. its electric field oriented in the same direction of the incident electric field $\boldsymbol{E_0}$.[137]

3.3.2 Quantum-mechanical description

The classical description of Raman scattering views the process as a modulation of the incident radiation by normal modes. In contrast, quantum-mechanics describes Raman scattering as a two-photon process (Figure 3.5): an initial photon promotes a normal mode from a starting vibrational state Ψ_s to a higher intermediate state Ψ_{in} and, subsequently, the

state Ψ_{in} relaxes to a final state Ψ_f, releasing a second photon. Assuming the harmonic approximation of Equation 3.3, the absorbed/emitted photons have an energy of $E = (n_f - n_s)h\upsilon$. Ψ_{in} is not necessarily an energy state intrinsic to the molecule/phase (i.e. an eigenstate): for non-resonant processes Ψ_{in} is rather introduced as a virtual state that enables discussing Raman scattering as a two-photon process.[133] The virtual state is, however, physically allowed to exist during a short interaction time due to the uncertainty principle.

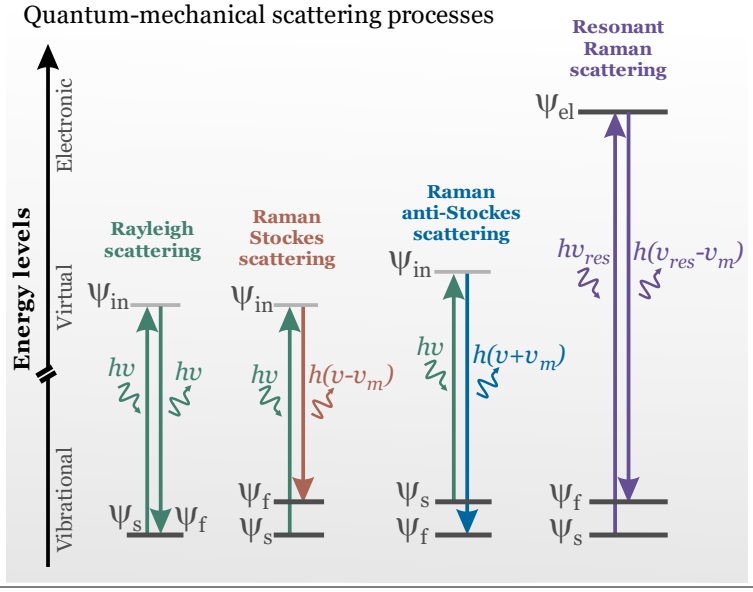

Figure 3.5. Quantum mechanical description of scattering processes. Scattering is described as two-photon process: an incident photon promotes a molecule from a starting vibrational state Ψ_s to an intermediate state Ψ_{in}, and a second photon is re-emitted due to the subsequent relaxation of the molecule to a final vibrational state Ψ_f. Rayleigh scattering occurs if the starting Ψ_s and final Ψ_f states have the same energy. Stokes Raman and anti-Stokes Raman processes occur when the final state Ψ_f has higher/lower energy than the starting state Ψ_f, respectively, and result in the re-emission of a photon of energy $h(\upsilon \pm \upsilon_m)$. Resonant Raman scattering occurs when the incident photon has enough energy $h\upsilon_{res}$ to promote a transition to an excited electronic state Ψ_{el}; as a consequence, the probability of re-emission of the second photon with energy $h(\upsilon_{res}-\upsilon_m)$ is greatly enhanced.

Note that normal modes in the ground vibrational state cannot undergo an anti-Stokes Raman process since they cannot be demoted to lower energy levels (Figure 3.5). Therefore, the number of anti-Stokes Raman events needs to be weighted by the proportion of modes existing already in excited states, defined by the Boltzmann distribution (Equation 3.4).

In addition, the quantum-mechanical expression defining the transition probability can be used to explore which normal modes are capable of Raman scattering. The algebraic properties of the vibrational wavefunctions and the polarizability yield two important conclusions about the plausibility of the Raman scattering transition. First, overtone transitions are forbidden if the wavefunctions are harmonic; however, anharmonicity

relaxes the selection rule such that overtone transitions (n_f - n_i > 1) also occur. Second, the Raman scattering transition is only allowed if the polarizability tensor and the normal mode share symmetry properties; more specifically, the transition is only allowed if the normal mode transforms according to any of the component of the polarizability tensor, under the operations of the point group of the molecule.[123] The components of the polarizability tensor transform according to the quadratic functions of the Cartesian coordinates (e.g. x^2, y^2, z^2, xy, xz, yz, and any of their linear combinations), which are commonly listed in character tables.[127,133] Hence, a normal mode is Raman-active if it belongs to the same symmetry species of one of the quadratic functions listed in the character table. Incidentally, normal modes transforming as the linear functions x,y,z are found to be infrared-active.[127]

The ideas above illustrate why symmetry is central to the description of vibrational spectra: the Raman/infrared activity of a normal mode can be quickly assessed by comparing its symmetry properties to the symmetry of the physical variables (dipole change, polarizability) mediating the interaction of the mode with electromagnetic radiation.

3.3.3 The Raman intensity

The induced dipole moments derived in Equation 3.7 can be inserted into Equation 3.8 to find the radiated power of an individual Raman scattering event. A system at temperature T with N_m Raman-active normal modes vibrating at a frequency v_m and with frequency degeneracy g_m, irradiated with an electromagnetic radiation of intensity I_0 and frequency v, will scatter Stokes Raman radiation over the whole space with an intensity that can be generally expressed as:[133,138]

$$I = AI_0 \frac{g_m N_m}{1 - e^{-hv_m/kT}} v(v - v_m)^3 \left(\frac{d\boldsymbol{\alpha}}{dq}\right)_0^2 \qquad \text{Equation 3.9}$$

where $\boldsymbol{\alpha}$ and q are the polarizability tensor and the displacement coordinate, associated to the normal mode, respectively, and A encloses multiple constants. The anti-Stokes Raman intensity features a similar mathematical expression.[133] Equation 3.9 is not universal: it is rather an expression that accurately captures the dependence of the intensity on the basic properties of Raman-active normal modes, namely their number, frequency, degeneracy, temperature-dependence and polarizability change. In general, only a 10^{-8} fraction of the incident photons undergo Raman scattering.[138]

As mentioned in section 3.3.1, isotropic polarizabilities preserve the direction of the incident electric field. The same occurs for the isotropic polarizability derivatives (Equation 3.9) that give raise to Raman scattering. Since only totally-symmetric vibrational modes (all

characters = 1 in character tables) result in isotropic polarizability derivatives, these modes scatter Raman radiation polarized in the same direction of the incident light.[137] Therefore, totally-symmetric modes can be identified by probing the sample with polarized light and measuring the polarization of the scattered light.[135]

3.3.4 Resonance Raman Effect

If the frequency *v* of the incident radiation approaches the energy required for promoting an electronic transition, the probability of a Raman scattering event increases significantly. As a result, the Raman intensity of certain normal modes may be enhanced up to 10^6 times from what is predicted by Equation 3.9. This phenomenon is called Resonant Raman scattering (Figure 3.5). In the non-resonant process, normal modes are promoted to higher vibrational states within the same electronic level. In resonant Raman scattering, however, the normal mode is promoted to a higher vibrational state within a higher electronic level (Figure 3.6). Resonance enhancement is governed by its own selection rules that depend not only on the properties of the vibrational states but also on the properties of the excited electronic state.[139]

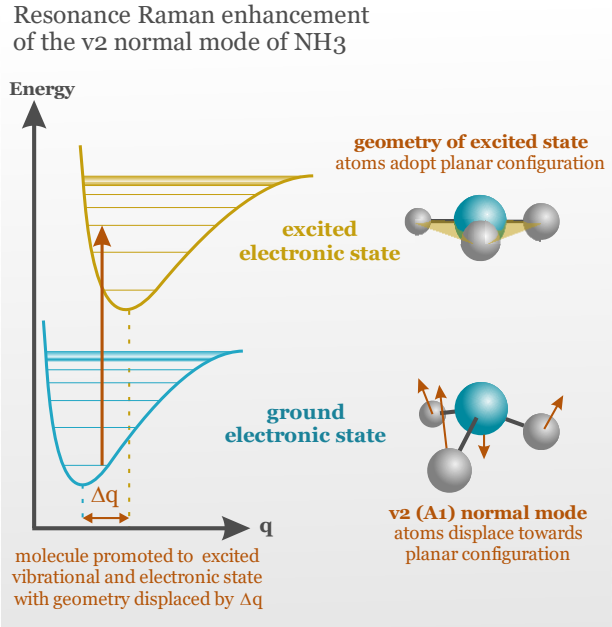

Figure 3.6. Resonant Raman scattering of the NH_3 molecule. In resonant conditions the molecule is excited to a higher vibrational state within a higher electronic level. The electronic excitation occurs with a deformation of the molecule Δq, hence the resonant process is governed by an A-term contribution. The electronically-excited NH_3 molecule adopts a planar configuration. Since the displacement pattern of the υ_2 mode mimics the geometry of the excited electronic state, its Raman scattering probability is greatly enhanced.[140]

The resonant selection rules are usually described by four different contributions (terms A, B, C and D).[139] In most cases the electronic transition changes the geometry of the molecule,

and the A-term contribution is dominant. The A-term affects normal modes featuring displacement patterns that imitate the geometry change accompanying the electronic transition.[141] In other words, if the Raman activity of a normal mode is resonance-enhanced by an A-term contribution, its displacement pattern reproduces the geometric deformation that the molecule undergoes as a consequence of the electronic transition (Figure 3.6).

The selection rules of the A-term contribution dictate that if the symmetry of the molecule does not change in the excited electronic state, then only totally-symmetric normal modes can undergo Raman resonance enhancement. In addition, the totally-symmetric normal modes often exhibit overtones of comparable intensity to the fundamental vibrations.[139,142]

3.4 The Raman spectrum

The Raman spectrum is the frequency-resolved distribution of radiation scattered from the sample. Raman-active vibrations are observed at frequencies $v + v_m$ (anti-Stokes) and $v - v_m$ (Stokes); in most cases, however, only the frequency region below v is analyzed since the Stokes scattering events are inherently more intense (section 3.3.3). In vibrational spectroscopy, the frequencies v_m are conventionally divided by the speed of light *c* in vacuum (in units of *cm/s*) and are expressed as wavenumbers $\tilde{v}_m$:

$$\frac{v_m[s^{-1}]}{c[cm/s]} \equiv \tilde{v}_m[cm^{-1}] \qquad \text{Equation 3.10}$$

A Raman spectrum is represented as a plot of scattered intensities versus the wavenumber shift from v_0 (Figure 3.7). A Raman spectrum is generally characterized by:

3.4.1 Number of discernible Raman bands

The number of Raman-active bands expected for a simple compound of N atoms is found by first counting the number of vibrational normal modes according to $N_m = 3N-6$ (section 3.2.1). Then, the displacement patterns of each atom are symmetrized according to the point/factor group, and classified into their respective symmetry species (section 3.2.3).[125,130] Last, the selection rules of these symmetry species are inspected in their respective character table to find which of those N_m modes are Raman-active. The previous procedure does not say anything about the frequency of the bands; hence, frequency-degenerate Raman-active modes (section 3.2.2) appear as one band in the spectrum and result in the observation of fewer bands than expected. Likewise, deformed geometric environments modifying the assumed point/factor group, in addition to overtones and other phenomena, might each generate more bands than expected.

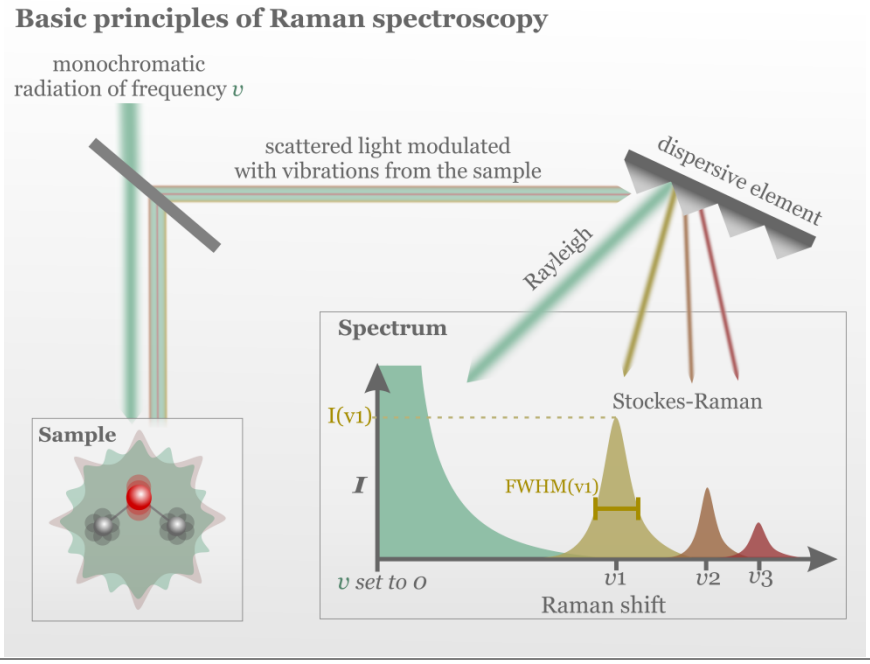

Figure 3.7. Basic principles of Raman spectroscopy. A monochromatic radiation of frequency υ is shined upon the sample. The radiation scattered back has been modulated by the vibration frequencies υ_1, υ_2 and υ_3 characteristic of the sample. A dispersive element split these frequencies, and a sensor detects their respective intensities. The information is presented as a spectrum: a plot of the intensity of radiation at frequencies shifted from υ (i.e. υ is set to 0). The vibrations of the sample manifest as bands, each with a characteristic frequency, intensity, width (usually the full width at half maximum or FWHM) and line-shape.

3.4.2 Wavenumbers

The wavenumber (and frequency according to Equation 3.10) of the Raman bands depend on the effective mass of the atoms involved in the vibration and the steepness of the potential energy-well holding these atoms to their equilibrium positions (Equation 3.2 and Figure 3.1a). However, it is difficult to calculate these values with the precision required for wavenumber prediction.[143] Moreover, anharmonic atomic displacements (Figure 3.1b), reduced vibration domains as in nano-crystalline solids, stress and strain, might all cause deviations from the ideal values predicted by Equation 3.2.[128]

3.4.3 Intensities

Based on the properties of normal modes, their Raman scattering intensity follows the functional dependence of Equation 3.9. The constant A in this equation can be worked out to explicitly account for the sampling effects related to the detection of the Raman signals. In condensed phases the Raman intensities also decrease when the size of the particles is reduced, as the scattered signal becomes more diffuse in the presence of an increased number of grain boundaries.[144] In practice, nevertheless, quantification based on Raman intensities is difficult and only applied in few cases.[145] Instead, the variations on relative

intensity are observed among different measurements, in order to detect and interpret the underlying phenomena.

3.4.4 Widths and line-shapes

Vibrational bands feature a natural broadening that is related to the lifetime of their excited vibrational state; i.e. the time that the normal mode survives in the Ψ_{in} state (Figure 3.5) before returning to Ψ_f due to spontaneous relaxation or anharmonic effects.[7,132] A band naturally broadened can be fitted with a Lorentz-type profile. However, sample-related properties such as disorder and strain/stress, in addition to instrumental effects, might all distribute the vibrational frequencies over a wide region and broaden the experimentally observed bands. As a consequence, the band profiles might feature a Gaussian-type shape that reflects the statistical distribution of frequencies around an average value.[146]

3.5 Summary

Vibrations are periodic displacements of atoms around their equilibrium coordinates. Vibrations are described as combinations of independent normal modes, each consisting of a collection of atoms oscillating at the same frequency and in-phase. The Raman effect is an inelastic scattering process where the normal modes of a sample modulate the frequency of the electromagnetic radiation scattered from the sample when irradiated with monochromatic light. Normal modes that change the polarizability of the molecule are Raman-active. Raman spectroscopy is the study of Raman-active atomic vibrations. A Raman spectrum is characterized by the number of observed bands, their wavenumbers, intensities, widths and lineshapes. Raman spectroscopy is sensitive to the short-range ordering of condensed phases since the atomic vibrations of some discrete molecular units are readily detected independently of the degree of structural organization. The intensity of some bands can be greatly enhanced if the frequency of the light source approaches the energy of an electronic transition.

Chapter 4 Materials and Methods

Confocal Raman spectroscopy has been used a main tool in this work for recording the *operando* Raman spectra of $LiMO_2$ cathode materials. Chapter 4 starts by summarizing the basics of confocal Raman spectroscopy, followed by a discussion of the design principles implemented in the development of the Raman spectro-electrochemical cell. Then, the details of the cell materials and cycling protocols are followed by the electrochemical and spectral validation methods of the developed cell. Last, the chapter portrays the data analysis methodology implemented for retrieving robust and meaningful data trends from hundreds of recorded *operando* spectra. Minor parts of this chapter have been published by **E. Flores**, P. Novák, E.J. Berg, *Front. Energy Res.* (2018), 6:82.[67]

4.1 Confocal Raman spectroscopy

Confocal Raman spectroscopy couples a Raman spectrometer with a confocal optical microscope for acquiring spatially-resolved Raman spectra. The optical ensemble of the microscope narrows the laser probing volume down to several micrometres, providing thus high spatial resolution.

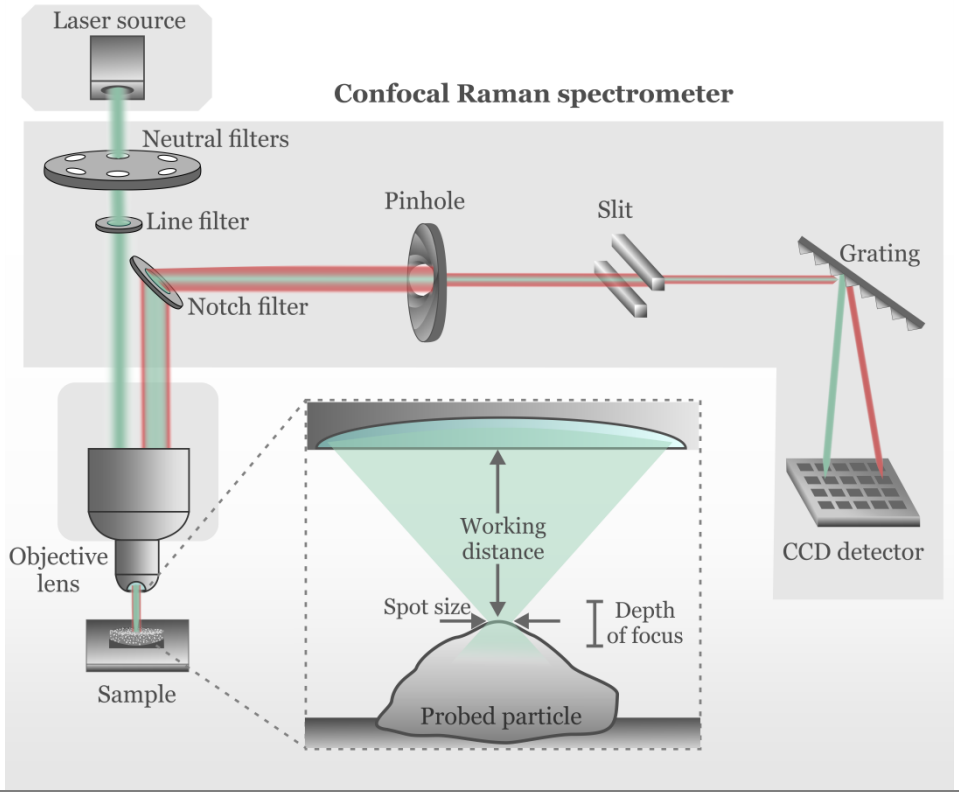

Figure 4.1. Schematic representation of a confocal Raman spectrometer.

Figure 4.1 illustrates the basic principles of a confocal Raman spectrometer. First, a laser emits a highly monochromatic beam of wavelength λ with a narrow wavelength spread of $\pm\delta\lambda$, subsequently, a neutral filter attenuates the beam power at all wavelengths. In typical setups, multiple filters with increasing attenuation strength are assembled in a wheel that the user can control. A line filter rejects wavelengths in the vicinity of λ (i.e. minimizes $\delta\lambda$); thus, making the beam more monochromatic. The spatial width of the beam is reduced as it passes through the optical setup of the microscope. The objective lens then focuses the beam into a small spot on the sample.[147]

The spot size diameter d establishes a limit of lateral resolution, and is related to the wavelength of the incident beam λ and the optical characteristics of the objective lens expressed as a Numerical Aperture NA. The relation among these quantities can be approximated as:[148,149]

$$d = \frac{1.22\lambda}{NA} \qquad \text{Equation 4.1}$$

Likewise, the depth of focus (D_f) determines the axial resolution and it is defined as the distance from the focal plane where the beam attenuates to half of its initial power. D_f can be approximated as:[148,149]

$$D_f = \frac{2\lambda}{NA^2} \qquad \text{Equation 4.2}$$

Given the laser source wavelength (λ=633 nm) and the objective lens (NA=0.55) used in this work, the laser beam should focus in a spot size of 1.4 µm diameter and feature a 4.2 µm depth of focus. However, the penetration of the beam might be shallower than what Equation 4.2 predicts, since D_f also depends on the dielectric properties of the sample.[150]

After interaction with the sample, the beam is back-scattered and collected via the microscope optics. Now the beam is a polychromatic combination of a strong Rayleigh component of wavelength λ, weakly modulated with the Raman signals of the sample. Hence, a notch filter is used to selectively attenuate the Rayleigh contribution, while transmitting both the Stokes and anti-Stokes Raman signals.[144] The filtered signals travel through a pinhole with a controllable diameter, which improves the spatial resolution of the beam by rejecting the light scattered from regions outside the sampling volume. Reducing the pinhole size improves spatial resolution but reduces the light collection efficiency, thus weakening signal's intensity. Then, a slit narrows the beam into a line that is later dispersed by a grating into separate wavelengths. The grating consists of a surface with parallel

grooves that reflect light at wavelength-dependent angles. A higher groove density results in wider wavelength dispersion and better spectral resolution, but at the expense of reduced signal intensity. Finally, the wavelength-separated photons are collected by CCD detector.[147,149]

Most of the results in this work were obtained using a Horiba Jobin-Ivon HR800 confocal Raman spectrometer, unless otherwise specified. The parameters of this confocal Raman setup are summarized in Table 4.1.

Table 4.1. Parameters used in the confocal Raman spectrometer setup.

Excitation Laser	Power controlled by the neutral D-filters. Measured with an Integra power-meter, Gentec, Canada.	D0: 8.2±0.2 mW D0.3: 4.4±0.2 mW D0.6: 2.3±0.2 mW D1: 1.0±0.2 mW
	Wavelength	633 nm
Objective lens	Magnification	50X
	Numerical aperture	0.55
	Manufacturer	Olympus Japan
Other parameters	Pinhole diameter	1.000 mm
	Slit separation	100 μm
	Grating groove density	600 lines/mm

4.2 Development of the Raman spectro-electrochemical cell

The key challenge in the design of an *operando* cell for Raman spectroscopy is to incorporate an optically transparent window, while keeping optimal electrochemical performance of the cell. This task is full of compromises that have been historically approached by implementing diverse cell designs.[151] As part of this PhD work, a custom-made cell with coin-cell type configuration was developed (Figure 4.2), building on the past knowledge available in our research group and avoiding the compromises, where possible. The cell design and parameters comply with multiple experimental constrains that can be divided into:

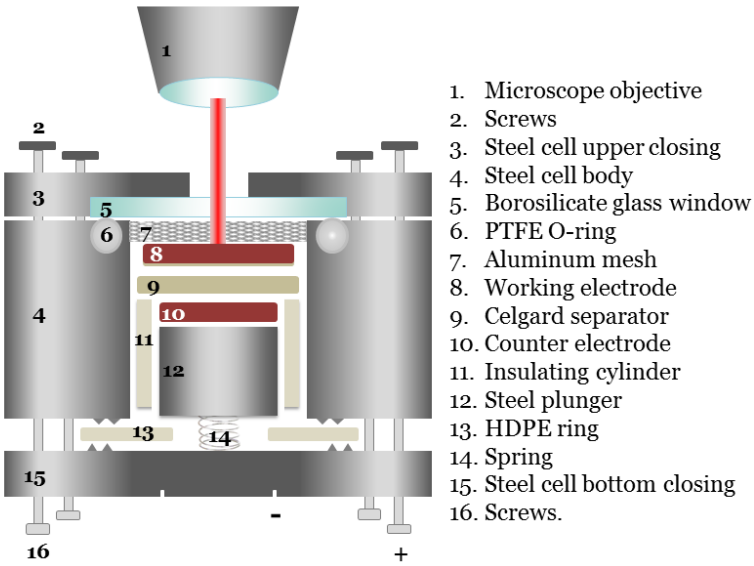

Figure 4.2. Schematic representation of the developed Raman spectro-electrochemical cell, along with the main cell parts.

4.2.1 Design constrains for optimal electrochemical performance

4.2.1.1 Facile assembly and reuse. Considering that the cells are built inside a glovebox, where dexterity of the operator is reduced, the cell design must permit convenient and exact assembly for guaranteeing reproducibility. The developed Raman cell inherited the coin-cell design widely used in our lab, in order to employ the infrastructure and know-how already available. The amount of moving parts and disposable elements has been minimized for facilitating the simplicity of the assembly procedure and cell reuse.

4.2.1.2 Similarity to commercial cells. The cell geometry, materials and components of the developed cell have been chosen to approach the specifications found in commercially available CR16 and CR12 coin-cell type LIB cells, where electrical contacts, diffusion distances and electrode alignment have been carefully optimized. The selected coin-type cell geometry permits easy and reproducible alignment of the electrodes into a cell stack (parts 8, 9 and 10 in Figure 4.2). For instance, the cathode size was chosen to be 14 mm diameter (part 8, Figure 4.2), which is large enough for easy handling and alignment. In principle, the confocal Raman setup is able to analyse significantly smaller electrodes but reducing the mass of electrochemical active material requires the application of lower currents, which approach the sensitivity limits of typical galvanostats and thus lead to unreliable electrochemical measurements. In addition, the Raman cell plunger (part 12, Figure 4.2) has been machined to the exact dimension of the anode, i.e. 12 mm diameter

(part 10, Figure 4.2), for further minimizing the risk of misalignment. The anode has a smaller diameter than the cathode for avoiding detrimental edge effects during electrochemical cycling.[152]

Moreover, a strong mechanical compression of the electrode assembly is necessary to ensure its mechanical integrity and to reduce cell overpotentials. Inappropriate electrical contact would lead to inhomogeneous electrode reactions and eventually misinterpretation of underlying cell electrochemistry.[153] A uniform and stable electrode compression is typically achieved by employing a spring and a hard window to resist fracture (part 14, Figure 4.2). In the cell developed here, the spring provides a stable pressure over the electrode stack of ca. 20 N/cm^2.[154]

4.2.1.3 Stable performance during experiment. The *operando* electrochemical cell must be sealed gas-tight during the extent of the experiment. Gas leaks into the cell and electrolyte leaks out of the cell would compromise electrochemical performance and increase the risk of measuring artefacts associated with side reactions. Tight sealing is generally achieved by compression of rubber and/or plastic O-rings at both open ends of the cell chamber. Furthermore, all materials in contact with the electrodes and electrolyte (cell body, sealing parts, and transparent window) should be chemically and electrochemically inert under experimental conditions. Both polytetrafluoroethylene (PTFE) and high density polyethylene (HDPE) O-rings are chemically resistant toward typical Li-ion battery carbonate based electrolytes and effective in sealing the cell body against leakage (parts 6 and 13, Figure 4.2).

4.2.2 Design constrains for high spectral quality

4.2.2.1 Optimal light collection efficiency. The distance between the light source and the probed oxide sample (working distance in Figure 4.1) should be minimized in order to increase the solid angle for collection of scattered light, thereby improving the signal-to-noise ratio.[144] First, the electrode must be placed as close as possible to the window, while still being electrically connected to the cell body from where it is electrochemically polarized. The electrode is pressed against the window with solely a 125-µm-thin Al mesh in between (parts 7, 8, Figure 4.2); the mesh size is sufficiently large to permit access of the probing laser to the electrode. Second, the window must be thin, made of an optically transparent and Raman-inactive material, and resist fracture, which can be induced by the cell stack compression against it. The developed cell uses a 100 µm-thin borosilicate glass (part 5, Figure 4.2) that is stabilized against fracture as it rests in the flat metallic lid of the cell, holed with a minor 4 mm aperture (part 3, Figure 4.2). The implementation of a thin window and mesh enable exploring the electrode using an objective lens with high numerical aperture (NA=0.55), featuring thus a reduced working distance and good light collection efficiency.

4.2.2.2 Minimum interfering signals. The proximity between the window and the electrode shrinks the electrolyte-filled space travelled by the light probe (space between parts 5 and 8, Figure 4.2), thus reducing the interference of strong Raman signals from the electrolyte. In addition, an appropriate choice of excitation wavelength can minimize fluorescence effects. The degree of fluorescent emission depends on how close the laser wavelength is to the absorption maxima of the fluorescent species, which generally is found toward the blue side of the visible spectra.[112,155] In this work a 633 nm excitation source (red) is used for all experiments, unless otherwise specified.

4.2.2.3 Prevention of thermal decomposition of the sample. The laser specific power should be sufficiently high to achieve reliable signal-to-noise ratio, but low enough to avoid laser-induced sample transformations. In an air-exposed lithiated oxide, these transformations are observable above 1.0 mW/μm^2, but the limit can be lower for delithiated electrodes[156] and even lower for *in situ*/*operando* conditions, because of the presence of the organic electrolyte. In this work the *in situ* stability of the material was tested with various attenuation filters (D1 and D2, see Table 4.2) for each type of experiment, to make sure that the sample is minimally affected.

Table 4.2. Cell parts and parameters implemented in the Raman cell.

Gas sealants	Polytetrafluoroethylene (PTFE) O-ring (20 x 2 mm)	
	High-density polyethylene (HDPE) hollow disc	
Window	Material	Borosilicate glass
	Dimensions	φ20 mm x 100 μm
Cell body	Material	Stainless steel
	Optical aperture of the cell's lid	4.0 mm
Power over the sampling spot (based on spot-size from Equation 4.1)	50X magnification, D1 filter	~0.6 mW/μm²
	50X magnification, D2 filter	< 80 μW/μm²

4.3 Electrode preparation and cycling

4.3.1 Preparation of composite electrodes

The composite electrodes were prepared from mixed slurries of 89 wt % active material, 5 wt % polyvinylidene difluoride (PVdF Kynar HSV 9000), 4.6 wt % amorphous carbon Super C65, and 1.4 wt % graphite dispersed in n-methyl pyrrolidone solvent (NMP). Prior to experiments, all active material powders were stored in an Ar-filled glovebox to avoid air

exposure. The slurries were coated onto Celgard 2400 sheets by the doctor blading technique[157,158] at a 100-µm wet thickness. The coated sheets were dried for 10 h under dynamic vacuum at 80 °C, punched to 14-mm diameter electrodes, further dried under dynamic vacuum at 80 °C overnight, and finally introduced into an argon filled glovebox without air exposure. Electrodes typically featured loadings of active material between 10-16 mg/cm^2, without counting the mass of the Celgard substrate.

Table 4.3. Materials used for preparation of the composite electrodes, the electrolyte and the cell assembly.

	Chemical	Supplier
Active material powders	$LiCoO_2$	Alfa Aesar, Germany
	$LiNiO_2$	Sigma-Aldrich, Germany
	$LiNi_{0.8}Co_{0.15}Al_{0.05}O_2$	Leclanché SA, Switzerland
	$LiNi_{0.33}Co_{0.33}Mn_{0.33}O_2$	BASF SE, Germany
	$LiNi_{0.6}Co_{0.2}Mn_{0.2}O_2$	BASF SE, Germany
	$LiNi_{0.8}Co_{0.1}Mn_{0.1}O_2$	BASF SE, Germany
Electrolyte	LC30: 1.0 M $LiClO_4$ in 1:1 (w/w) ethylene carbonate (EC)/dimethyl carbonate (DMC)	BASF SE, Germany
Others	Li-metal	Sigma-Aldrich, Germany
	Binder: polyvinylidene difluoride (PVdF) Kynar HSV 900	Arkema, France
	Conductive additive: amorphous carbon Super C65	Imerys Graphite and Carbons, Switzerland
	Conductive additive: graphite SFG6	Imerys Graphite and Carbons, Switzerland
	Polypropylene separator: Celgard 2400	Celgard LLC, USA
	Glass fiber separator	EUJ116, Hollingworth & Vose Company Ltd., UK
	Cathode current collector: aluminium mesh 5 Al 7-125	Dexmet corporation, CT, USA
	n-methyl pyrrolidone solvent (NMP)	Sigma-Aldrich, Germany

4.3.2 Raman cell assembly and cycling

The custom-made Raman spectro-electrochemical cell was assembled inside an argon-filled glovebox (O_2, H_2O < 1 ppm). Before assembly, the composite electrode and a glass fibre separator (Ø17 mm, 1 mm thick) were wetted for several minutes in LC30 electrolyte (1.0 M $LiClO_4$ in 1:1 (w/w) ethylene carbonate (EC)/dimethyl carbonate (DMC)) to ensure sufficient wetting.

The assembling of the Raman cell is started by placing the glass window onto the inner face of the cell's lid, fitting a PTFE O-ring into the circular indentation on the top face of the cell's body, and screwing together the ensemble (parts 2-6, Figure 4.2). Next, the aluminium mesh (Ø17 mm) was placed on the glass window; the wet cathode composite electrode was subsequently pressed against the mesh for electric contact, followed by the introduction of two Celgard separators previously wetted in electrolyte. Then, an insulating cylinder and the plunger holding the lithium metal counter electrode disk (0.2 mm thick, Ø12 mm) were consecutively added (parts 10-12, Figure 4.2). Last, the spring and the HDPE cylinder were placed into and around the plunger, respectively; the bottom lid was placed on the cell's body bottom face, and finally cell was closed and sealed by tightening the screws (parts 13-16, Figure 4.2).

The cell was cycled galvanostatically (i.e. at constant current) at room temperature with a computer-controlled galvanostat (CCCC Hardware, Astrol Electronic, Switzerland), typically at an applied current of 10 mA/g normalized to the weight of the active material in the electrode, unless otherwise specified. The state of lithiation (SOL) was calculated based on the ampere hour counting method.[159] The SOL x is defined as the fraction of lithium left in the structure at a given time t [h], based on the galvanostatic current I [mA], the weight of the active material m_{active} [g] and the theoretical limit of specific charge Q_{th} [mAh/g] according to:

$$x = \frac{It}{Q_{th}\, m_{active}} \qquad \text{Equation 4.3}$$

The SOL of every delithiation step starts from the SOL where the previous lithiation ended; likewise, the SOL of every lithiation step starts from the SOL where the previous delithiation ended. The calculated theoretical limits of specific charge for each oxide are presented in Table 4.4.

Table 4.4. Theoretical limit of specific charge of multiple layered oxides.

Layered oxide	Q_{theor} [mAh/g]
$LiCoO_2$	273.9
$LiNiO_2$	274.6
$LiNi_{0.8}Co_{0.15}Al_{0.05}O_2$	279
$LiNi_{0.33}Co_{0.33}Mn_{0.33}O_2$	279.5
$LiNi_{0.6}Co_{0.2}Mn_{0.2}O_2$	276.5
$LiNi_{0.8}Co_{0.1}Mn_{0.1}O_2$	275.6

4.4 Validation of the Raman spectro-electrochemical cell

Figure 4.3 shows the electrochemical performance and spectral quality enabled by the newly developed Raman cell, using a $LiNi_{0.8}Co_{0.15}Al_{0.05}O_2$ (NCA) composite electrode. NCA is a convenient benchmark for comparing the spectral quality of the cell due to its inherently weak Raman signals. When NCA is cycled between 3.0 and 4.3 V (Figure 4.3a), the electrode potential profile *E(x)* features very low overpotentials between cycles (η < 10 mV). In addition, NCA delivers reversibly a specific charge of 221 mAh/g, fairly close to the practical specific charge achieved by commercial-like cells.[30,31]

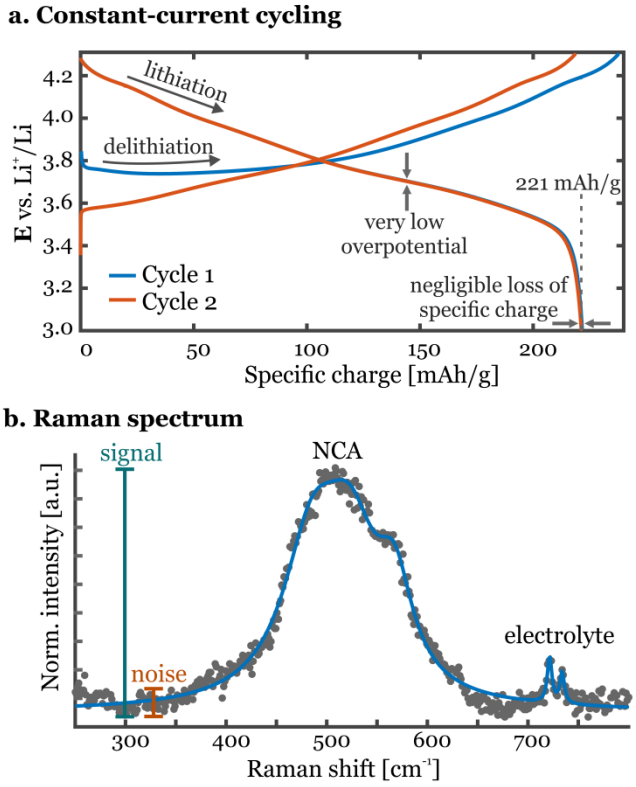

Figure 4.3. Validation of the newly-developed Raman spectro-electrochemical cell. **a.** Galvanostatic potential profiles of a $LiNi_{0.8}Co_{0.15}Al_{0.05}O_2$ (NCA) composite electrode cycled *vs.* Li-metal (1 M $LiClO_4$ in EC:DMC 1:1 wt., 10 mA/g rate) using the developed Raman cell. The cell enables cycling NCA up to 221 mAh/g. The profiles have low overpotentials and negligible loss of specific charge between the first and second cycle. **b.** *In situ* spectra of an NCA particle of the composite electrode assembled inside the cell (0.2 mW/µm², 100 s exposure).The spectrum features a high signal-to-noise ratio and minimal electrolyte signals, which in all enables easy identification and fitting of the inherently weak NCA bands.

The developed cell provides not only cycling performance well comparable to a standard coin-cell, but also improved quality of the *in situ* spectra compared to the literature.[160] Figure 4.3b shows that the Raman spectrum of NCA recorded with the new cell features well-resolved spectral features, weak or even negligible electrolyte bands and low noise. The spectrum was recorded over 10 minutes of exposure that enables the acquisition of ca.

250 spectra during a full cycle at a literature-standard rate of 10 mA/g; comparable time-resolved experiments in the literature record fewer than 60 spectra per cycle.[161,162]

4.5 Data analysis

In this work, instead of picking out sample data-sets — as is typically reported in the literature — the hundreds of Raman spectra resulting from every *operando* experiment are all processed for obtaining robust and meaningful patterns within narrow cycling intervals. To this end, several Matlab scripts (version R2016a) were developed as part of this PhD work to perform automated data processing of all spectra outputted from an *operando* experiment. Figure 4.4 illustrates the three main techniques employed for analysis: peak fitting, multivariate curve resolution and bidimensional correlation analysis; the last two techniques were applied as alternatives to peak fitting in cases where the experimental Raman bands were heavily overlapping.

4.5.1 Baseline correction and peak fitting

Baseline correction is the process of separating the slow-varying fraction of the spectrum — the baseline — from the sharp features representing the Raman response of the sample. Initially, the sections of the spectrum belonging to the baseline need to be identified, either by a mathematical method or by visual inspection. These sections are fitted either parametrically (i.e. by optimizing the parameters of an analytical function such as a polynomial), or non-parametrically (e.g. local curve fitting, smoothing, and others).

Peak fitting aims at separating the individual contributions of vibrational bands from an overlapping spectral envelope. The process involves the use of analytical mathematical expressions describing the vibrational bands with few parameters matching the experimental data points. All possible information about the sample (section 3.4.4) must be considered when choosing a fitting model able to deliver physically meaningful results.[146] The strategy adopted in this PhD work for the automated baseline correction and peak fitting of numerous spectra is summarized in the following steps:

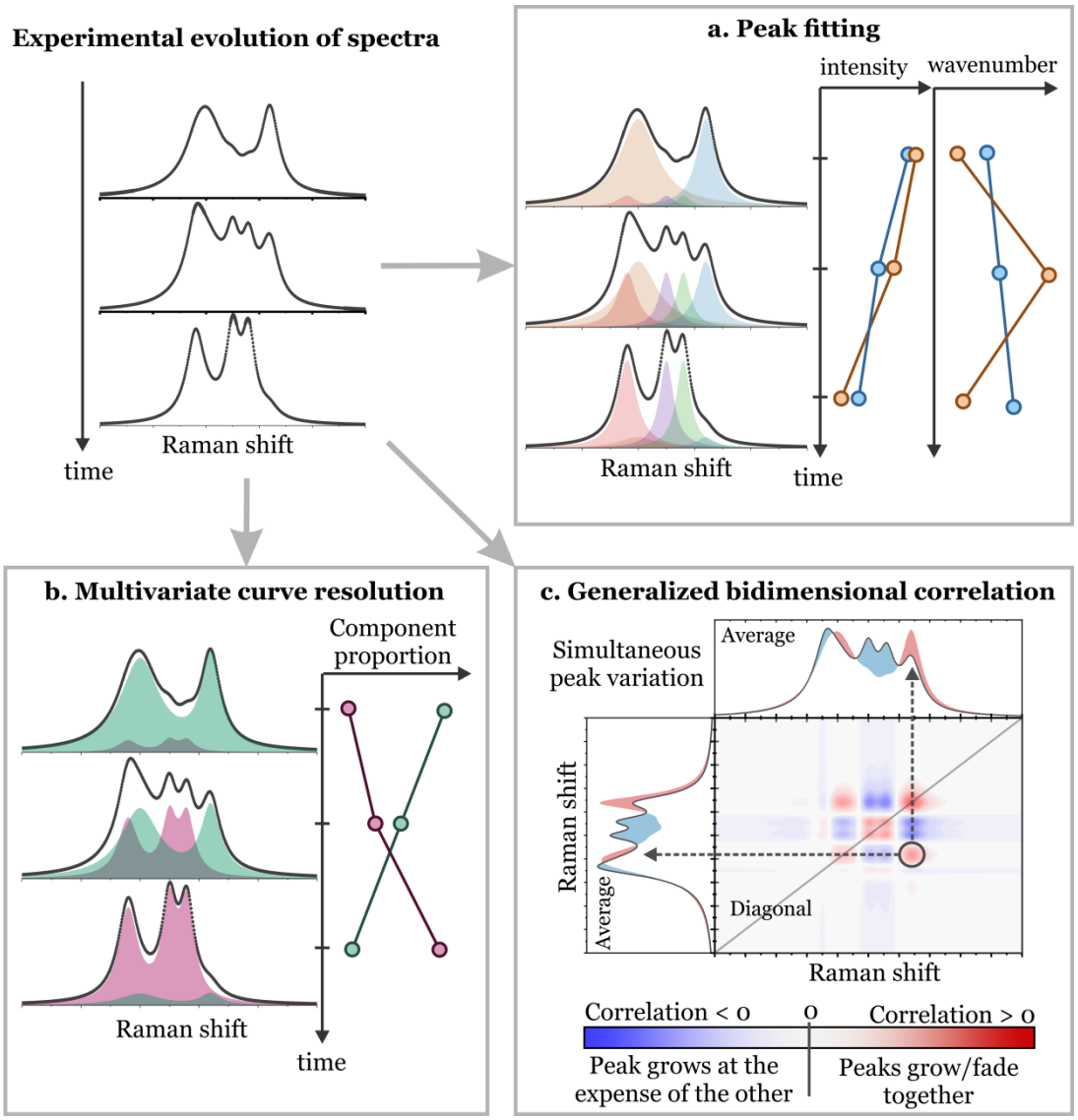

Figure 4.4. Simulated results from the three techniques applied for analysing the time-dependent evolution of the spectra. **a.** Peak fitting. Each spectrum is fitted and the variations of the fitting parameters (e.g. peak intensity, wavenumber) are followed during cycling. **b.** Multivariate curve resolution (MCR). The variations of spectral intensity during the experiment are quantified for computing pure components that explain most of the intensity variance. If the resulting components compare to experimental spectra, they carry physical meaning and their proportions can be followed during cycling. **c.** Synchronous plot from the generalized bidimensional correlation analysis. As in MCR, the intensity variance is computed, but this time for finding pairs of wavenumbers responding simultaneously to (de)lithiation. The circled region features positive correlation according to the colour code, meaning that the peaks shown by arrows grow/fade simultaneously during (de)lithiation. These peaks likely share a common physical origin.

4.5.1.1 Visual inspection of optimum baseline and fitting parameters. A Matlab-based graphical user interface **spectrum_inspection_GUI.mlapp** was developed for systematically executing the following steps:

a) Load and visualize a randomly selected spectrum.

b) Cut the spectrum into the wavenumber range displaying the signals from the oxide, which are typically found between 350 and 700 cm^{-1}. A slightly wider region (e.g. 300-800 cm^{-1}) is selected for including more data points belonging to the baseline and thus improving the fitting.

c) Determine by visual inspection the intervals of the spectrum featuring the Raman signals of the oxide, i.e. not belonging to the baseline. The script performs the baseline polynomial fitting only on the data-points of the baseline.

d) Test polynomials with different degrees for finding the curve that best fits the baseline. This step is critical since an under/over-fitting of the baseline curve would result in an over/under-estimation of the Rama band intensities of the oxide. Since the baseline signals originate from physical phenomena (e.g. fluorescence), varying slightly within the 300-800 cm^{-1} region, these signals are better described by low polynomial degrees (e.g. second, third). If no polynomial degree provides a satisfactory fitting, step c) is repeated with a new choice of baseline intervals. If the fitting still does not improve, step b) is repeated with a wider or narrower spectral range (± 50 cm^{-1}).

e) Subtract the optimal baseline curve from the spectrum.

f) Define a peak fitting model based on visual inspection of the baseline-subtracted spectrum and any available physical information about the sample (e.g. the expected number of bands, presence of overlapped contributions, among others). A fitting model consist of:

   - The number of peaks to be used for the fitting.
   - The functional profile of these peaks (Lorentzian, Gaussian, Voight, etc.), which also determines the number of parameters to be fitted.
   - The constraints of each parameter, i.e. the lowest and highest values each parameter is allowed to acquire during the iterative fitting process.
   - The initialization parameters, i.e. the initial values of each parameter when the iterative fitting process is started. The GUI is already scripted with default initialization values that are based on the constraints specified by the user.

g) Fit the baseline-subtracted spectrum. The Matlab fit function uses a Trust-Region algorithm limited to a maximum of 400 iterations. The fitting model specified in step f) is modified until reaching a satisfactory peak fit.

h) Repeat steps a) to g) for many randomly-selected spectra (at least 10), testing if the baseline and fitting outcomes are satisfactory for all selected spectra. In most cases, the parameters need only minor modification from spectrum to spectrum.

i) Once a set of baseline and peak fitting parameters have been found to be robust for 10+ samples, they are exported for performing the automated fitting.

4.5.1.2 Automated baseline and peak fitting of all spectra. The optimum parameters obtained from the visual inspection are input sequentially in a series of Matlab scripts as follows:

- **counts.m** loads all spectra from their directory, cut all to the desired spectral region and exports separate files containing i) the names, ii) dates/times of acquisition, iii) intensities, and iv) wavenumbers of all spectra.
- **cycling.m** loads, organizes and exports the cycling data, while the script **synch.m** synchronizes the electrochemical readings with the dates/times of acquisition of each spectrum.
- **baseline.m** loads the intensity files from step a), performs a polynomic baseline fitting to all spectra, and exports the baseline-subtracted intensities.
- **fit_lorentzian.m** loads the baseline-subtracted spectra, fits and exports the optimum fitting parameters found for each spectrum. The fitting is also carried out using the Trust-Region algorithm with a 400 iterations limit.

The accuracy of the automated process is verified by inspecting the fitted baselines and peaks of several spectra in order to judge whether the curves satisfactory fit the experimental data. Finally, the fitting parameters of the peaks are plotted versus the electrochemical readings from the synchronized cycling data (Figure 4.4a).

4.5.2 Multivariate curve resolution (MCR)

MCR is a multivariate analysis technique that decomposes a spectrum into a linear combination of independent components, each weighted according to their relative contribution. The components are unmixed iteratively from the complete dataset of cycling-dependent spectra, aiming at maximizing the percentage of the explained intensity variance during the experiment. As a result, the experimental variation of spectral intensities can be represented as the independent evolution of the proportion of each component (Figure 4.4b).[163]

The MCR analysis was performed with the graphical user interface provided in reference [163]. The GUI loads the baseline-subtracted spectra, finds the profiles of the components and their respective proportions. Since the analysis uses minimum input from the physical nature of the system, it is necessary to verify that the results carry relevant information by examining if the components compare well to real spectra. Experimentally comparable components can be confidently interpreted and used to obtain cycling-dependent spectral trends (Figure 4.4b).

The pre-treatment step involved baseline-correcting all spectra using a polynomial of third degree as specified in section 4.5.1. The data set was smoothed using a moving average algorithm with a window of 10 data points. The time variance of all spectra was modelled using two components, set to run with a noise tolerance of 10%, a convergence threshold of 0.1 and a maximum of 40 iterations. The components explained 99.6% of the time variance.

4.5.3 Generalized bidimensional correlation analysis

The generalized bidimensional correlation analysis explores the simultaneous and sequential variations of spectral intensities of two different spectral regions when the system is perturbed by an external stimulus (e.g. change of temperature, pressure, state of lithiation). The technique first calculates the intensity variations at each wavenumber during a perturbation; in the *operando* experiment the state of lithiation of the electrode is perturbed during cycling. Then, these variations are used for computing the intensity covariance at every pair of wavenumbers. Large covariance highlights spectral regions responding simultaneously (synchronous correlation) and sequentially (asynchronous correlation) to electrochemical cycling. Synchronous and asynchronous response types are usually represented in separate plots, each consisting of a wavenumber *vs*. wavenumber plane of orthogonal axes where the covariance is represented as a contour map (Figure 4.4c). The covariance values are mapped using a colour code that relates the behaviour of every pair of bands in the abscissa and ordinate coordinates.[164] In this representation, the main diagonal exhibit self-correlation zones (correlations between the same peak), while off-diagonal zones contain cross-correlation zones (correlation between different peaks). The covariance map is symmetric with respect to the main diagonal, so the analysis is made only using either the upper or lower diagonal regions. In addition the static spectra — the average of all spectra — are plotted in the top and left axis for visualizing the peaks showing correlations (Figure 4.4c). The mathematical formalism of the analysis as described in reference [165] was implemented in a Matlab script **corr2D.m.** The script loads the baseline-subtracted spectra and exports the datasets with the resulting synchronous and asynchronous maps.

Chapter 5 Raman spectra of lithiated oxides

Even if most commercially-relevant lithiated oxides share a common crystallographic structure, their Raman spectra exhibit significant differences depending on the specific transition metal composition. In this chapter the relationships between spectral features and crystallographic as well as electronic structure of the oxides are discussed, by comparing the experimental results with the predictions based on i) the symmetry of an ideal crystallographic $R\bar{3}m$ structure and ii) first-principles lattice models where the effects of bonding and electronic structure are explicitly accounted. Last, the Raman spectra of $LiMO_2$ measured using multiple excitation wavelengths are analysed, searching for Raman enhancement effects linked to electronic structure of the oxides. Some excerpts of this chapter have been published in **E. Flores**, P. Novák, E.J. Berg, *Front. Energy Res.* (2018), 6:82,[67] and reproduced in part with permission of Chemistry of Materials, submitted for publication (2019).

5.1 Predictions based on crystallographic lattice symmetry

5.1.1 Nuclear site group analysis

The symmetry-based classification of normal modes of vibration permits a quick identification of the number of Raman-active modes and their displacement patterns (section 3.2.3). From the multiple ways of determining the symmetry-based classification of normal modes in crystals, the nuclear site group analysis is preferred due to its facile and intuitive approach. The method symmetrizes the three degrees of translational freedom of each atom, according to the factor group of the lattice and the point group of the atom site.[130] The procedure requires as inputs only the diffraction-refined i) space group and ii) Wyckoff sites of each atom in the lattice. The nuclear site-group-analysis procedure applied on layered $LiMO_2$ is illustrated and formulated in Figure 5.1.

The analysis provides three key conclusions about the Raman activity of $LiMO_2$. First, the lattice features only two Raman-active modes, the A_{1g} mode and the E_g mode (Figure 5.1d). Second, only oxygen atoms possess A_{1g} and E_g degrees of freedom (Figure 5.1b), so both Raman-active vibrations reflect only oxygen displacements. Third, the A_{1g} mode reflects the displacement of oxygen atoms along the *c*-axis of the lattice, while the E_g mode reflects oxygen displacements along consecutive oxygen layers (Figure 5.1e). Given the properties of these modes, their corresponding bands primarily inform about the environment surrounding oxygen atoms. In the following section all these symmetry-based predictions will be compared to experimental spectra.

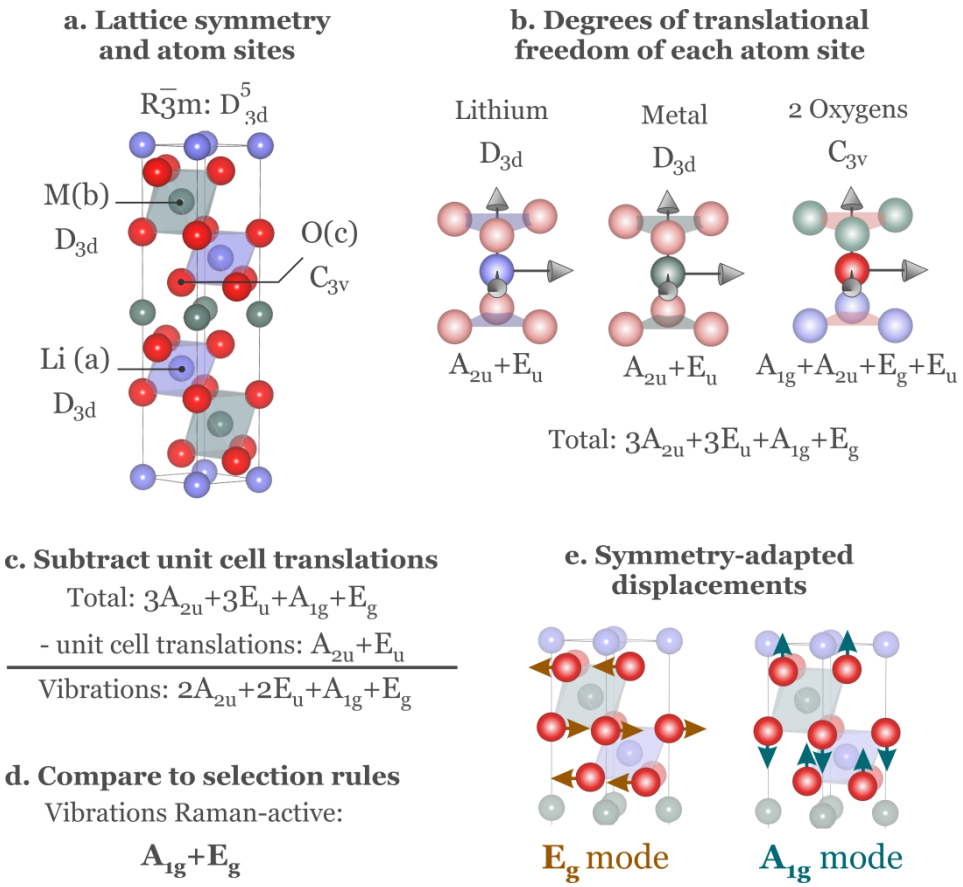

Figure 5.1. Nuclear site group analysis of the vibrational modes of $LiMO_2$. **a.** First, the translational symmetry elements of the lattice's space group $R\bar{3}m$ (Hermann-Mauguin notation) are omitted, leaving a D_{3d} (Schoenflies notation) factor group (see table 1.2 from reference [131]). The sites occupied by atoms are refined from well-resolved diffraction patterns (section 2.1) and the symmetries of these sites are found in tables (e.g. Bilbao crystallographic server, Wyckoff positions tables[166]). Li, M and O occupy sites with D_{3d}, D_{3d} and C_{3v} point symmetry, respectively. **b.** Second, the three degrees of freedom (d.f.s) of each atom are symmetrized with respect to both, the lattice's factor group and the point group of their site. Reference [130] lists these d.f. for all factor groups and all lattice sites. For instance, in $LiMO_2$ a lithium atom can move in space along a vector with A_{2u} symmetry (1 d.f.) and along a plane with E_u symmetry (2 d.f.s). Some of these d.f.s result in the translation of the cell as a whole; cell translations transform according to the *x, y, z* Cartesian vectors in the character table. **c.** For the D_{3d} point group cell translations correspond to a A_{2u} mode and a E_u mode. Once subtracted, the remaining d.f.s represent the motions of atoms relative to each other, i.e. vibrations. **d.** The D_{3d} character table shows that, from these vibrations only the A_{1g} and the E_g mode are Raman-active. The analysis can be further extended for finding a set of displacement vectors behaving according to the A_{1g} and the E_g symmetry species. **e.** The symmetry-adapted displacements of the A_{1g} and the E_g modes can be obtained by projecting arbitrary, orthogonal displacement vectors into new coordinates complying with the A_{1g} and E_g symmetry properties.[125] The symmetry-adapted A_{1g} displacement mode consists of oxygen atoms moving parallel to the *c*-axis of the lattice, at opposite directions in consecutive layers. Likewise, the E_g mode consist of the anti-parallel oxygen motion along consecutive layers.[167]

5.1.2 Testing the predictions

Figure 5.2 shows the Raman spectra of several layered oxide powders. $LiCoO_2$ displays only two Raman-active bands located at 487 and 597 cm^{-1}, just as predicted from the nuclear site group analysis (Figure 5.2a). Raman measurements of $LiCoO_2$ thin films using polarized light (section 3.3.3) show that the intensity of the band at 596 cm^{-1} has a strong dependence on the polarization of the incident radiation, so it is assigned to the totally-symmetric A_{1g} mode, while the band at 486 cm^{-1} — invariant to light polarization — is assigned to the E_g mode.[168-170] The agreement between prediction and experiment confirms that in $LiCoO_2$ each atom is surrounded by an environment with the content (type of atoms) and geometry (symmetry) expected from crystallographic measurements (Figure 5.1b).

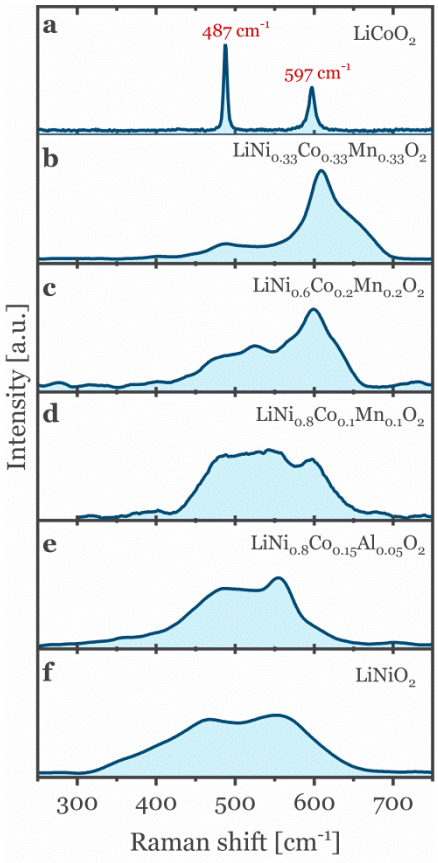

Figure 5.2. Raman spectra of commercially-relevant layered oxides powders. For clearer comparison, each profile is lightly smoothed and normalized to its own maximum intensity.

In contrast, when cobalt is completely replaced by nickel, or partially replaced by a mixture of other transition metals, the spectral profiles (Figure 5.2 b-f) widen and feature more bands than the expected A_{1g}/E_g pair of modes. The symmetry of the oxygen site is different — possibly lower — than the one at the C_{3v} site of the $R\bar{3}m$ crystallographic lattice model. These as-received powders still exhibit diffraction patterns best described by a $R\bar{3}m$ space group[171,172] but the Raman measurements clearly indicate that the oxygen environments

(and possibly that of the other atoms) are different at the local scale. At this point, nuclear site group analysis reaches its limit, because the local symmetries differ from those predicted by crystallography. As the spectral profiles complicate, many authors have resorted to phenomenological description of the spectral features, which will be discussed in the following section.

5.2 Phenomenological interpretation of the Raman spectra

Figure 5.2 shows that all lithiated Mn-containing oxides exhibit a broad band centred at 600 cm^{-1} that is absent in Mn-free oxides. The intensity of this band scales with the fraction of manganese per $LiMO_2$ formula; hence, the band clearly results from manganese substitution. The relation between spectrum and oxide composition have been generalized to the idea that the profiles in Figure 5.2b-f result from a simple combination of multiple A_{1g}/E_g pairs of bands, each originating from individual MO_6 units.[156,173] For instance, the spectrum of $LiNi_{0.33}Co_{0.33}Mn_{0.33}O_2$ (NCM111) would consist of three A_{1g}/E_g pairs, each arising from NiO_6, CoO_6 and MnO_6 units, vibrating at the frequencies found in $LiNiO_2$, $LiCoO_2$ and $LiMnO_2$, and contributing to the overall intensity in a 1:1:1 proportion.[174,175] The model supposes that the MO_6 units vibrate locally and independently, just as functional groups in large molecules (section 3.2.4). However, there are two peculiarities that suggest otherwise. First, increasing the manganese proportion in $LiMO_2$ not only increases the intensity of the bands at 600 cm^{-1} but also shifts them towards higher wavenumbers (Figure 5.2 d-b), implying thus that these vibrations are not completely independent. Second, drawing a parallel to $LiCoO_2$, the spectrum of $LiNi_{0.8}Co_{0.15}Al_{0.05}O_2$ (NCA) shows no features at 597 cm^{-1} despite having 15 % of cobalt in the structure (Figure 5.2 a and e).

Similar observations on other layered oxides[156,176] demonstrate that the phenomenological interpretation of individual MO_6 vibrating units is inaccurate. It also shows that the Raman spectra of $LiMO_2$ are rather difficult to assign and interpret, since the band positions, widths and intensities rather reflect strongly coupled vibrations affected by the complex local environments surrounding oxygen atoms. Moreover, conditions related to the sample properties (e.g. crystallite size and purity,[177] orientation[168,178] and internal stresses[179]) and the experimental conditions (e.g. temperature, light polarization and wavelength) have all been found to affect the spectra.

A more rigorous interpretation of the spectra can be achieved by comparing the experimental findings with more comprehensive models of vibrations, capable of accounting for the interatomic forces and electronic structure governing the vibration frequencies and Raman intensities. To this end, phonon calculations, based on density

functional theory, are applied for lithiated layered oxides for comparing the calculated spectra with the experimental findings. The DFT-based calculations and analysis were performed in collaboration with University of Bern (Prof. Dr. Ulrich Aschauer and Dr. Nathalie Vonrüti). A detailed description of the calculations can be found in Appendix B1.

5.3 First-principles model of $LiCoO_2$ vibrations

Figure 5.3 compares the theoretical and experimental spectrum of $LiCoO_2$. Like the symmetry-based predictions and the experimental spectrum, DFT calculations also yield only two Raman-active modes, further confirming that $LiCoO_2$ builds a highly-ordered $R\bar{3}m$ layered structure. The calculated positions show a small and systematic underestimation (20-25 cm^{-1}) of the experimentally observed wavenumbers, resulting from an underestimation of the atomic interactions that is typical of the DFT-PBE functional.[180] The DFT-derived atomic displacements confirm the E_g (487 cm^{-1}) and A_{1g} (597 cm^{-1}) band assignment based on polarization measurements. The calculated E_g/A_{1g} intensity proportion, however, disagrees with the experimental spectrum. While in most literature studies the A_{1g} band appears more intense than the E_g band,[167,168,181–185] there are exceptions that agree with the data in Figure 5.3.[186] The discrepancy might originate from distinct synthesis conditions and the state of the sample, as mentioned above.

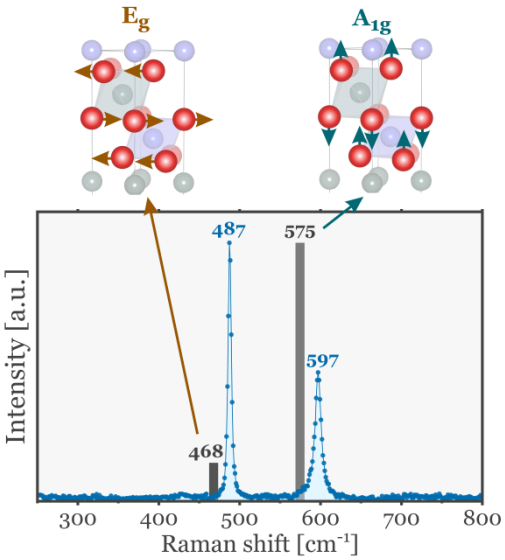

Figure 5.3. Comparison between the experimentally-measured and the DFT-calculated Raman spectra of $LiCoO_2$, along with the calculated displacement vibration patterns.

5.4 First-principles model of $LiNiO_2$ vibrations

Experimentally, the as-received $LiNiO_2$ powder is crystallographically described by a rhombohedral lattice, but our own DFT calculations and others[80] show that a monoclinic structure of $C2/m$ symmetry (C_{2h} factor group) is more energetically favourable. According to nuclear site group analysis and DFT phonon calculations, the monoclinic structure features three Raman-active modes, two of A_{1g} symmetry and one of B_g symmetry, all involving the motion of oxygen atoms only.

Figure 5.4a compares the predicted bands to the experimental Raman spectrum of $LiNiO_2$. Both spectra feature a strong band close to 560 cm^{-1} that, according to the phonon calculations, involve oxygen displacements with A_{1g} symmetry, analogous to the mode represented in Figure 5.1e. However, the displacement pattern is not completely parallel to the *c*-axis of the lattice as in the case of the $R\bar{3}m$ structure. In addition, the measured Raman spectrum features a band at 463 cm^{-1}, where the E_g band of rhombohedral $R\bar{3}m$ oxides is typically found (Figure 5.2); yet, the calculated spectrum shows no Raman activity within the same spectral range. Instead, the calculated Raman bands are placed at lower wavenumbers: 372 and 312 cm^{-1}. The former band manifests as a small shoulder in the measured Raman spectrum, but the latter band does not have any experimental correspondence. The experimentally-recorded Raman spectrum suggests that $LiNiO_2$ keeps its rombohedral lattice symmetry, despite the calculations predicting otherwise.

The contradiction between the calculated and experimental spectra does not necessarily represent a failure of the DFT-based model because the calculations inherently aim at the ground state configuration (temperature = 0 K). The structure can be monoclinic at 0 K but undergo a phase transition to a layered structure at higher temperature. Indeed, the neutron diffraction pattern of $LiNiO_2$ at low temperature (10 K) is best described by a monoclinic unit cell with $C/2m$ symmetry, while at room temperature (RT) is best refined using a $R\bar{3}m$ layered symmetry.[187] Hence, there must be a transition temperature where the monoclinic-rhombohedral phase transformation occurs.

5.4.1 Rhombohedral-monoclinic phase transition of $LiNiO_2$

Figure 5.4b shows the temperature-dependent Raman spectra of $LiNiO_2$ (experimental details in Appendix B2). The spectrum remains relatively unchanged down to -30 °C. When the temperature reaches -70 °C the band at 464 cm^{-1} sharpens and becomes slightly more intense. Similarly, two features at 360 and 286 cm^{-1} become more defined. As the temperature is lowered further, the band at 464 cm^{-1} intensifies, while the other two features develop into broad but well distinguishable bands. The bands at 360 and 286 cm^{-1}

that appear below -70 °C are very likely a signature of the monoclinic phase, since they are located fairly close to the DFT-calculated Raman bands (372 and 312 cm^{-1}). Therefore, Raman spectroscopy provides compelling evidence that $LiNiO_2$ undergoes a rhombohedral-to-monoclinic phase transition at a temperature close to -70 °C. To the best of our knowledge, these are the first experimental observations reporting a transition temperature.[187–189]

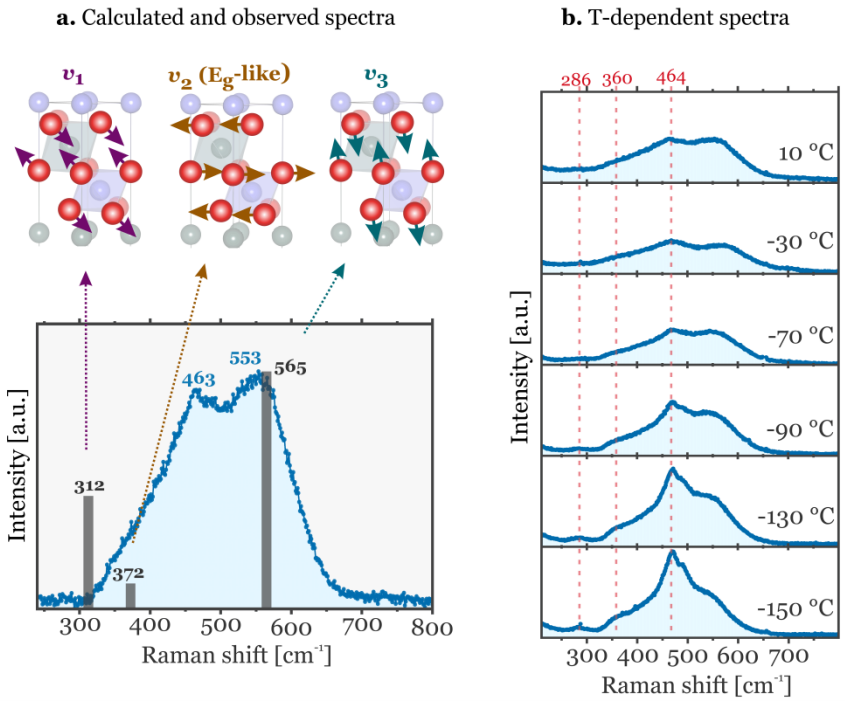

Figure 5.4. **a.** Comparison between the experimentally-measured $LiNiO_2$ spectrum and the DFT-calculated Raman spectrum of monoclinic $LiNiO_2$, along with the displacement patterns. **b.** Recorded Raman spectra of $LiNiO_2$ powder as a function of temperature.

Complementary local probes provided further clues about the nature of the phase transition. *Ex-situ* EXAFS measurements of LNO at room temperature showed that the Ni K-edge features two long and four short Ni-O distances, indicating that the NiO_6 octahedron is Jahn-Teller (JT) distorted.[190,191] As mentioned in section 2.1.1, the degenerate electronic configuration of Ni^{3+} predicts the distortion of its environment in order to remove such degeneracy. In this sense, Jahn-Teller distortion could be the driving force of the phase transition. Above the transition temperature, long and short Ni-O bonds remain randomly oriented such that, in average, all Ni-O distances are crystallographically equivalent and the lattice is better described by a $R\bar{3}m$ space group. However, below the transition temperature, long Ni-O bonds might align with each other, thus extending the distortion cooperatively throughout the lattice and lowering the lattice symmetry to a monoclinic one. The transition then occurs at the temperature where the alignment of Ni-O bonds becomes thermodynamically favourable.[80,187,192]

All attempts of reproducing the results in Figure 5.4b yield noticeable spectral changes close to -70 C; however, the bands at 360 and 286 cm^{-1} are not always observed. This limited reproducibility might be a consequence of Ni-Li site exchange. As mentioned in section 2.4.1, $LiNiO_2$ is prone to develop $[Ni_{Li}]^{\bullet}$ defects that introduce disorder into the structure. Even at small concentrations, these defects frustrate transformations to ordered thermodynamic states,[59,193] and so they could also impede the cooperative alignment of JT-distorted Ni-O bonds. Since the concentration of $[Ni_{Li}]^{\bullet}$ defects is highly sensitive to the synthesis, temperature and storage conditions of the $LiNiO_2$ powder,[194] their concentration is difficult to control and thus leads to reduced reproducibility.

5.5 First-principles model of $LiNi_{0.33}Co_{0.33}Mn_{0.33}O_2$ vibrations

5.5.1 Comparison to experimental spectrum

DFT calculations on $LiNi_{0.33}Co_{0.33}Mn_{0.33}O_2$ (NCM111) are significantly more complex than on $LiCoO_2$ and $LiNiO_2$, since the presence of three transition metals requires evaluating multiple ways of arranging them in the unit cell. Hence, many unit cells, each with different arrangement of transition metals, were relaxed to the ground state and the cell with lowest energy (labelled LE-DFT structure) was selected for the phonon calculations.

Figure 5.5 compares the experimental Raman spectrum of NCM111 with the calculated LE-DFT structure. In general the spectra are well-comparable: both feature a strong, dominant mode (measured at 600 cm^{-1} and calculated at 566 cm^{-1}) along with some small bands at lower wavenumbers with intensity ratios qualitatively comparable. The 40 cm^{-1} underestimation of the strong band is similar to that observed in $LiCoO_2$ (Figure 5.3a). In the LE-DFT spectrum, the small bands within the 390-510 cm^{-1} range envelop multiple Raman active vibrations that result in broad spectral profiles, indicating that the measured bands also hide several highly overlapping Raman active modes. The displacement patterns found in the phonon calculations are complex and resemble neither E_g nor A_{1g} type of motions of the $R\bar{3}m$ lattice; however, all modes with non-negligible Raman activity predominantly involve the motion of oxygen atoms. Only oxygen displacements are capable of modulating the polarizability of the lattice to produce detectable Raman-active vibrations.

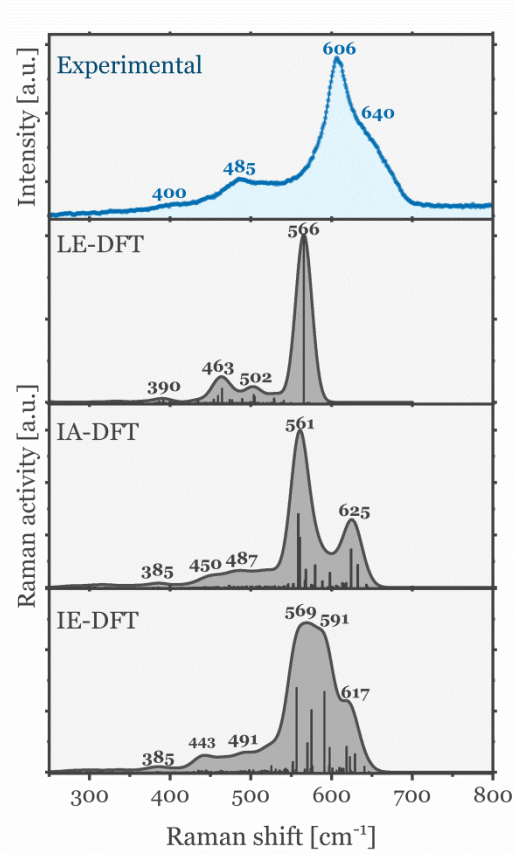

Figure 5.5. Experimentally-measured Raman spectrum of NCM111, along with the calculated spectra of the lowest-energy DFT structure (LE-DFT), the intralayer-disordered structure (IA-DFT) and the interlayer-disordered structure (IE-DFT). The IE-DFT structure exchanges M/M pair from adjacent layers, while the IA-DFT structure swaps the position of two M within the same M layer. All calculated Raman spectra were artificially broadened by 10 cm^{-1} for better comparison to the experimental spectrum.

The strong band of the measured spectrum (606 cm^{-1}) features a shoulder at higher wavenumber (640 cm^{-1}) not reproduced by the LE-DFT spectrum. The shoulder might originate from atomic configurations differing somehow from the LE-DFT structure. To explore this possibility, both inter (IE) and intra (IA) layer cation exchanges are introduced to the LE-DFT NCM111 structure, and their calculated Raman spectra are compared in Figure 5.5. The IE-DFT structure exchanges a M/M pair from adjacent layers, while the IA-DFT structure swaps the position of two M within the same M layer. Figure 5.5 shows that both types of exchange result in Raman-active vibrations above 600 cm^{-1}. From an energetic perspective, the IA-type of disorder is slightly more probable to occur at room temperature than the IE-type of disorder, since the calculations show that the IA structure (- 56 meV/formula) is more energetically stable than the IE structure (-44 meV/formula). However, at the temperatures typically used for the synthesis of these oxides (> 600 °C) the energy difference between lattice configurations can be easily surmounted, such that both types of disorder are likely to be present in the as-synthesized material.

5.5.2 Local structure of NCM111

The good agreement between the calculated and experimental spectrum validate the LE-DFT structural model as a good approximation of the local atomic environments in the as-received NCM111 powder. Hence, the LE-DFT lattice is studied in detail for obtaining meaningful insights into the properties of the synthesized material.

5.5.2.1 Oxidation states of transition metals. The oxidation states of each transition metal can be computed from their magnetic moments. Each unpaired electron in M contributes *S*=1/2 Bohr magnetons (μB) of spin momentum to the total momentum μ.[74] Hence, μ(M) can be used to estimate the number of M *d*-electrons arranged in the octahedrally split t_{2g} and e_g bands (see section 2.1) and so the oxidation state of M. The calculated magnetic moments of all nickel atoms in the unit cell is μ(Ni) = 1.76 μB, which approaches the value of 2 μB expected for a Ni$[t_{2g}]^6[e_g]^2$ (S=1) configuration. Likewise, all μ(Co) = 0.03 ~ 0 μB and all μ(Mn) = 3.22 ~ 3 μB, indicating Co$[t_{2g}]^6[e_g]^0$ (S=0) and Mn$[t_{2g}]^3[e_g]^0$ (S=3/2) configurations, respectively. Therefore, all nickel, cobalt and manganese atoms are found in 2+, 3+ (low-spin) and 4+ oxidation states, respectively. These results evidence the transfer of one electron associated with manganese to nickel as discussed in section 2.1.1, which are also in agreement with previous calculations[84] and X-ray absorption spectra[45,85,195].

5.5.2.2 Oxygen's nearest neighbours. In an ideal $R\bar{3}m$ structure with no cation disorder all Li and M are coordinated to six oxygen atoms, while oxygens are coordinated to three Li and three M (see Figure 5.1b). If M would distribute randomly, there would be ten possible combinations of M occupying the first coordination shell of oxygen, namely Li_3-O-Ni_3, Li_3-O-Co_3, Li_3-O-Mn_3, Li_3-O-Ni_2Co, Li_3-O-Ni_2Mn, Li_3-O-$NiCo_2$, Li_3-O-$NiMn_2$, Li_3-O-Co_2Mn, Li_3-O-$CoMn_2$, and Li_3-O-NiCoMn. However, in the calculated LE-DFT structure, oxygen is exclusively surrounded by one nickel, one cobalt and one manganese atom (i.e., a Li_3-O-NiCoMn environment). No transition metal repeats in the closest neighbourhood of an oxygen atom. This configuration is only realized if the transition metals are ordered within the M layer.

Figure 5.6a shows the view of the NCM111 LE-DFT lattice along the *c*-axis. It is clear that transition metals order into a repeating pattern of Ni-Co-Mn triangles. The bidimensional pattern — often described in Wood's notation[196] as a [√3 × √3]R30° superlattice — has also been predicted by other first principles calculations. Intralayer M ordering seems driven by the strong clustering tendency of Ni^{2+} and Mn^{4+}.[84,197–199] Experimentally, characterization techniques probing the local order, such as EXAFS and electron diffraction, have found evidence of [√3 × √3]R30° superlattice features.[85] However, long-range order probes find

inconclusive[200] or no evidence of transition metal ordering.[59] Therefore, the triangular Ni-Co-Mn pattern of NCM111 shown in Figure 5.6a remains short-ranged, likely due to the disruptions that $[Ni_{Li}]^{\bullet}$ defects cause in the ordering of the transition metal layers.[59]

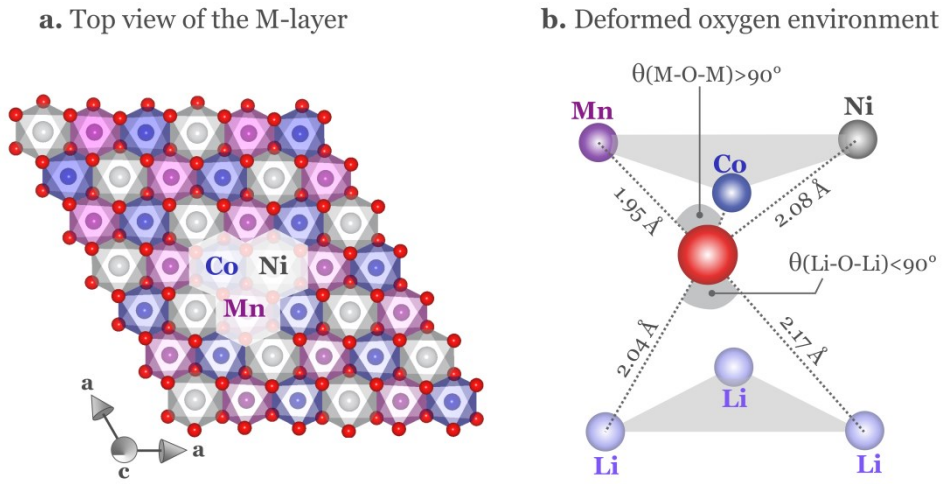

Figure 5.6. **a.** Top view of the transition metal (M) layer in the calculated LE-DFT lattice. Cobalt, nickel and manganese arrange in a bidimensional triangular pattern that repeats over the whole layer. **b.** Spatial arrangement of oxygen's nearest neighbours in the LE-DFT lattice. Oxygen atoms are found closer to the transition metal layer, bonded to each M at the preferred distance of the particular M oxidation state. Li-O distances adapt such that diametrical M-O-Li lengths keep a constant value of 4.12 Å. The proximity of oxygen to the M layer widen the M-O-M angles and shut the Li-O-Li angles.

5.5.2.3 Geometry of oxygen's nearest neighbours. The distances and angles of oxygen to its nearest neighbours are computed from the LE-DFT structure in order to investigate the geometry of oxygen's first coordination shell. The calculated distances and angles are shown in Appendix B3 and summarized in Table 5.1. The M-O distances are in very good agreement with the experimentally-found M-O distances for Ni^{2+} (2.08 Å), low-spin Co^{3+} (1.95 Å) and Mn^{4+} (1.94 Å),[84,201] confirming thus the valence assigned to all M in the previous section, solely based on the magnetic moments.

Table 5.1. Summary of bond distances and angles calculated from the LE-DFT structure.

Atom pair	Bond distances [Å]
Ni-O	2.08
Mn-O	1.94
Co-O	1.95
Li-O1	2.04
Li-O2	2.17

Atom triplet	Bond angle [°]
Li-O-Li	86
Co-O-Mn	96
Ni-O-Mn	93
Ni-O-Co	92

The Li-O distances distribute around two values as shown in Table 5.1. When looking at the calculated structure is noted that Li-O1 bonds are collinear to Ni-O bonds, while Li-O2 bonds are collinear to both Mn-O and Co-O bonds. Interestingly, the total length of these collinear bonds is constant; e.g. Li-O1 (2.04 Å) + Ni-O (2.08 Å) = Li-O2 (2.17 Å) + Co-O (1.97 Å) = 4.12 Å. Li-O distances seem to be buffering the geometrical distortions introduced by multiple M-O distances, probably due to the ionic and thus non-directional nature of the Li-O interactions. Note the similarity of the Ni-O (2.08 Å) and short Li-O (2.04 Å) distances, which facilitates the interlayer migration of Ni^{2+} to Li^{+} sites left vacant due to synthesis defects or delithiation.[106,107]

All M-O-M angles are obtuse (> 90°) and all Li-O-Li angles are acute (< 90°). The angles subtended between atoms in different layers exhibit similar trends (Appendix B3). The bond distances and angles found describe a deformation where oxygen atoms approach the M layer and move away from the Li layer. As a consequence, the shorter M-O distances open the M-O-M angles, while the long Li-O distances shut the Li-O-Li angles (Figure 5.5b). These distortions might originate from i) the strain of accommodating edge-sharing MO_6 octahedra with different volumes and/or ii) magnetic exchange interactions between transition metals.[74]

5.6 Raman resonant enhancement

As mentioned in section 3.3.4, resonance-enhanced Raman bands can be used to explore the electronic structure of a material. Resonance Raman effects have previously been measured on $LiNiO_2$,[202] $LiCoO_2$[183] and $LiNi_{0.5}Mn_{1.5}O_4$.[203] Thus, the Raman resonance effects of some commercially-relevant positive electrode materials are here explored, with the aim of assisting the spectra interpretation and clarifying the evolution of their electronic structure on cycling. The methodology of all the measurements in this section is described in Appendixes B4 and B5.

5.6.1 Wavelength-dependent Raman spectra of $LiMO_2$

Figure 5.7a shows the Raman spectra of layered oxide powders recorded with 785 nm (near infrared), 633 nm (red) and 532 nm (green) laser excitation wavelengths. The spectrum of NCM111 features a band at 530 cm^{-1} that only appears under the 785 nm laser excitation, while the band at 600 cm^{-1} grows a shoulder towards lower wavenumbers when the sample is irradiated with the green laser. Some weak features distinguished close to 1000 cm^{-1} most likely originate from overtone bands. Similar features are observed in the wavelength-dependent spectra of the other layered oxides. For instance, NCM622 display bands near 600 cm^{-1} that appear strong and sharp under the red and green excitation. Also, under the green laser excitation, NCM811 and NCA — sharing the same nickel proportion — feature an enhanced band at 563 cm^{-1}. At exactly twice the wavenumber of this band, NCA also exhibits a strong and sharp overtone band at 1126 cm^{-1}. In LNO the Raman band at 523 cm^{-1} also appears stronger when moving to shorter wavelengths and exhibits weak but observable overtones between 700 and 1200 cm^{-1} for all excitation wavelengths. At this point it is necessary to confirm whether the Raman bands feature wavelength-dependency as a consequence of optical absorptions from electronic excitations.

5.6.2 Optical absorptions of $LiMO_2$

Figure 5.7b shows the UV-Vis spectra of the layered oxide powders recorded in diffuse reflectance mode (Appendix B5). All spectra exhibit two weak but noticeable absorptions at 630 and 560 nm. NCM111 shares with LNO a strong absorption in the near infrared region (λ > 700 nm), while it shares with NCM622 a weak absorption band close to 400 nm. When the Raman excitation wavelengths are superimposed in the plot, it is clear that the three laser probes fall near electronic absorptions of $LiMO_2$. Therefore, several Raman bands in 5.7a are resonance-enhanced. Since all laser excitations might enhance the Raman signals, it is difficult to identify non-resonant bands that can act as reference to study resonant bands. Such identification requires further measurements of the non-resonant Raman spectrum of the oxides by using a laser excitation either well below (far infrared) or well above (far UV) the electronic transition energies.

The electronic transitions behind the absorptions in Figure 5.7b might originate from several processes. Ligand-metal transitions could occur, where electrons occupying states of oxygen character (see Figure 2.1b) are promoted to partially-empty states of transition metal character. In addition, *d-d* transitions are also possible, where electrons at t_{2g} *d*-states are promoted to partially-filled e_g^* *d*-states (both of M character) by surmounting the octahedral-field splitting gap Δ_O.[7] The absorption of light in the 350-800 nm (3.5-1.5 eV) range of the spectrum likely originates from *d-d* transitions, since the DFT-calculated Δ_O gaps are in the 0-3 eV range; in contrast, ligand-metal transitions are predicted to consume more than 4 eV.[53,75,170,204]

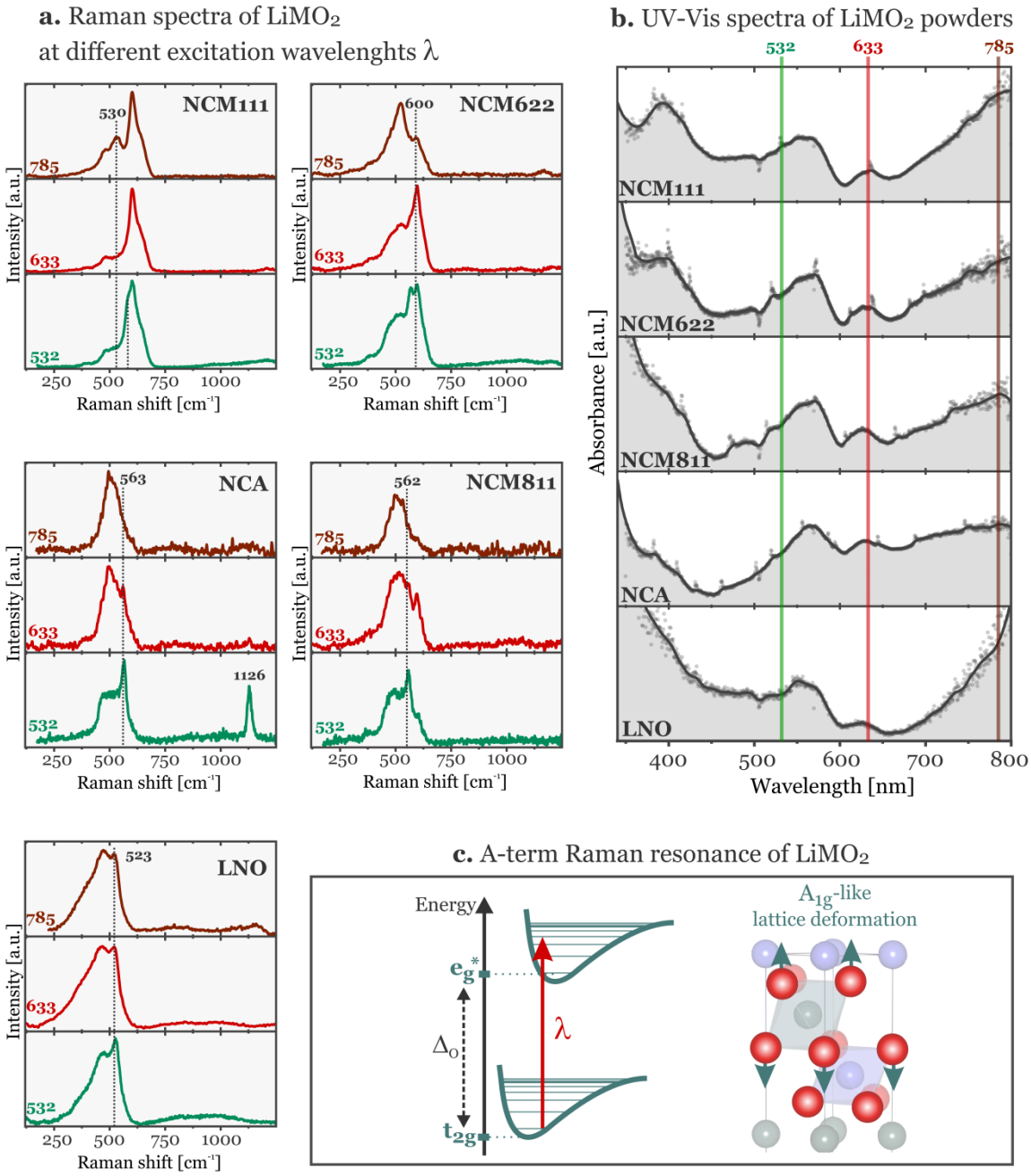

Figure 5.7. **a.** Raman spectra of $LiMO_2$ powders using 785, 633 and 532 nm excitation wavelengths. **b.** UV-Vis spectra of $LiMO_2$ powders in diffuse-reflectance mode; superimposed, the laser excitation wavelengths used to record the Raman spectra in Figure 5.7a. **c.** A-term Raman resonance of $LiMO_2$. Certain excitation wavelengths λ promote a t_{2g}-e_g^* electronic transition by surmounting the octahedral field splitting gap Δ_O, which enhance the Raman activity of totally symmetric A_{1g}-like modes. In the electronically-excited state, the lattice is partially deformed following an A_{1g}-like pattern, i.e. it is expanded/contracted along the *c*-axis.

5.6.3 Raman-resonance effect in $LiMO_2$.

The spectral features observed in Figure 5.7a-b possess three key characteristics. First, most wavelength-dependent Raman bands appear in the 520-600 cm^{-1} region, where totally-symmetric vibration modes are expected to occur (A_{1g}-like modes in Figure 5.3 and Figure 5.4). Second, overtone bands are observed, sometimes of comparable intensity to the fundamental bands as in the case of NCA. Third, the electronic excitations induced by the laser wavelength consist of *d-d* transitions. These findings confirm an A-term Raman resonance enhancement (see section 3.3.4 and Figure 5.7c), implying that i) the excitation energy of the laser promotes an electronic transition of the oxides, ii) the transition changes the spatial arrangement of atoms but does not affect the symmetry of the lattice, and iii) the electronically-excited lattice exhibits a geometry change that includes a A_{1g}-like displacement, i.e. it is expanded/contracted along the *c*-axis.

Resonance enhancements from electronic *d-d* transitions are of particular interest since these orbitals control the physico-chemical properties of $LiMO_2$ (section 2.1.1). The previous findings indicate that alterations on *d*-electron density result in changes of the lattice parameters and volume, particularly along the *c*-axis (Figure 5.7c). Similar effects might occur when the *d*-electron density is modified during (de)lithiation of the oxide. These lattice changes, if repetitive and extensive, lead to particle strains and eventually to mechanical disintegration of the active material (section 2.4). In this context, the Raman-resonant spectra provide insights into the electronic structure of $LiMO_2$, its potential evolution upon cycling and its role on the eventual deterioration of the lattice.

5.7 Summary

In this chapter symmetry-based (nuclear site group analysis) and DFT-based lattice models are formulated for predicting and describing the Raman-active vibrations of $LiMO_2$. Compared to phenomenological approaches, the comparison between predictions and experiment enable a more systematic, accurate and comprehensive interpretation of the spectral features. $LiMO_2$ lattices with $R\bar{3}m$ symmetry are predicted to exhibit only two Raman-active modes, reflecting oxygen displacements only. While $LiCoO_2$ adopts an almost ideal $R\bar{3}m$ lattice structure, substituting cobalt in $LiMO_2$ results into Raman spectra with many more bands than expected by nuclear site group analysis, despite still being crystallographically described by a $R\bar{3}m$ lattice. These findings highlight the sensitivity of Raman spectroscopy to the short-range structure of the oxides. In $LiNiO_2$, comparisons between measured and DFT-calculated spectra suggest that the material adopts a monoclinic lattice at low temperature, and the monoclinic-rhombohedral phase transition is confirmed to occur close to -70 °C according to temperature-dependent Raman measurements of $LiNiO_2$. The remarkable agreement between calculated and measured

spectrum validates the LE-DFT model of NCM111, where all nickel, cobalt and manganese atoms are found in 2+, 3+ (low-spin) and 4+ oxidation states, respectively. The transition metals exhibit intralayer ordering, forming a short-ranged [√3 × √3]R30° superlattice. Intra and interlayer disorder in NCM111 manifest in the Raman spectrum as a shoulder experimentally observed at 640 cm^{-1}. All $LiMO_2$ oxides here studied exhibit Raman resonance-enhancement features corresponding to *d-d* electronic transitions, which enhance the totally-symmetric Raman modes via an A-term resonance enhancement mechanism (section 3.3.4). The electronically excited lattice partially deforms following an A_{1g}-like pattern, i.e. it is expands/contracts along the *c*-axis. All these conclusions will be leveraged in the following chapters for interpreting the evolution of the Raman spectra of $LiMO_2$ during cycling.

Chapter 6 *Operando* Raman spectroscopy of Li_xCoO_2

$LiCoO_2$ is the most widely used cathode material for batteries in portable applications, and as such, it has been subject of intense study. Many authors have reported the evolution of the Raman spectra of $LiCoO_2$ during cycling but the results have been only phenomenologically interpreted. Hence, the spectral trends have remained as a scientific curiosity rather than utilized for characterizing the operation and stability of the cathode material. In this context, the case of $LiCoO_2$ represents an excellent starting point for demonstrating the descriptive power of the methodology developed in this PhD work, and for finding spectrum-property relationships able to provide mechanistic insights into the cycling behaviour of the cathode. This chapter starts with a general description of the electrochemical characteristics of $LiCoO_2$ and the phase transition providing most of the reversible specific charge of the cathode. Later, the evolution of the Raman spectra of $LiCoO_2$ is presented along with the fitted peak heights of both Raman active modes. These results are followed by a critical assessment on the physical properties controlling the spectral trends. Last, we show how these detailed trends can be used to investigate the kinetics and reversibility of the phase transition.

6.1 Electrochemical profiles and phase transition

Figure 6.1a shows the constant current profile of a $LiCoO_2$ composite electrode as a function of lithium content *x*, along with the differential charge plot. The delithiation-lithiaton hysteresis is not negligible, evidencing overpotentials even at the slow cycling rate used (10 mA/g). The initial plateau-like region of the electrode potential at a high state of lithiation (SOL) manifests as a well-defined redox couple around 3.90 V in the differential charge plot, highlighting an ongoing phase transition. X-ray diffraction reveals the coexistence of two hexagonal phases in the $0.93 > x > 0.75$ SOL region,[205] implying the occurrence of a miscibility gap. Therefore, delithiation through the gap proceeds as a first-order phase transition, where a $Li_{0.93}CoO_2$ phase is depleted while a $Li_{0.75}CoO_2$ phase grows (Figure 6.1b).

Both immiscible phases share the same $R\bar{3}m$ lattice symmetry and have slightly different lattice parameters but contrasting electronic behaviour. According to NMR and electric measurements, the $Li_{0.93}CoO_2$ phase features localized electron holes and behaves as an insulator, while delocalized holes provide metallic-like conduction properties to the $Li_{0.75}CoO_2$ phase.[206,207] DFT calculations indicate that the holes become localized when they interact with a dilute concentration of lithium vacancies, and this interaction is strong enough to drive phase separation.[96] It is anticipated that Raman spectroscopy will provide further insights into the metal-insulator phase transition as the improved time resolution enables the investigation of the miscibility gap within narrow compositional intervals.

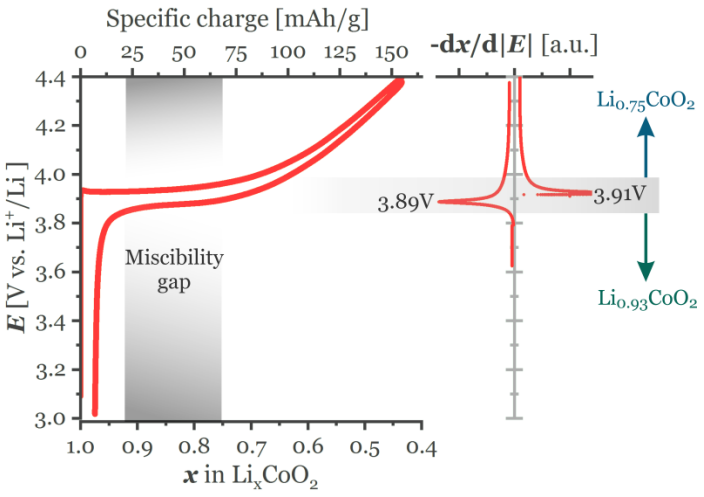

Figure 6.1. Galvanostatic cycling potential profile and the corresponding differential charge profile of Li_xCoO_2 during the first cycle in the Raman cell (3.0- 4.3 V *vs.* Li^+/Li, 10 mA/g). Sharp redox peaks close to 3.9 V originate from a first-order metal-insulator phase transition. The miscibility gap occurs within the $0.93 > x > 0.75$ SOL interval.

6.2 *Operando* Raman spectra

Figure 6.2 shows the spectral overview describing the cycling-dependent behaviour of the Raman-active bands of a $LiCoO_2$ particle within the composite electrode. The band located at 487 cm^{-1} has been assigned to the E_g vibrational mode while the band at 596 cm^{-1} to the A_{1g} mode (section 5.1.2). The most noticeable feature of the landscape is the fading of both $LiCoO_2$ bands quickly after delithiation starts, and their complete absence for most of the cycle. The bands reappear approaching the end of re-lithiation but with reduced intensity. These general trends have been reported in the literature[168,184,185] but here the improved time resolution and spectral quality enables a detailed analysis of the spectral trends.

The E_g and A_{1g} bands have been fitted using Lorentz-type profiles via the automated fitting procedure described in section 4.5. Figure 6.3 shows the fitted peak intensities of the E_g and A_{1g} bands of LCO during the first cycle and as a function of the state of lithiation *x*. Both bands behave remarkably similar, suggesting they respond to the same underlying physical phenomenon. Just after the delithiation starts ($1.0 > x > 0.99$) the bands lose almost 60 % of their initial intensity; subsequently they progressively fade until reaching noise levels when the state of lithiation (SOL) drops below 0.93. On lithiation, however, the bands reappear for SOL above 0.75 and they rapidly grow until reaching a constant intensity for $x > 0.77$. The resulting pattern outlines a clear charge-discharge hysteresis.

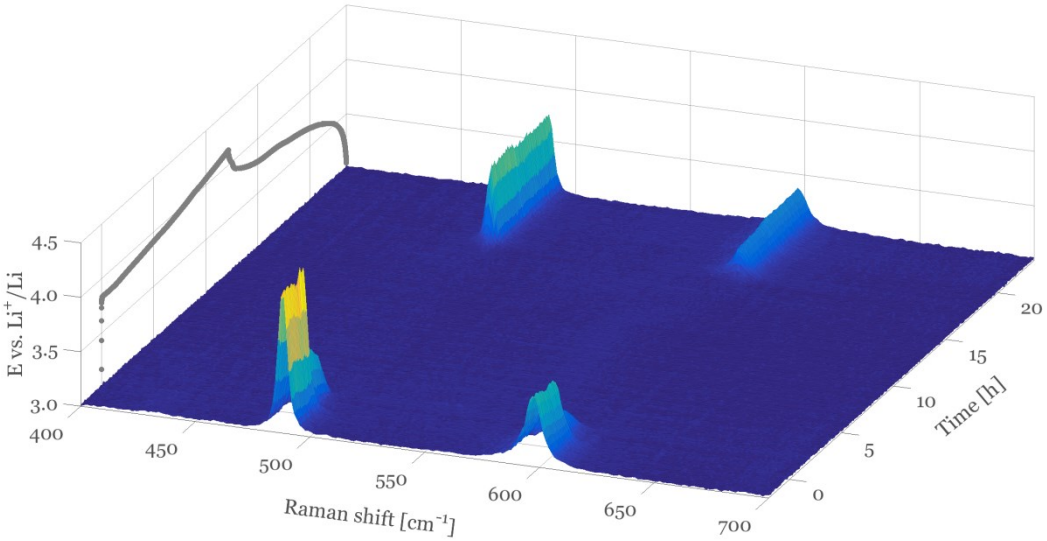

Figure 6.2. Coloured surface map representing the evolution of the Raman spectrum of Li_xCoO_2 during the time of one galvanostatic cycle. The cycling potential profile is plotted in the left plane.

The attained high time resolution enables a precise identification of the SOL marking the disappearance (x=0.93) and reappearance (x=0.75) of the bands (Figure 6.3). The main finding of the experiment is that these values are the same SOL values defining the boundaries of the $Li_{0.93}CoO_2$ and $Li_{0.75}CoO_2$ phase coexistence. Therefore, the behaviour of the Raman bands is clearly related to the phase transition.

Phase transitions are typically detected as changes in the number of Raman-active bands, since the two immiscible phases usually exhibit different lattice symmetries.[208] In the present case, however, the transition from the insulator to metallic phases manifests rather as an abrupt drop of intensity of both Raman-active bands.

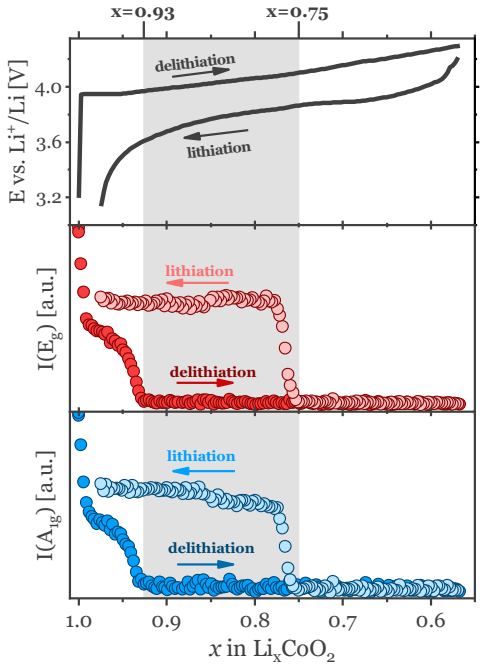

Figure 6.3. Galvanostatic potential profile along with the fitted peak intensities of the E_g and A_{1g} bands of Li_xCoO_2 as a function of SOL. The miscibility gap is highlighted in the shadowed area.

6.3 Physical mechanisms of intensity variations

From the variables affecting the Raman intensity (Equation 3.9), there could be multiple properties differentiating the Raman intensity of the insulator and the metallic phase. It is unlikely, though, that the polarizability change induced by both modes would be affected drastically and simultaneously during the phase transition, considering that both phases have the same composition and almost identical lattice structures. Likewise, as the unit cell of both phases feature $R\bar{3}m$ symmetry, the number N_m of Raman-active vibrations per unit cell is not expected to vary. The sudden and synchronous disappearance of the bands seems rather the result of processes hindering the access of the incident intensity I_0 into the Raman-active sample. The following sections discuss multiple possible mechanisms potentially weakening I_0, attempting to quantify the extent of light attenuation based on basic physical models.

6.3.1 Light attenuation by free charge carriers

When light interacts with a conductive material, radiation is mostly elastically scattered away, as the electric field accelerates the free charge carriers (electrons or holes) in the sample creating electric currents.[150] Only a small fraction of the incident radiation penetrates the material, quickly weakening as it travels axially into the sample. Given that

the metallic phase $Li_{0.75}CoO_2$ is three orders of magnitude more conductive than the insulator phase $Li_{0.95}CoO_2$,[206,209] many authors have suggested that the metallic phase features significantly weaker Raman signals due to its high electronic conductivity.[168,184,185,210,211] This hypothesis is investigated using a physical model capable of quantifying light penetration and comparing the outcome to the trends in Figure 6.3.

Light attenuation due to dielectric effects is described classically by the concept of skin depth, defined as the penetration distance it takes to reduce light intensity to $1/e$ (~ 37% of the initial intensity). Solving Maxwell equations for an electromagnetic wave of frequency ν, in a material with electric permittivity ε, magnetic permeability μ and electronic conductivity σ, the skin depth D_{skin} can be approximated as:[150]

$$D_{skin} \cong \frac{2}{\sigma}\sqrt{\frac{\varepsilon}{\mu}} \qquad \text{Equation 6.1}$$

Equation 6.1 is valid for poorly conducting materials; more specifically, in the limit where $\sigma << 2\pi\nu\varepsilon$.[150] Given the laser probe frequency of 474 THz (633 nm), assuming the permittivity of $LiCoO_2$ to be the calculated in the high frequency limit ($\varepsilon = \varepsilon_\infty = 15\varepsilon_0$)[212], and assuming the magnetic susceptibility to be negligible ($\mu = \mu_0$)[213,214], Equation 6.1 is valid when the conductivity is well below 10^3 S/cm.

Since regions of the sample that are not illuminated do not scatter Raman signals, Equation 6.1 can be used to estimate the size of the illuminated portion of the sample — the sampling volume — as a function of the electronic conductivity. Note that the sampling volume is not only limited by the electronic conductivity but also by the depth of focus determined by the confocal optics, which was estimated in section 4.1 to be 4.2 µm for our experimental setup. Hence, the Raman intensities are controlled by the shorter of these two depths (Figure 6.4a). Using Equation 6.1 the skin depth is here calculated at ν = 473 THz (633 nm), under the same previous assumptions about ε, μ and the conductivity values found in the literature. In general, the values of electronic conductivity of cathode materials are known to vary largely according to the methodology employed and the state of the sample.[49] A literature survey (references [206,207,209,215,216]) locate the conductivity of the insulator phase within the range of $1x10^{-5}$ and $3x10^{-3}$ S/cm; Figure 6.4b shows that for these values the calculated skin depth is in the order of centimetres and even meters of penetration. Hence, the sampling volume in the insulating phase is solely limited by the confocal depth of focus. The situation is different for the metallic phase: given the conductivity values found in literature (between 1 and $1x10^2$ S/cm) light penetration might be shallower than the 4.2 µm confocal depth (Figure 6.4b, right plot). Therefore, the sampling volume shrinks, reducing the amount of probed material and thus the number of collected Raman scattering events.

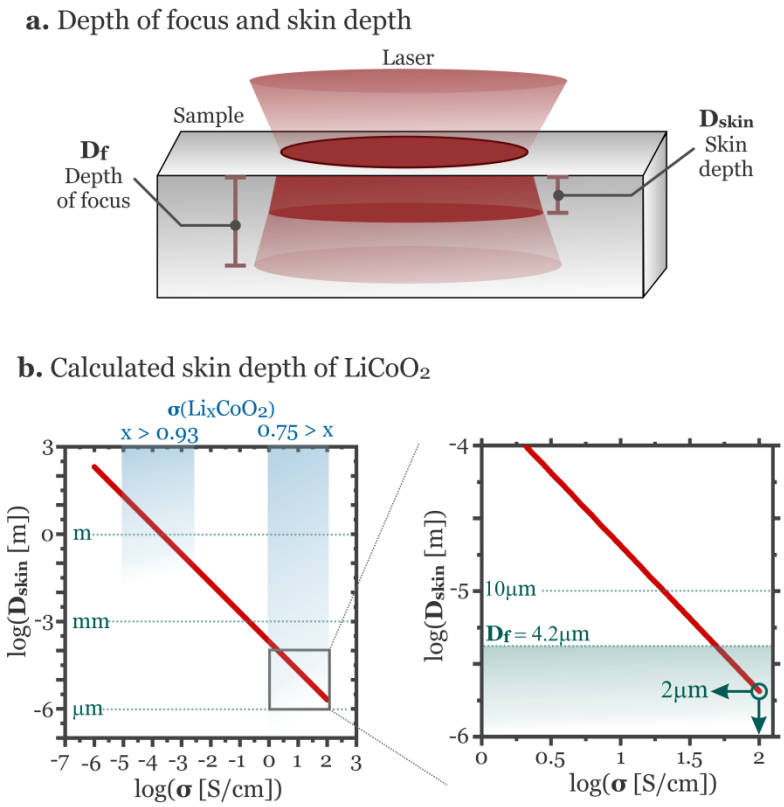

Figure 6.4. **a.** Schematic representation of light penetration into the sample. For non-conducting samples sampling volume is solely limited by the confocal depth of focus. For conducting samples, the skin depth limits the sampling volume. Regions of the sample excluded from laser illumination do not scatter Raman light. **b.** Calculated skin depths as a function of electronic conductivity. An enlargement into the conductive regime (plot in the right) shows that the skin depth limits the sampling volume when conductivity approaches 10^2 S/cm.

The model demonstrates how increased electronic conductivity leads to weakened Raman signals. However, several authors have reported Raman spectra with intense bands on sub-micrometre-thin films of $LiCoO_2$, even when the thickness of the films (< 1 μm) is shallower than both the confocal and skin depths in Figure 6.4b.[217,218] Therefore, none of these depths (Figure 6.4a) seem to be the limiting factor reducing the intensity of the Raman bands. The skin-depth model implicitly assumes that the sample is a semiconducting material with no optical absorption in the visible range of the spectrum. In reality, the sample might exhibit optical absorption and so influence the disappearance of the Raman signals; this possibility is investigated next.

6.3.2 Light attenuation by optical absorption

The intensity of the incident light can also be attenuated as it is absorbed when promoting transitions between electronic states of the material. The phenomenon can be empirically described using the Beer-Lambert law[7] that yields an expression similar to Equation 6.1, i.e. a penetration depth where light intensity is reduced to $1/e$ of its initial intensity. However, in the present case attenuation results from electronic excitations, so it depends on the absorption coefficient γ characteristic of the electronic transition and dependent on the photon frequency υ:

$$D_{absorption} \equiv \frac{1}{\gamma(\upsilon)} \qquad \text{Equation 6.2}$$

$LiCoO_2$ features multiple optical absorptions in the visible range[219] that likely correspond to *d-d* electronic transitions (section 5.6.2). These absorption bands are predicted[20] and experimentally-observed[170] to evolve during cycling. Using spectroscopic ellipsometry analysis, Liu et al. have determined the absorption coefficient of Li_xCoO_2 at multiple wavelengths.[170] The reported values of γ at 633 nm (1.96 eV) are summarized in Table 6.1, together with the absorption depths calculated from Equation 6.2.

Table 6.1. Reported[170] optical absorption coefficients (at 2.0 eV = 620 nm) and the corresponding absorption depths of Li_xCoO_2 at several SOL.

x in Li_xCoO_2	Absorption coefficient [cm^{-1}]	$D_{absorption}$ [nm]
0.83	1.0×10^5	100
0.72	2.5×10^5	40
0.53	3.0×10^5	33
0.43	2.0×10^5	50

All the absorption depths in Table 6.1 are well below both the confocal and skin depths values in Figure 6.4; therefore, optical absorption seems to be the main process leading to light attenuation. Unfortunately, it is not possible to directly compare Raman intensities with the penetration depths derived from absorption coefficients, since the Raman intensities in Figure 6.3 are negligible for all the lithium compositions spanned in Table 6.1. Confirming a relation between optical absorption and Raman intensity requires further measurements of the absorption coefficient of Li_xCoO_2 within the $1.0 > x > 0.93$ compositional range, where reliable Raman intensity data is available.

6.3.3 Other factors influencing light attenuation

Given the micrometre-sized crystallites of the $LiCoO_2$ particles probed, the behaviour of light at grain boundaries (e.g. increased reflectance) might become a major factor influencing light attenuation.[144] In addition, the intensity of both Raman-active bands of $LiCoO_2$ is

known to be wavelength-dependent, i.e. to be resonance-enhanced.[183] Hence, an optical absorption at the wavelength of the laser probe could attenuate light intensity and simultaneously enhance Raman scattering. Therefore, a better understanding on the disappearance of both bands in Figure 6.2 would require accurate measurements of light penetration into single-crystal films of Li_xCoO_2 before (x > 0.93) and after (0.75 > x) the phase transition and using multiple laser wavelengths.

6.3.4 *Operando* experiments in the literature

The Raman spectral trends of $LiCoO_2$ during cycling have been extensively studied in the literature. Unlike our findings, some authors still detect the E_g/A_{1g} pair of bands when $x < 0.75$. At SOL below 0.75 the bands appear weakened, broadened and red-shifted.[181,182,220,221] With enough spectral resolution, the apparent broadening is resolved as a splitting into a new pair of Raman active bands,[168,222,223] accordingly assigned to the E_g and A_{1g} Raman active modes of the also $R\bar{3}m$ $Li_{0.75}CoO_2$ metallic phase. Several authors argue that the new pair of bands appear red-shifted because the $Li_{0.75}CoO_2$ lattice is larger than the $Li_{0.93}CoO_2$ lattice.[168,222] A literature search reveals that all experiments where any Raman band is observed when $x < 0.75$ used a green excitation laser (514 or 532 nm),[168,181,182,220,221,223,224] while our experiments (no bands when $x < 0.75$) are performed using a red excitation laser (632 nm). As mentioned above, $LiCoO_2$ features an optical absorption band at 590 nm,[219] and the Raman spectrum of the fully lithiated material has been found to be resonance-enhanced with a green (532 nm) excitation laser.[183] Therefore, the Raman bands of the metallic phase might only be detectable if they are resonance-enhanced by a green excitation laser.

6.4 Hysteresis of Raman intensity trends

Another remaining question is the origin of the delithiation/lithiation hysteresis of the Raman intensities observed in Figure 6.3. Independently of the physical mechanism, strong Raman bands can be confidently associated to the presence of the insulating $Li_{0.93}CoO_2$ phase, while weak or non-existent bands indicate the presence of the metallic $Li_{0.75}CoO_2$ phase. Hence, the hysteresis implies that the disappearance of the insulating phase (the apparent Raman scatterer) during delithiation and its reappearance during lithiation do not occur at the same SOL. There are two types of SOL heterogeneities that can explain the observed hysteresis.

6.4.1 Inter-particle heterogeneity

The SOL of the particle probed might differ from the calculated average SOL of the composite electrode (Figure 6.5a). Hence, the Raman signal response of the particle on delithiation might appear delayed with respect to re-lithiation. SOL heterogeneity develops when secondary particles of active material are electronically isolated from the conductive network of the composite electrode, as a consequence of several degradation phenomena such as retreat of the carbon conductive additive[155] or particle cracking[218]. Raman compositional maps[182,225] and X-Ray microscopy[226] confirm the presence of electrochemically inert particles of active material distributed laterally and axially throughout the composite electrode.

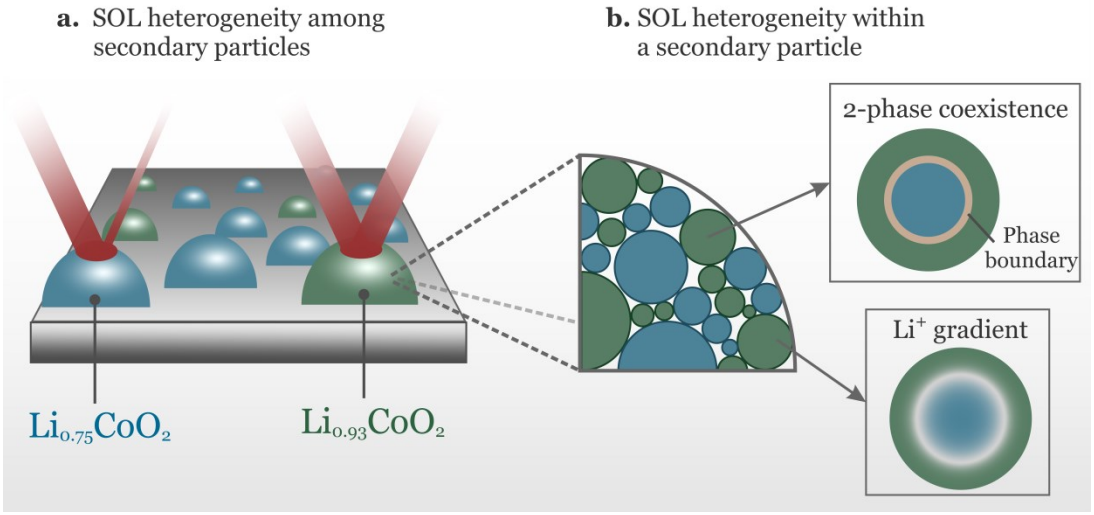

Figure 6.5. Possible kinetic effects causing the delithiation-lithiation hysteresis of Raman band intensities. **a.** SOL heterogeneity among secondary particles. Isolated particles do not experience the same SOL as the electrode average. **b.** SOL heterogeneity within a secondary particle. The secondary particle is an agglomerate of primary particles, which could exhibit diverse SOL from particle-to-particle, intraparticle lithium gradients and/or intraparticle two-phase coexistence.

6.4.2 Intra-particle heterogeneity

The laser-probed secondary particle is an agglomerate of nm-sized primary particles,[227] which might exhibit a spatially-heterogeneous SOL as a consequence of slow lithium diffusion and/or a sluggish phase transformation kinetics (Figure 6.5b).[99] Consequently, the Raman bands might become (un)detectable even when the phase transition has not been completed throughout the probed secondary particle.

Experiments at higher cycling rates could elucidate the origin of the hysteretic intensity trends. (De)lithiating the composite electrode at higher currents would evidently enhance interparticle SOL heterogeneity and intraparticle lithium gradients, due to slow Li^+ diffusion in the electrolyte and within the particle's bulk (see Figure 2.2). However, it is not

straightforward that higher imposed currents could have an effect on the dynamics of the first-order phase transition.[228] Therefore, preliminary *operando* experiments at higher cycling currents have been performed in an attempt to pinpoint the origin of the hysteresis in Figure 6.3. Different $LiCoO_2$-based composite electrodes have been cycled at higher rates and the Raman intensity trends are presented in Figure 6.6. Unexpectedly, the (de)lithiation hysteresis narrows when the cycle rate is doubled from 10 mA/g to 20 mA/g, and becomes negligible when the electrode is cycled four times faster (i.e. at 40 mA/g).

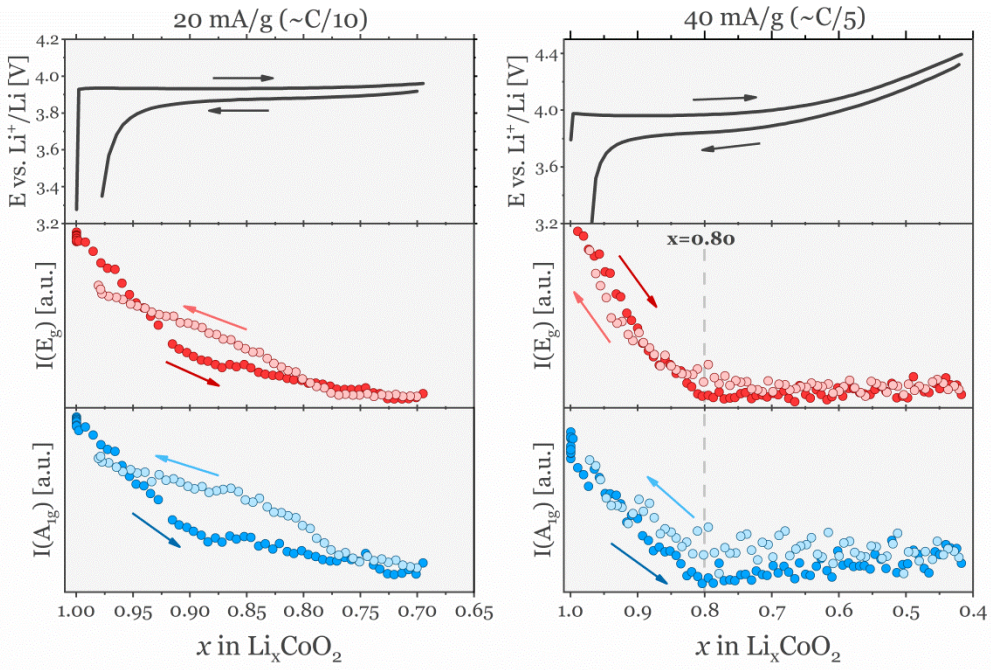

Figure 6.6. Galvanostatic profiles and the evolution of the E_g and A_{1g} fitted peak intensities of Li_xCoO_2 cycled at 20 mA/g (left) and 40 mA/g (right).

These results are evidently incompatible with kinetic limitations arising solely from slow Li^+ diffusion. Recently, Matsuda et al. reported a similar hysteresis in the Raman peak position trends of an $LiCoO_2$ thin-film electrode in a solid-state cell during cycling.[224] The hysteresis appears when measuring the side of the film facing the solid electrolyte but does not appear when measuring the side facing the current collector. Their observations confirm a SOL heterogeneity through the Li_xCoO_2 film, which they attributed to a sluggish propagation of the phase boundary between $Li_{0.93}CoO_2$ and $Li_{0.75}CoO_2$.[224]

While the results shown in Figure 6.3 and Figure 6.6 demonstrate the suitability of *operando* Raman spectroscopy for investigating the kinetics of phase transitions, more experiments are needed before drawing in-depth conclusions from the data. Ideally, *operando* experiments at various rates should be performed on the same particle, in order to discard

interparticle heterogeneity effects; such experiments, however, are challenging given that the Raman signal quality quickly deteriorates after the first cycle (at least it does using a 633 nm excitation laser). In addition, the cycling stopping conditions must be the same for all experiments, since the dynamics of the phase transition might be affected by the cycling cut-off potential.[229]

6.5 Reversibility of the phase transition

Originally the phase transition was believed to be irreversible since the measured electronic conductivity on Li_xCoO_2 thin films remains high after complete re-lithiation, suggesting that the insulator phase is not recovered.[209,230,231] If this would be the case, i.e., if re-lithiation would stop at any SOL within the $0.93 > x > 0.75$ range, the coulombic efficiency of $LiCoO_2$ (ratio of specific charges after delithiation and re-lithiation) would be no greater than 93 %. In contrast, the electrochemical measurements in Figure 6.1 show coulombic efficiencies above 97 %. The Raman experiments in Figure 6.3 and Figure 6.6 also indicate that a fraction of the insulator phase (strong Raman scatterer) has been recovered as the Raman bands partially gain intensity at the end of the re-lithiation. The recovery of the Raman intensities have been documented in composite electrodes previously,[185,223] as well as in thin films even after 200 cycles.[218] These findings and those in the literature are in line with the known remarkable cycling stability of LCO.[232]

The apparent contradiction between the conductivity measurements and the Raman intensity trends seems to be related to the diverse length scales probed by these techniques. As discussed previously, inter-particle heterogeneity introduces variations between local (single-particle Raman intensity) and collective (electronic conductivity) electrode properties. At the end of re-lithiation many individual particles might recover the insulator phase, but a sufficient proportion of delithiated metallic-like particles can still create a percolation network that renders the electrode highly conductive. Therefore, the recovery of the insulator phase at the end of re-lithiation might remain overlooked, unless it is identified using a technique with sufficient spatial resolution such as confocal Raman spectroscopy.

6.6 Summary

Operando Raman measurements of Li_xCoO_2 ($1.0 > x$ 0.6) have been performed during the first cycle. The automated fitting procedure of all spectra allowed a detailed analysis of the intensity evolution of both Raman-active bands as a function of SOL. The Raman band intensities weaken abruptly and simultaneously when delithiation starts, completely disappearing until the end of the delithiation; thereafter, the bands reappear at the end of re-lithiation. Enabled by an improved time resolution, it is demonstrated that the

disappearance/appearance of the bands occurs at the same lithium contents delimiting the miscibility gap between the $Li_{0.93}CoO_2$ and $Li_{0.75}CoO_2$ phases. Hence, the Raman intensities clearly respond to the insulator-metal phase transition of Li_xCoO_2. A critical assessment of multiple physical mechanisms potentially controlling the cycling-dependent evolution of the Raman band intensities was formulated. Based on physical models, the skin depth limits light penetration to several micrometres, whereas optical absorption attenuates light intensity after 100 nm. Consequently, the Raman signals likely fade when the metallic $Li_{0.75}CoO_2$ phase undergoes an optical absorption at the wavelength of the laser probe. The Raman bands of the metallic phase might still be detected after the phase transition due to resonance-enhancement. A hysteresis develops between the Raman intensity trends on delithiation and lithiation, which suggests kinetic limitations of the composite electrode associated to the dynamics of the first-order phase transition. The partial recovery of Raman intensity of the bands at the end of re-lithiation indicates that the phase transition is reversible, agreeing with the known remarkable stability of $LiCoO_2$ during long-term cycling.

Chapter 7 *Operando* Raman spectroscopy of Ni-rich $LiMO_2$ oxides

$LiNi_{0.8}Co_{0.15}Al_{0.05}O_2$ (NCA) and $LiNi_{0.8}Co_{0.1}Mn_{0.1}O_2$ (NCM811) are both highly attractive Ni-rich oxides for automotive applications due to their high storage capacity and energy efficiency. Unfortunately, their attractive performance metrics fade quickly during cycling and come at the risk of detrimental cell failure. Electrochemical degradation has been related to the cyclic phase transformations these materials undergo during continuous cycling. In this chapter the *operando* Raman spectra of both NCA and NCM811 are discussed, by firstly analysing the main spectral features and later by interpreting them based on first-principles calculations in combination with complementary studies. Once the spectrum-property relationships have been established, the cycling-dependent spectral trends reveal the occurrence and nature of multiple phase transitions, including those leading to the irreversible degradation of the active material. Some excerpts of this chapter have been published by **E. Flores**, N. Vonrüti, U. Aschauer, P. Novák, E.J. Berg, *Chem. Mater.* (2018), 30, 14, 4694-4703[171] and reproduced in part with permission of Chemistry of Materials, submitted for publication (2019).

7.1 Electrochemistry

The electrochemical profile is a foremost indicator of the occurrence of phase transitions (section 2.3.1). Figure 7.1 shows the constant-current and differential charge profiles of NCA (left) and NCM811 (right) during the 2nd cycle, set between 3.0 and 4.3 V *vs*. Li^+/Li and at a 10 mA/g rate. These materials have a characteristic activation process, most of which ends after the first (pre)cycle,[172] therefore, the second cycle is more representative of the intrinsic reversible electrochemical reactions of the oxides during their lithiation/delithiation (profiles of other cycles shown in appendix B6). During the precycle, the dissolution of a nm-thin surface layer of Ni-rich oxides occurs, when the oxidizing electrode potential is increased during the first delithiation. The layer consists of $(Li_2/Ni)CO_3$ and/or other inorganic species (such as LiOH) that are residuals from the synthesis and/or are formed after air (humidity) exposure of the powder during storage/handling. The formation and irreversible dissolution of these layers are mostly responsible for the permanent loss of cycleable Li^+, represented by the shaded rectangles in Figure 7.1.[233,234] Despite the initial Li^+ loss, both materials still deliver ~218 mAh/g with comparatively small overpotential hysteresis.

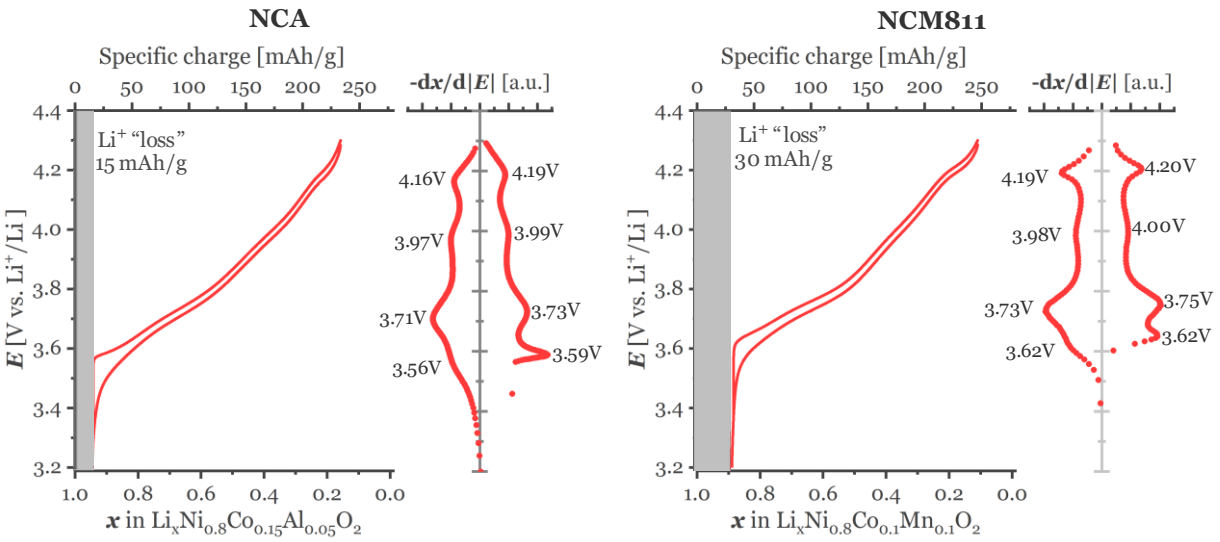

Figure 7.1. Galvanostatic potential profiles and the corresponding −dx/|dE| curves of NCA and NCM811 during the second cycle (3.0–4.3 V *vs.* Li^+/Li).

Figure 7.1 also shows the differential charge profiles of both Ni-rich oxides. NCA and NCM811 differ by their Co content and the substitution of Al by Mn; yet, their redox profiles are virtually identical. Both exhibit 4 redox couples occurring at very similar electrode potentials. Evidently, the phase transitions behind the redox peaks are intrinsic to the Ni-rich nature of the oxides. For comparison, *in situ* X-Ray diffraction of Li_xNiO_2 (100% nickel) reveals that the oxide cycles through multiple miscibility gaps between phases labelled as H1 (hexagonal), M (monoclinic), H2 and H3.[235] The miscibility gaps manifest as a redox couples centred at 3.63 (H1->M), 4.01 (M->H2) and 4.17 (H2->H3) V *vs.* Li^+/Li,[235] and compare well to the peaks in Figure 7.1. First-principles studies indicate that these phase transitions are configurational (section 2.3.2).[95] Therefore, many authors assume that the phase transitions of Ni-rich oxides are of similar nature to the ones observed in $LiNiO_2$. However, *in situ* X-Ray diffraction has failed in identifying miscibility gaps in NCA and NCM811 (80% nickel); both oxides rather (de)lithiate following a solid solution mechanism, i.e., only one phase is observed to cycle.[47,48,234] The H and M phases might be too similar to be resolved by separate Bragg reflections in the substituted oxides; instead, they might manifest as subtle peak broadenings.[47,48] In section 5.4.1 it was demonstrated that Raman spectroscopy is capable of resolving the monoclinic and rhombohedral phases of $LiNiO_2$; hence, it is anticipated that the Raman spectra of Ni-rich oxides will provide similar hints about the occurrence and nature of the phase transitions.

7.2 General features of the *operando* Raman spectra

Interpretation of the cycling dependent Raman spectra of Ni-rich oxides requires an accurate assignment of all experimentally detected Raman-active bands. Figure 7.2a shows the Raman spectra of individual NCA and NCM811 particles within the composite electrode, as recorded in the Raman cell at open circuit potential (OCP), i.e. before enforcing any external potential to the electrodes. The spectrum of NCA can be well-fitted with two peaks at 503 and 564 cm^{-1}, assigned in the literature to the E_g and A_{1g} vibrational modes, respectively, which are expected for the $R\bar{3}m$ lattice (section 5.1.1).[167] Instead, the spectrum of NCM811 requires at least three peaks for fitting the weak Raman signals. As discussed in section 5.5, disordered oxygen environments increase band multiplicity; in particular, the peak at 604 cm^{-1} is a feature common of Mn-containing oxides.

Figure 7.2b-c show how these bands evolve during three cycles, along with their corresponding constant-current profiles. When an external potential is applied, the spectra of both oxides evolve as a consequence of the delithiation/lithiation process; the spectral trends are clearly a function of the state of lithiation (SOL). In general, the weak and broad Raman profiles of the lithiated oxides grow progressively during delithiation and convert into a strong pair of bands, which weaken again reversibly on re-lithiation. The spectra of both oxides evolve remarkably similarly during cycling, indicating that the spectral trends are also intrinsic to the Ni-rich nature of the cathode materials, and that the two intense bands exhibited by both oxides likely share common physical origin. Accordingly, the bands at 482 and 540 cm^{-1} in NCM811 (Figure 7.2a) are also labelled as E_g and A_{1g} modes of vibration, respectively. Note that while this assignment is not completely accurate due to the unknown local symmetry of NCM811, it enables direct comparison to the assigned bands of NCA.

The surface maps in Figure 7.2b-c entail spectral details that are further analysed using several sample spectra, shown in Figure 7.3. Upon delithiation (x < 1.0), the relative intensities of the bands increase, while their position undergo subtle changes. Note that the Raman spectrum of NCA develops some bands above 600 cm^{-1} that were not detectable in the lithiated state (highlighted with a star in Figure 7.3). In Figure 7.2b the bands appear as shoulders in the 600-650 cm^{-1} region and disappear again on re-lithiation. These bands in NCA cannot be Mn-related as in NCM811 because NCA is a Mn-free oxide. Although the Raman spectra of NCA were previously reported to be recorded *in situ*,[160] the improved spectral quality from our experimental setup enables for the first time resolving these bands. However, their origin remains unclear, so it is further discussed in the following section.

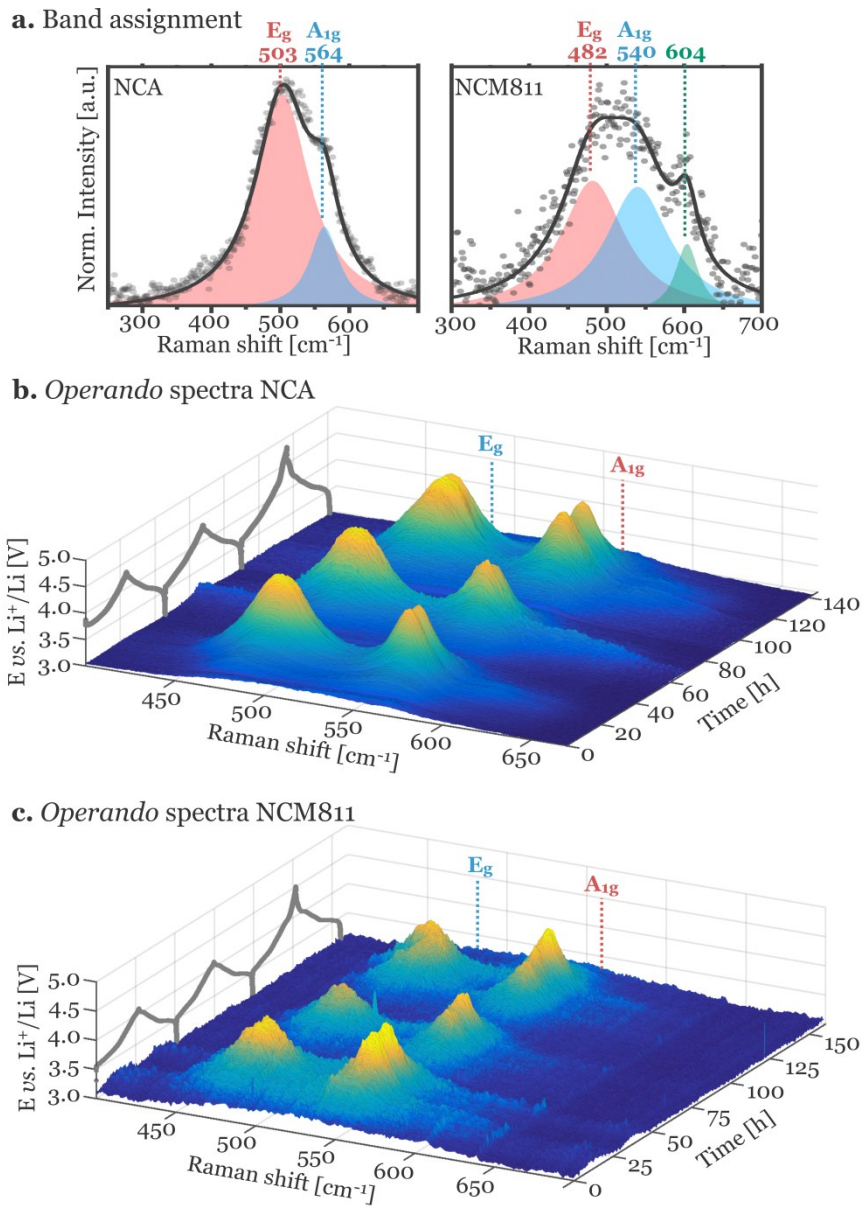

Figure 7.2. **a.** Raman spectra of a single NCA and NCM811 particles at OCP, together with the respective band assignments. Coloured surface maps of the spectral evolution of **b.** NCA and **c.** NCM811 during two standard cycles (3.0-4.3 V) and a third overcharge cycle (3.0-4.8 V). The maps are tridimensional representations build from each recorded spectrum (Raman shift and intensity in the horizontal and vertical axes, respectively) sorted along the time direction (depth axis). The corresponding galvanostatic potential profiles are plotted in the left plane, while the assigned E_g and A_{1g} bands are labelled in the back-plane of the map.

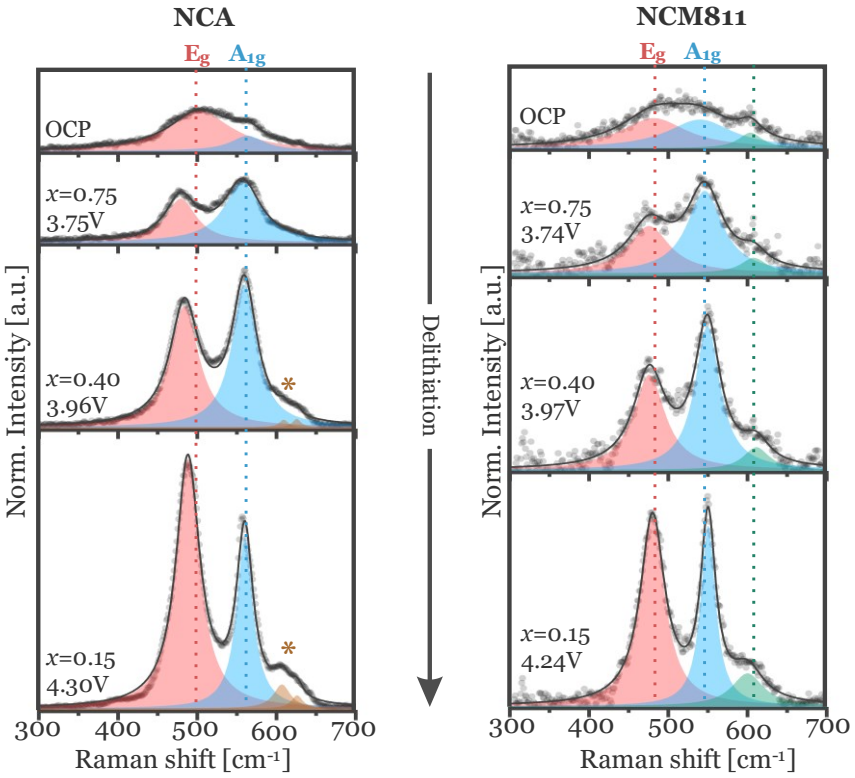

Figure 7.3. Raman spectra of NCA and NCM811 at multiple SOL during the second cycle (3.0–4.3 V): OCP, *x*=0.75, 0.40 and 0.15.

7.3 Investigation of the origin of NCA bands above 600 cm^{-1}

There are several possible sources of new Raman-active bands of NCA during the *operando* experiment, which can be either extrinsic or intrinsic to the active material.

7.3.1 Organic decomposition products

Decomposition reactions chemically or electrochemically triggered at the particle interface can leave Raman-active side-products that might accumulate at the cathode's surface and become detectable during the experiment (see section 2.4.2). Organic species, such as alkyl chlorides (derived from the $LiClO_4$ salt) and alkyl carbonates originating from the decomposition of organic electrolyte[110] feature Raman-active vibrations within the 600-650 cm^{-1} range.[236] While the dynamics of the layers formed from these byproducts is still poorly understood, they generally accumulate at the surface of the cathode,[237–240] instead of (dis)appearing cyclically as indicated by the results on Figure 7.2b. Hence, the bands seem rather unrelated to decomposition byproducts.

7.3.2 Reconstructed interphases

Julien and Camacho-Lopez have shown that lithium manganese oxide with spinel structure feature bands within the 600-650 cm^{-1} region that also grow in intensity during delithiation.[241] As mentioned in section 2.4.1, the surface of NCA and other Ni-rich oxides develops nm-thin reconstructed surface layers with spinel-like (Fd3m) structure when polarized to high potentials. Therefore, if the Raman signals of these layers are strong, they might cause appearance of the Raman bands above 600 cm^{-1}. The exact stoichiometry of the surface layers has not been determined, so it is not possible to compare them with the known compounds. However, heating the delithiated oxide particles above 200 °C drives the transformation of NCA into the same spinel phase.[242] In a complementary study here performed, the delithiated NCA powder has been heated to 500 °C to trigger the formation of these layers, and their recorded Raman spectra has been compared to the bands observed during cycling (details in appendix B7). Even if the heat treatment triggered the transformation to the spinel-like phase, the Raman spectrum of such phase does not feature bands within the 600-650 cm^{-1} range. Therefore, the bands above 600 cm^{-1} do not originate from reconstructed spinel-like interphases.

7.3.3 Lattice symmetry lowering

During delithiation of $LiMO_2$ the formation of lithium vacancies and the oxidation of the transition metals might modify the symmetry of the lattice. As mentioned above, diffraction techniques might not distinguish the transformed lattice from the initial one. However, these symmetry changes, even if subtle, might introduce new Raman-active vibrational modes such as the ones observed above 600 cm^{-1}. Hence, DFT phonon calculations are here performed using the $LiCoO_2$ and $Li_{0.5}CoO_2$ structural model (justification in appendix B8) for investigating the symmetry-lowering hypothesis. Figure 7.4 compares the calculated and measured Raman spectra of LCO and NCA, respectively. Both spectra are well comparable, establishing the suitability of the DFT-based LCO structural model and supporting the E_g (503 cm^{-1}) and A_{1g} (564 cm^{-1}) band assignment proposed in the literature.[167] Notably, the calculated Raman spectrum of delithiated LCO predicts the appearance of a new Raman-active band located at 623 cm^{-1}. The vibration pattern of the new band resembles the A_{1g} vibrational mode common of $R\bar{3}m$ oxides but shows stronger displacements toward Li^+ vacant sites. A new Raman-active vibrational degree of freedom is indicative of the transformation of the local oxygen symmetry, and the DFT calculations clarifies that such transformation is introduced by lithium vacancies.

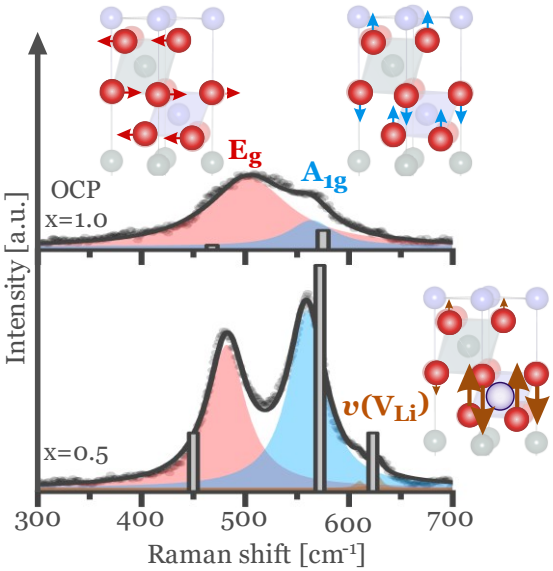

Figure 7.4. Comparison between the experimental Raman spectra of NCA (curves) and DFT-calculated spectra of Li_xCoO_2 (grey bars) at OCP and x=0.5, along with the displacement patterns of each assigned band according to the phonon calculations. The DFT-$Li_{0.5}CoO_2$ structure features a new vibrational mode at 623 cm^{-1}, involving strong A_{1g}-like displacements towards vacant lithium sites.

At this point it is possible to tentatively assign all bands observed in NCA and NCM811; these assignments are summarized in Table 7.1. Again it is noted that the E_g and A_{1g} labelling is used for drawing parallels between compounds and they are only accurate if oxygen atoms are in a C_{3v} symmetry site (section 5.1.1). With the bands assigned, is now possible to analyse comprehensively the spectral trends during cycling.

Table 7.1. Band assignment of the spectra of lithiated Ni-rich oxides.

Wavenumber range [cm^{-1}]	Oxide	Assignment
480-500	NCA	E_g mode: oxygen displacements along oxygen layer.
	NCM811	
550-565	NCA	A_{1g} mode: oxygen displacements parallel to c-axis.
	NCM811	
600-650	NCA	A_{1g}-like displacements of oxygen atoms neighbouring vacant Li^+ sites.
	NCM811	Two bands: one Mn-related band and another Li-vacancy related.

7.4 Spectral trends during cycling: fitted peak positions

The fitting procedure outlined in section 4.5 is applied to each spectrum in Figure 7.2b-c. Figure 7.5 shows the fitted peak positions $P(E_g)$ and $P(A_{1g})$ of the two main Raman active bands of NCA (Figure 7.5a) and NCM811 (Figure 7.5b) during two standard cycles (3.0-4.3 V) and a third overcharge cycle (3.0-4.8 V). Overcharging of layered oxides is well-known to be detrimental for their performance, as the degradation processes discussed in section 2.4 aggravate at high electrode potentials.[109,243–245] Hence, the spectral trends on overcharge are also investigated in the search for specific Raman spectroscopic signatures related to degradation.

Based on the band assignments in Table 7.1, the behaviour of the E_g and A_{1g} bands should be sensitive to cycling-related changes along the oxygen layer and along the *c*-axis of the lattice, respectively. Figure 7.5a shows that, in NCA during all cycles, $P(E_g)$ follows a U-shape trend with a minimum close to x = 0.7, whereas $P(A_{1g})$ is generally displaced to higher wavenumbers. In particular, during the third (overcharge) cycle, the $P(A_{1g})$ trend reaches a maximum at x = 0.15 and again decreases upon further delithiation. In NCM811 (Figure 7.5b) the trends are generally similar to the observed in NCA but the U-shaped $P(E_g)$ trend is less pronounced. Notably, most spectral changes are highly reversible, since the trends during delithiation are almost superimposed to the trends during re-lithiation. The only exception is the $P(A_{1g})$ trend in NCA during overcharge (Figure 7.5a, cycle 3) which features a small but noticeable delithiation-lithiation hysteresis. Further interpretation of the trends requires identifying the physical phenomena driving these changes.

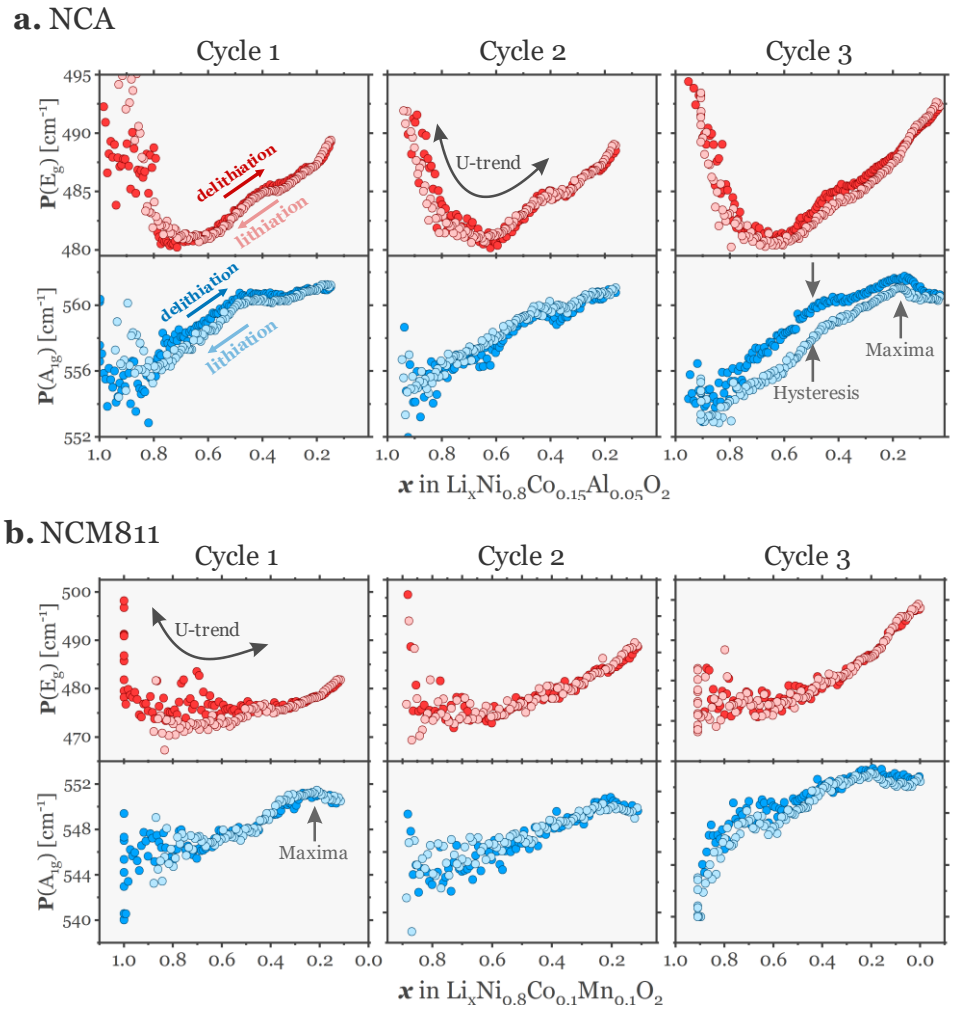

Figure 7.5. Fitted peak positions *P* of the E_g and A_{1g} Raman bands of **a.** NCA and **b.** NCM811 as a function of state of lithiation *x*, during two standard cycles and a third overcharge cycle. The arrows highlight the key features of these trends that are discussed.

7.4.1 Understanding peak position changes

Since the Raman-active vibrational modes of $LiMO_2$ originate from displacements of oxygen atoms (section 5.5.1), variations in the frequencies (or wavenumbers) of these modes reflect variations in the interatomic forces pinning oxygen atoms to their lattice sites (section 3.1). These forces also act for all other atoms to build a preferred lattice configuration, so many authors have conceptually connected the vibration frequencies to the crystallographic lattice parameters, understanding that both observables originate from the same underlying interactions.[167,173,175,202,246] Based on this interpretation, intense interatomic forces that keep atoms closer together and thus build smaller unit cells, oppose atomic displacements strongly and hence result in higher vibrational frequencies. Likewise, weak forces resulting in larger unit cells give rise to lower vibrational frequencies. However, the crystallographic lattice parameters are long-range averages of atomic configurations that might deviate in the short-range. Since the vibrational modes are primarily sensitive to

short-range atomic environments (section 3.2.4), the *x*-dependent variations in peak position might appear decoupled from the cycling-dependent changes in the crystallographic lattice parameters.

Appendix B9 summarizes a supplementary study of the relation of the peak position with parameters from the crystallographic and first-principles model of the NCA lattice. The results indeed confirm that the peak position trends are decoupled from the trends in the crystallographic *a* and *c* lattice parameters. Instead, DFT calculations indicate that the U-shaped trend of $P(E_g)$ likely results from a crossover of two phenomena: an initial bond softening due to lithium vacancy formation ($x > 0.7$) and a later continuous bond hardening due to the oxidation of the transition metal. The DFT calculations also attribute the increase of $P(A_{1g})$ during delithiation to the increased M-O covalency, which results from removing electrons from antibonding e_g^* states. Based on the previously described spectrum-property relationship, the two main features of the $P(A_{1g})$ trends can now be interpreted.

First, the overcharge hysteresis of the $P(A_{1g})$ trend in NCA (Figure 7.5a, cycle 3) indicates that the M-O bond is slightly but irreversibly weakened after cycling at high potentials. Since the trend hysteresis is only observed in $P(A_{1g})$, the NCA lattice seems to degrade anisotropically, i.e. preferentially along the *c*-axis. Ni-rich oxides are known to undergo an abrupt contraction along the *c*-axis at low SOL, which precedes the mechanical deterioration of the particles (section 2.4.3).[172,247] In this context, the trend hysteresis in $P(A_{1g})$ is a spectroscopic signature of such degradation process, indicating that the *c*-axis contraction occurs together with an irreversible change in M-O covalency. Notably, the minor (if not negligible) hysteresis on the $P(A_{1g})$ trend of NCM811 (Figure 7.5b) implies that the structural changes of the Mn-containing oxide are less severe. Such an effect would agree with the reported higher stability of NCM over NCA against, for instance, particle cracking.[248]

The second feature is the trend maxima that $P(A_{1g})$ reaches close to x=0.2, observed in NCA on overcharge (Figure 7.5a, cycle 3) and somewhat weaker in NCM811 (Figure 7.5b) during all three cycles. At this point, it can only be said that i) the M-O bond does not strengthen further when delithiation proceeds below x=0.2, ii) the effect seems anisotropic given that it manifests only in the A_{1g} mode, and iii) the inflection does not necessarily anticipates irreversibilities, since $P(A_{1g})$ in NCM811 exhibits negligible hysteresis. Later in this chapter, these findings will be discussed in relation to electronic transformations of the lattice.

7.4.2 Fine structure of peak position trends

Further examination of the highly resolved *P* profiles in Figure 7.5 reveals that the trends are not monotonic but rather display many minor plateaus. These plateaus are more easily

discerned when examining the derivative of the band position trend with respect to the lithium content. Figure 7.6 shows the differential charge curves of NCA and NCM811, along with the trends in peak positions and their derivatives $-dP/dx$. The plateaus in P appear as minima in the $-dP/dx$ curves. When these minima are cross-correlated with the differential charge curves, the plateaus clearly coincide with the electrochemical redox peaks of the oxides. In NCA (Figure 7.6a) all four labelled redox peaks correlate to minima in the $-dP/dx$ profiles. In NCM811 (Figure 7.6b) the trends are more scattered, but the redox peak at 3.73 V correlates clearly to a plateau in $P(E_g)$ and $P(A_{1g})$, while the peaks at 3.98 V and 4.19 V correlate to minima in the $-dP/dx$ profiles of both bands.

Understanding the described correlations requires considering that both P and E are related to the lattice energy. On one hand, the electrode's potential E is proportional to the derivative of the lattice energy g with respect to the lithium content x (Equation 2.3), and E plateaus when a minimum in g generates a miscibility gap (see Figure 2.3). On the other hand, the frequency of a normal mode P depends on the second derivative of the lattice energy with respect to the atomic displacement q (Equation 3.1 and Equation 3.2). Therefore, the *operando* experiment can be viewed as a probe of a lattice energy surface, built from both the lithium content and the atomic displacement of the normal mode (Figure 7.6c). The partial slope of this surface along the lithium content axis x is proportional to the electrode potential E, while the partial slope along the atomic displacement axis q relates to the frequency of the normal mode P. The occurrence of a phase transition will therefore manifest as a minimum in the lattice energy surface, in which case both E and P exhibit plateaus simultaneously. This argument demonstrates how the fine structure of P responds to the occurrence of phase transitions.

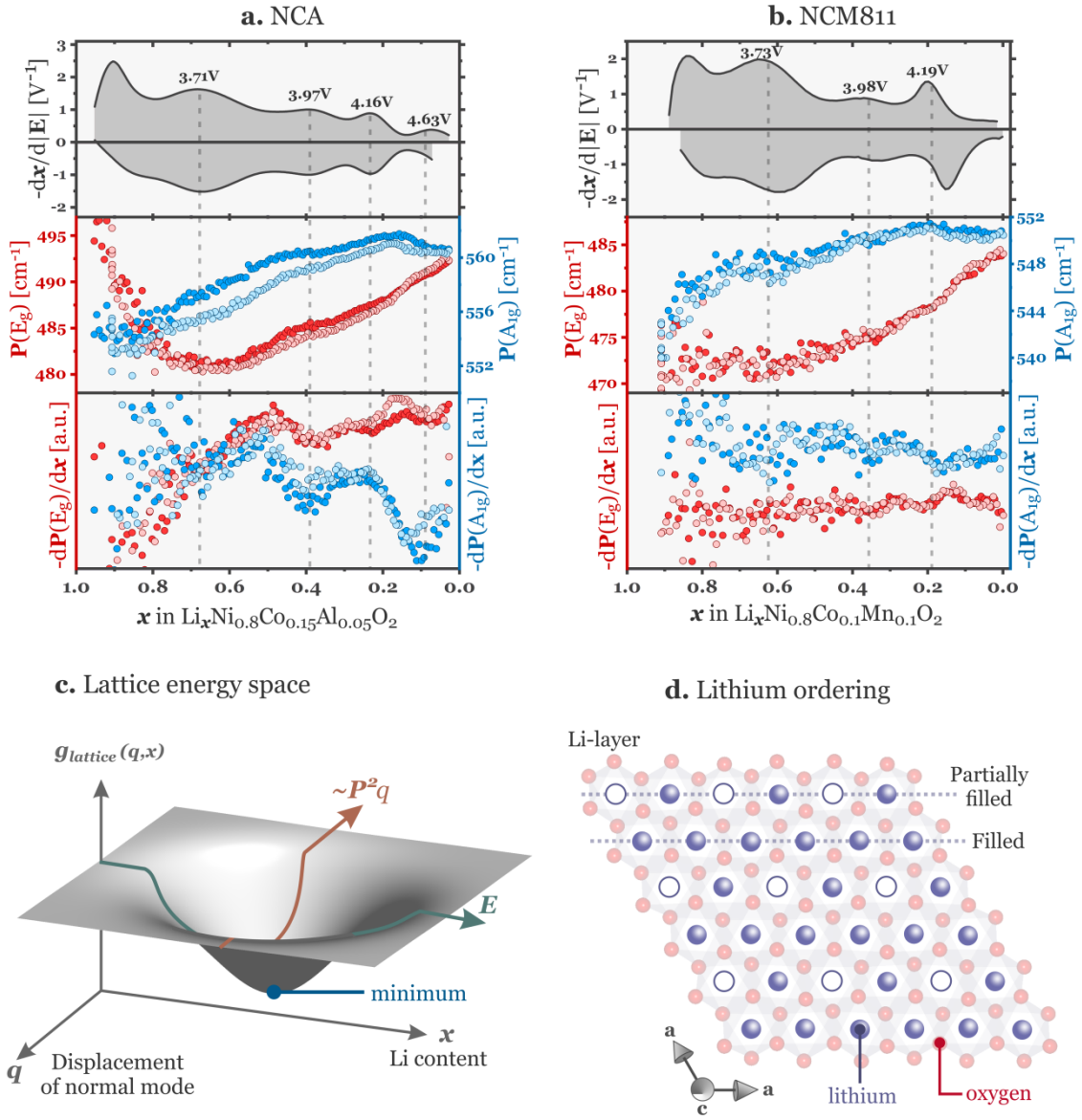

Figure 7.6. $-dx/d|E|$ curves along with the fitted band positions P and derivative curves $-dP/dx$ of the E_g and A_{1g} bands of **a.** NCA and **b.** NCM811 during the third overcharge cycle (3.0-4.8 V). The dotted lines reference the redox peaks labelled in the $-dx/d|E|$ curves. **c.** The lattice energy surface abstraction used for explaining the correlation between plateaus in P and E. The energy of the lattice can be thought as a surface that depends on the lithium content x and the atomic displacement q of a normal mode. The slope of the surface along the x direction is proportional to E, while the slope along q is related to P. A phase transition manifests as a minimum in the energy surface. **d.** Lithium layer of the $LiMO_2$ lattice viewed along the c-axis. Lithium ions in $Li_{0.75}NiO_2$ order into fully-filled rows alternated by half-filled rows.[249]

There is still the open question about the nature of these phase transitions, i.e. whether they are electronic, structural or configurational (section 2.3.2). Displacive phase transitions leading to lattice rearrangements are unlikely, since none of the Raman-active modes of NCA and NCM8111 decrease to zero frequency at the phase transition (see soft mode, section 3.2.4). However, there are two observations that hint at transitions of configurational nature. First, DFT calculations in the previous sections have shown that the NCA bands above 600 cm^{-1} arise from oxygen vibrations next to vacant Li^+ sites. Second, The intensity of these lithium vacancy bands (appendix B10) becomes detectable when the lithium content drops below 0.65, just after the redox peak at 3.71 V in Figure 7.6a. NCM811 also features the same redox peak after which the bands above 600 cm^{-1} show a growing intensity trend (appendix B10); therefore, these lithium vacancy bands are also present in NCM811 but overlap to Mn-related bands, causing less pronounced trends than in NCA. In light of these observations, the redox peak ~3.73 V in both oxides clearly originates from a configurational phase transition driven by the ordering of lithium and its vacancies within the Li-layer (Figure 7.6d), of similar nature as the transitions encountered in $LiNiO_2$ during cycling.[95,235,249] Unlike the case of $LiNiO_2$, X-ray diffraction does detect miscibility gaps neither in NCA nor in NCM811; hence, these ordered lithium domains remain short-ranged and thus they cannot be probed via diffraction techniques, but are readily detectable by Raman spectroscopy.

While it is tempting to assign the remaining redox peaks in Figure 7.6a-b to configurational phase transitions, electronic driving forces cannot be ruled out and might indeed be involved in the redox processes of Ni-rich oxides at low lithium contents, as it will be discussed later in this chapter.

7.5 Spectral trends during cycling: fitted peak intensities

This section describes the cycling-dependent trends on fitted peak intensities. Figure 7.7 shows the fitted peak intensities $I(E_g)$ and $I(A_{1g})$ of the two main Raman active bands of NCA (Figure 7.7a) and NCM811 (Figure 7.7b) during two standard cycles (3.0-4.3 V) and a third overcharge cycle (3.0-4.8 V). In general, the intensities of these bands increase during delithiation, until reaching maxima when the SOL approaches 0.2 Li^+ per formula. Most of these trends are reversible during re-lithiation, again with the exception of $I(A_{1g})$ of NCA after overcharge (Figure 7.7a, cycle 3). Another particularity is the step change of both $I(E_g)$ and $I(A_{1g})$ of NCA observed only during the first cycle (Figure 7.7a, cycle 1). Last, the trends of both NCM811 bands feature a peculiar hysteresis only at low SOL; however, such features could not be reproduced in repeated experiments. The interpretation of all these trends requires understanding the physical mechanisms modifying the Raman band intensities.

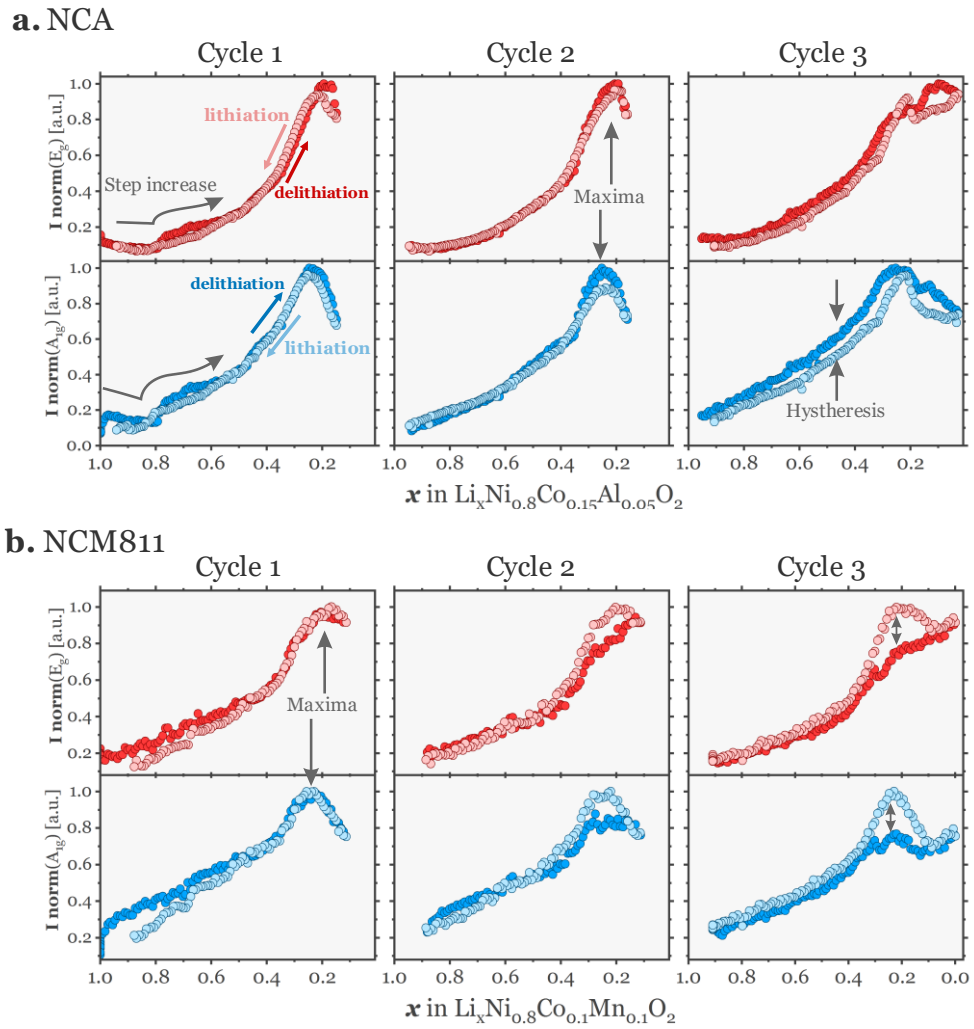

Figure 7.7. Fitted band intensities I of the E_g and A_{1g} Raman bands of **a.** NCA and **b.** NCM811 as a function of state of lithiation x, during two standard cycles and a third overcharge cycle. The intensities are normalized to the highest one measured during a cycle. The arrows highlight the key features of these trends that are discussed.

7.5.1 Understanding peak intensity changes

Cycling-dependent variations in the Raman band intensity of Ni-rich oxides have been previously described but not interpreted in sufficient depth.[160,173] As in the case of $LiCoO_2$ (section 6.3) such variations might originate from the intrinsic polarizability changes of the normal modes, or from attenuation/enhancement of the incident radiation intensity I_0 (see Equation 3.9). However, skin-depth effects are discarded since both the electronic conductivity[250,251] and the Raman band intensity of Ni-rich oxides increase on delithiation. Therefore, here four alternative (and possibly complementary) mechanisms are proposed by which the intensity of the Raman bands could be influenced by lithium content.

Mechanism 1: Evolution of the electron density around oxygen. Equation 3.9 shows that the Raman intensity increases with the square of the polarizability change induced by the vibration of the normal mode. Both the A_{1g} and E_g modes involve vibrations of oxygen atoms. It is therefore intuitive to consider that, if oxygens carry more electron density, their motion polarizes the lattice to a larger extent. Previously reported first-principles calculations have related higher oxygen electron density to more intense Raman bands.[252] Hence, the increasing $I(A_{1g})$ and $I(E_g)$ trends during delithiation would be a manifestation of electron density accumulating around oxygen. Likewise, the intensity inflection for $x < 0.2$ would accordingly reflect electron depletion from the oxygen atoms.

Mechanism 2: Electronic resonance Raman effect. The Raman bands of NCA and NCM811 are both enhanced by electronic resonance (section 5.6). If the electronic structure of the oxides (see Figure 5.7b) evolves significantly during cycling, $I(E_g)$ and $I(A_{1g})$ would thus probe the *x*-dependent changes of the absorption bands of the oxides relative to the laser excitation energy (here 632 nm ∼1.96 eV).

Mechanism 3: Site disorder induced by Jahn−Teller (JT) distortions. In Ni-rich oxides nickel adopts a low-spin $Ni^{3+}(t_{2g})^6(e_g)^1$ configuration, which is JT-active (section 2.1.1).[45,86] The resulting distortion of the $Ni^{3+}O_6$ octahedron and its propagation to neighbouring sites would result in broader and weaker Raman bands. Once delithiation proceeds, nickel oxidizes to a JT-inactive low-spin Ni^{4+} $(t_{2g})^6(e_g)^0$ configuration.[190,195,253] As the distortion disappears, the remaining $Ni^{4+}O_6$ environments are more symmetric and, thus, are anticipated to yield sharper and stronger bands. Therefore, the observed growth of Raman intensities on delithiation would reflect the rise of the Ni^{4+}/Ni^{3+} proportion, so the inflection would reflect a subsequent distortion of the $Ni^{4+}O_6$ environments.

Mechanism 4: Lattice strain. The Raman band intensities of $LiCoO_2$ powder have been observed to increase with applied external pressure, likely due to an increased electron density around oxygen atoms as a consequence of compression.[179] Variations in band intensity may be indirectly caused by the build-up of lattice strains upon delithiation, so the inflection would be a manifestation of strain relief by, for instance, particle cracking (section 2.4.3).

These proposed mechanisms are not mutually exclusive. For instance, a particular electronic structure could at the same time modify the polarizability, favour JT distortion, permit electronic excitations, and change the electronic conductivity of the oxide. However, the results of DFT calculations presented in Figure 7.4 predict an increase of non-resonant Raman activity of the E_g and A_{1g} modes on delithiation, in an unstrained LCO lattice with no JT-distortion. Consequently, changes in the electron density around oxygen atoms (mechanism 1) are most likely to be the main contributor to band-intensity growth upon

delithiation. Therefore, in the following sections, mechanism 1 is applied to the interpretation of the trends in peak intensities shown in Figure 7.7.

7.5.2 Maxima in intensity trends at low SOL

On charge, the E_g and A_{1g} bands display a progressive intensity increase until reaching the maxima at $x \sim 0.2$, hereafter the intensities again decrease. According the mechanism 1, the intensity weakening of the bands originates from the depletion of oxygen charge. As mentioned in section 2.1 the (de)lithiation of $LiMO_2$ is conventionally charge-compensated by the oxidation/reduction of the transition metals. However, at low states of lithiation Ni-rich oxides are prone to the oxidation of the oxygen anions instead, which result in the reconstruction of the oxide surface and the release of oxygen gas (section 2.4.1). In this sense, the intensity inflections in Figure 7.7 might be the manifestation of an electronic transition involving the oxidation of oxygen. This scenario is further investigated by comparing the band intensity trends to the potential release of oxygen gas as monitored by online electrochemical mass spectrometry (OEMS) (details in appendix B11).

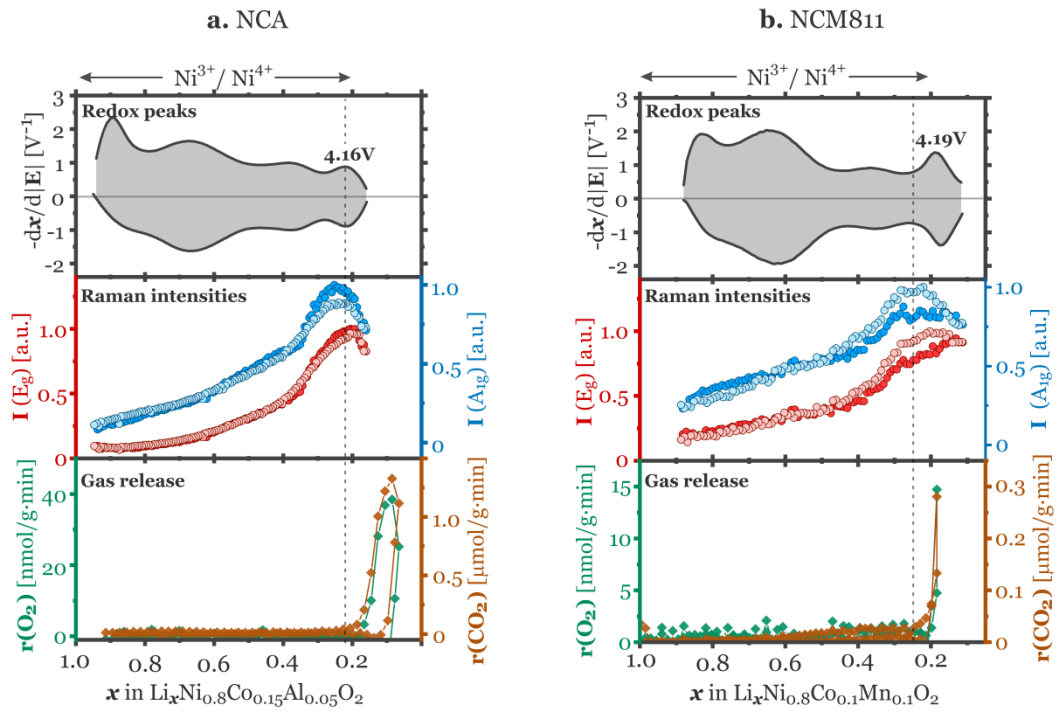

Figure 7.8. −dx/d|E|curves along with the fitted $I(E_g)$ and $I(A_{1g})$ band intensities and the CO_2 and O_2 evolution analysis of **a.** NCA and **b.** NCM811. Within the $1.0 < x < 0.2$ range both oxides are formally expected to charge-compensate the cycling process with the Ni^{3+}/Ni^{4+} redox couple. The dotted line highlights the onset of CO_2 and O_2 evolution, which occurs shortly after the Raman intensities have reached maxima.

Figure 7.8a-b show that within most parts of the 1.0 > *x* > 0.2 range, the Raman intensities of the oxides keep their increasing trend and there is no detectable evolution of oxygen gas, as expected given that both oxides are composed of 80 % nickel, which is the transition metal responsible of charge compensation;[30,31,195,254] in other words, extraction of 80 % lithium (*x*=0.2) is formally expected to be accompanied by the oxidation of all Ni^{3+} to Ni^{4+}. However, when the SOL approaches *x* = 0.2 the Raman intensities reach maxima, shortly followed by the release of oxygen gas. CO_2 gas is also released, likely from the decomposition of the electrolyte triggered by the formation of highly reactive oxygen species at the surface of the active material (see Figure 2.4).[255] These findings support the hypothesis that the Raman intensity maxima respond to a fundamental electronic transition of Ni-rich oxides at $x \sim 0.2$, where electrochemical delithiation changes from predominantly cationic ($Ni^{3+} \rightarrow Ni^{4+}$) to an anionic ($O_2^- \rightarrow O^-/O$) charge-compensation process. The low-SOL hysteresis on $I(E_g)$ and $I(A_{1g})$ of NCM811 (Figure 7.8b) tentatively suggests that the electronic transition is somewhat different in the two oxides; however, such features could not be reproduced in repeated other experiments and so they are not further discussed.

Based on the quantitative analysis of the gas evolution, oxygen oxidation can induce the reconstruction of only a few surface oxide monolayers of ~ 1 nm depth,[255] which is too thin for detectable Raman signals to arise. Considering a laser penetration depth of several hundreds of nanometres (section 6.3), the Raman intensity response in Figure 7.7 rather originates from the material's bulk. Therefore, these findings indicate that partial oxygen oxidation does occur also in the bulk of both Ni-rich oxides, whereas full oxygen oxidation and release is only possible at the surface, probably due to unlinked orbitals and lack of kinetic constraints (i.e. here O_2 can form and escape). Recent X-ray absorption spectroscopy studies of Ni-rich layered oxides[256–258] complementarily confirmed the oxidation of oxygen anions from the bulk at low SOL.

It is also important to note that, while the inflection of Raman intensities and gas evolution are correlated, these two processes occur at lower electrode potential than the redox peak of NCM811 at 4.19 V (Figure 7.8b). The oxidation of oxygen might not be the phase transition causing the redox peak at 4.16-4.19 V common of Ni-rich oxides. The appearance of the redox peak rather correlates to the abrupt *c*-axis contraction of Ni-rich lattice that precedes mechanical degradation, indicating that the associated phase transition is structural and detrimental for electrochemical performance.[47,48,259,260] Kondrakov et al. showed that such contraction likely results from the weakening of interlayer O-O repulsions, which occurs when charge is depleted from oxygen orbitals hybridized to Ni-e_g^* orbitals.[254] Interestingly, electron removal from e_g electronic orbitals also explains why in Figure 7.5 $P(A_{1g})$ reaches maxima while $P(E_g)$ does not: section 5.6.3 showed the A_{1g} vibrational mode to be more sensitive to the electron population of M-*d* orbitals thanks to the Raman-resonance effect.

In brief, very positive electrode potentials cause electron depletion from oxygen levels hybridized with Ni-e_g levels. Oxygen oxidation in the bulk initially manifests as maxima in $P(A_{1g})$, $I(E_g)$ and $I(A_{1g})$ trends (Figure 7.5 and Figure 7.7), shortly followed by the release of oxygen gas from the surface (Figure 7.8). Oxygen oxidation in the bulk leaves the lattice prone to eventually undergo an abrupt structural contraction along the *c*-axis that manifests in the redox peak at 4.16-4.19 V. If severe, the contraction irreversibly degrades the lattice along the *c*-axis, as indicated by the hysteresis of both $P(A_{1g})$ and $I(A_{1g})$ after overcharge (Figure 7.5a and Figure 7.7a). This sequence of events implies that oxygen oxidation also initiates mechanical degradation (section 2.4.1), and the results presented in Figure 7.8 indicate that the onset of this detrimental phenomenon can be readily detected by analysing the Raman spectral trends.

7.5.3 Step change of NCA intensities during the first delithiation

A particular feature of the intensity trends of NCA spectra (Figure 7.7a) is a step-wise simultaneous change of intensity of both Raman bands that only occurs during the first cycle. During delithiation, $I(E_g)$ and $I(A_{1g})$ both exhibit a step increase at 3.74 V (x = 0.8), while during re-lithiation both intensities feature a step decrease at 3.58 V. Since these step-changes only occur in the first cycle, they might be related to the dissolution/formation of the $-CO_3$ surface layer that irreversibly consumes Li^+, as discussed above (Figure 7.1).[234,257,259] These layers dissolve and might even reform during re-lithiation, as previously evidenced by X-Ray diffraction.[259]

In Figure 7.9a the step-increase on the intensity trends of NCA during delithiation (stored on inert Ar atmosphere) is presented in detail and compared to the trends of long-term air-exposed NCA particles (Figure 7.9b), where thicker $-CO_3$ layers are expected.[234] The step increase occurs at different lithium contents (x=0.79 in Ar-stored NCA and x=0.96 in Air-stored NCA) but at very similar electrode potentials (3.75 V in Ar-stored NCA, 3.78 V in Air-stored NCA). The evidence indicate that the step-wise changes are likely triggered by an electrochemical process extrinsic to the cathode material, since they do not depend on the $LiMO_2$ lithium content but rather on the electrode potential. The $-CO_3$ surface-layer breakdown is indeed a cathode-independent process reported to occur above 3.8 V, according to X-ray absorption spectroscopy.[257] However, Raman signatures of these carbonates (expected around 1080 cm^{-1}) are not directly detected, probably due to the nm-thickness they typically feature at the surface of the particles.[261] Nevertheless, Li^+ blockage by $-CO_3$ layers and the sudden Li^+ release after layer dissolution (Figure 7.9c),[234] could influence the Raman peak intensities in the step-wise manner illustrated in Figure 7.9a-b.

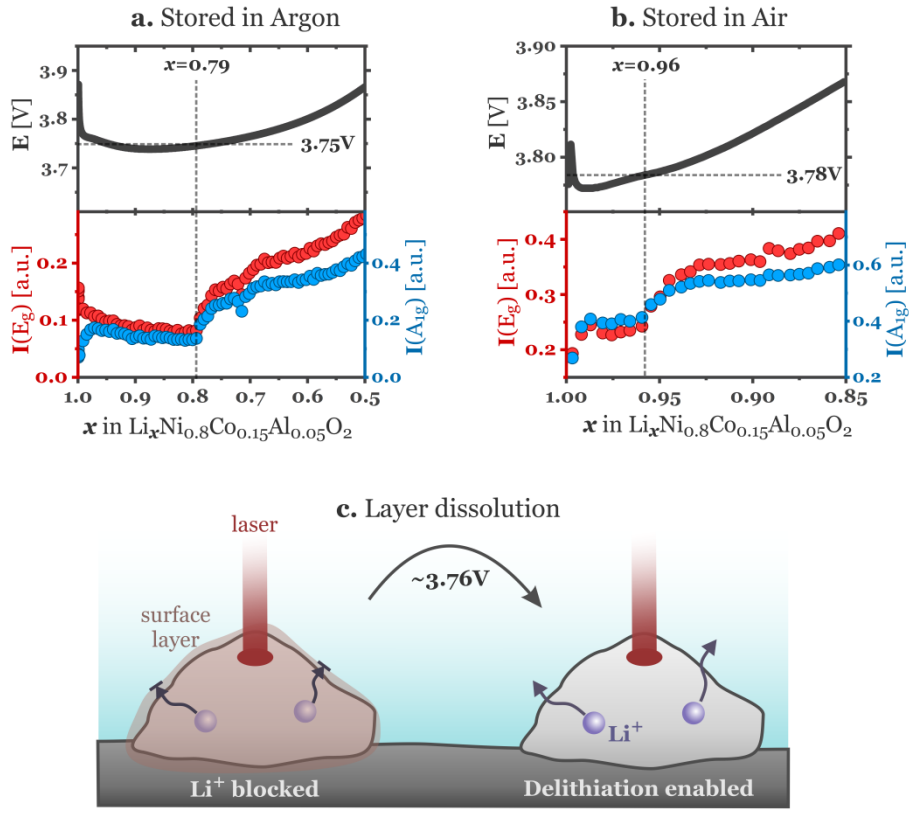

Figure 7.9. Galvanostatic potential profiles and the corresponding Raman intensity profiles of composite electrodes prepared using active material **a.** stored on an Argon-filled glovebox and **b.** stored on air for 8 years. **c.** Proposed mechanism for the step increase of intensities during delithiation: Li^+ blockage due to the surface layer impedes delithiation, such that Raman intensity variations are not detected. Once the layer dissolves, delithiation of the probed particle is enabled and results in a detectable increase of Raman intensities.

7.6 Summary

In this chapter the occurrence and nature of cycling-dependent phase transitions of NCA and NCM811 are investigated using *operando* Raman spectroscopy. Both oxides exhibit several comparable redox couples, indicating that they cycle through multiple phase transitions, intrinsic to Ni-rich materials. All Raman-active bands have been assigned based on experimental investigations and DFT calculations: both oxides exhibit a E_g band (480-500 cm^{-1}), a A_{1g} band (550-565 cm^{-1}), and a third set of bands above 600 cm^{-1} that in NCA are assigned to oxygen displacements towards vacant lithium sites, whereas in NCM811 they overlap to bands intrinsic to Mn-containing oxides. The automated fitting procedure enables detailed monitoring of the SOL-dependent trends in peak position *P* and intensities *I* within narrow composition intervals. In general, the SOL-dependent evolution of *P* is decoupled from the crystallographic lattice changes. The fine structure of *P* trends exhibit subtle plateaus that correlate to the redox couples of both oxides; such correlation is best explained using an abstract lattice energy space. Based on the assignment and

SOL-dependent intensity of the bands above 600 cm^{-1}, the redox couple centred at ~3.73 V has been found to originate from a configurational phase transition between lithium ordered/disordered phases, similar to the case of $Li_{0.75}NiO_2$. *I(E_g)* and *I(A_{1g})* of both oxides reach maxima close to *x*=0.2, shortly followed by the release of lattice oxygen from the surface of the material. Further delithiation leads to the abrupt lattice contraction along the *c*-axis that manifest as the redox couple signature at 4.16-4.19 V in the voltage profile. Severe contraction from overcharge degrades the structural integrity of the lattice irreversibly and anisotropically, confirmed by the hysteresis in *P(A_{1g})* and *I(A_{1g})*. The *P(A_{1g})* hysteresis is comparatively smaller in NCM811 than in NCA, indicating the Mn-containing oxide to be more resilient to degradation. A step increase of *I(E_g)* and I(A_{1g}) in NCA during the first delithiation suggest the electrochemically-triggered dissolution of a $–CO_3$ layer ca. 3.76 V.

Chapter 8 *Operando* Raman spectroscopy of NCMs

Composite cathodes based on $LiNi_{0.33}Co_{0.33}Mn_{0.33}O_2$ (NCM111) and $LiNi_{0.6}Co_{0.2}Mn_{0.2}O_2$ (NCM622) oxides provide a good compromise between energy density and cycling stability, therefore Li-ion batteries based on these active materials are attractive alternatives to Ni-rich based cathodes for automotive applications. In this chapter it is discussed the investigation of the cycling-dependent Raman spectra of NCM111 and NCM622, using both conventional (i.e. peak fitting) and non-conventional (e.g. multivariate curve resolution and generalized correlation) data analysis techniques, capable of retrieving robust and meaningful spectral trends. The conclusions drawn from the trends are based on the knowledge build on previous chapters, and compared to the cycling characteristics of Ni-rich oxides. The findings are expected to provide a more complete overview on how structural and electronic transitions are driven by cycling, and also on how these transitions depend on the transition metal ratio in the oxide. Reproduced in part with permission of Chemistry of Materials, submitted for publication (2019).

8.1 Electrochemistry

Figure 8.1 shows the constant current and differential charge curves of NCM111 and NCM622 based composite electrodes during the second cycle. All the main electrochemical features are in general agreement with previous reports.[46–48] During the activation process on the precycle, both electrodes lose reversible specific charge. NCM622 with 0.6 nickel per formula unit delivers higher specific charge than NCM111 (0.33 nickel per formula unit) within the 3.0-4.3 V window, as expected given that Ni is the main contributor to charge compensation.[195,262,263] In addition, NCM111 cycles with higher overpotentials than NCM622, as indicated by its comparatively larger delithiation-lithiation hysteresis. During the overcharge cycle (Appendix B.12) the hysteresis for NCM622 increases mildly, while for NCM111 widens severely, indicating that the latter degrades more than the former due to deep delithiation.

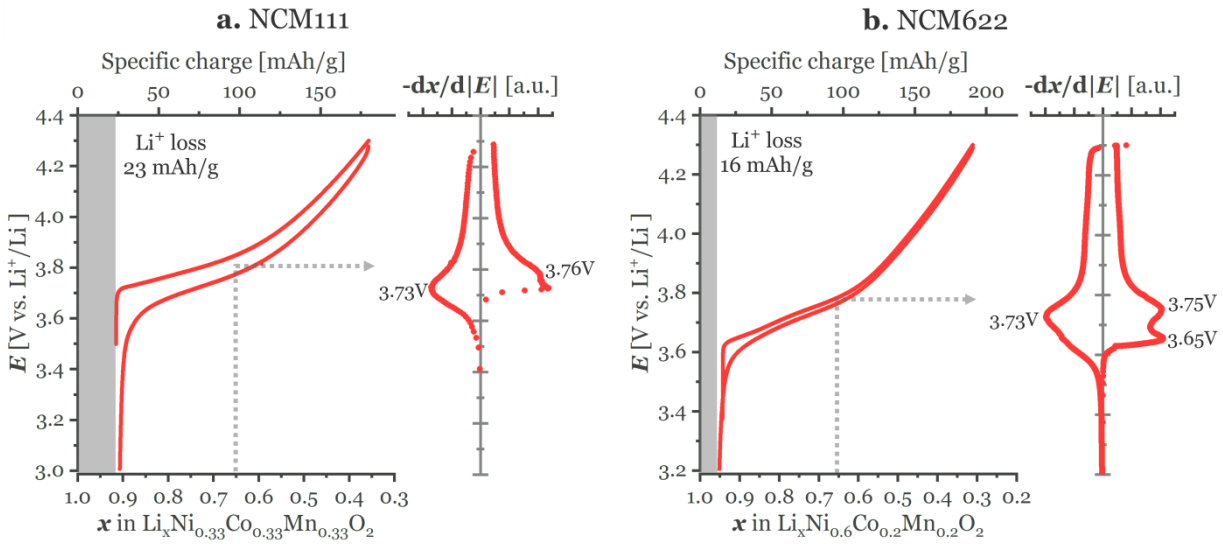

Figure 8.1. Galvanostatic potential profiles and the corresponding –dx/|dE| curves of **a.** NCM111 and **b.** NCM622 during the second cycle (3.0–4.3 V *vs.* Li^+/Li). The dotted-line arrow indicate that the redox peak at ~ 3.74 V occurs at $x \sim 0.65$.

Delithiation of NCM111 proceeds through one main redox peak only, located at 3.76 V, while in NCM622 it splits into a pair of peaks located at 3.65 V and 3.75 V; these peaks manifest themselves as only one peak at 3.73 V during re-lithiation. *In situ* X-ray diffraction does not identify any miscibility gap while these materials cycle. Note, however, that the peak pair at ~3.74 V ($x \sim 0.65$, Figure 8.1) also occurs in Ni-rich oxides, where it has been assigned to a lithium-ordering phase transition (section 7.4.2). Unlike Ni-rich oxides, neither NCM111 nor NCM622 exhibit redox couples at more positive potentials (i.e. $E > 3.8$ V). These differences justify reasonable doubt as to whether the assignments and interpretations made on Ni-rich oxides can also be applied on NCM111 and NCM622. Hence, the following sections present the Raman spectral features of these oxides during cycling, searching for features related to miscibility gaps and electronic transitions that might not be manifested in the electrochemical profiles, but still could have relation to the phenomena observed in Ni-rich oxides.

8.2 General features of the *operando* Raman spectra

Figure 8.2a shows several sample spectra of NCM111 at various stages of the first delithiation. The spectrum at open circuit potential (OCP) is dominated by a strong band at 609 cm^{-1}, typical for Mn-containing oxides, with a shoulder at higher wavenumber assigned to inter/intralayer disorder. The spectrum also features some weak and broad bands at 485 and 400 cm^{-1} that envelop multiple Raman-active vibrations (section 5.5.1). During

delithiation all these bands weaken progressively until the SOL approaches *x*=0.5, at which point the spectral profiles grow a pair of bands at 481 and 555 cm^{-1}.

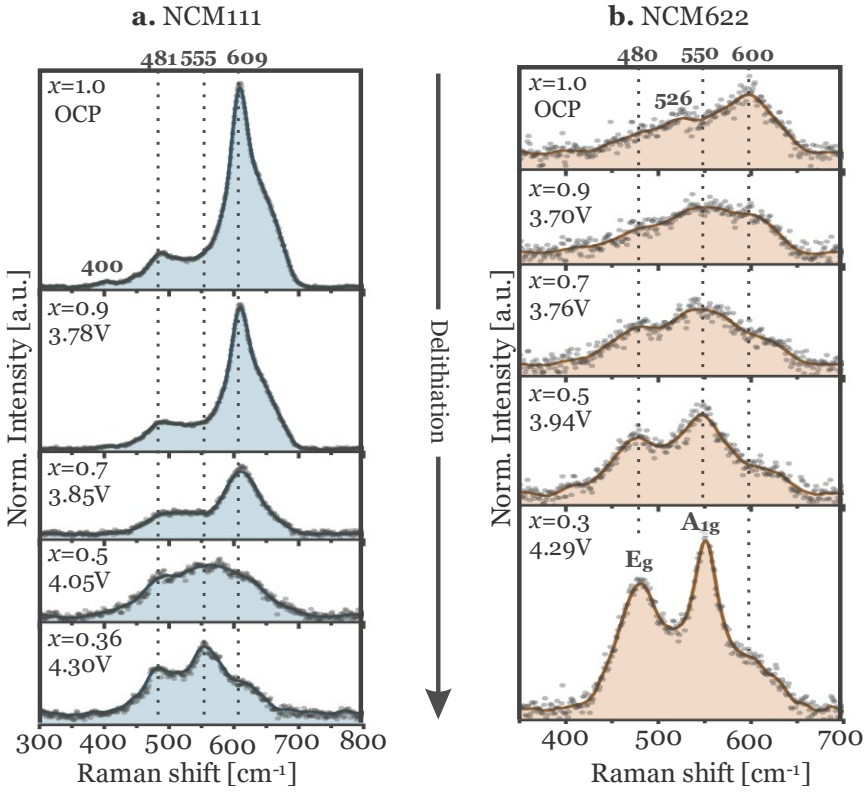

Figure 8.2. Raman spectra of **a.** NCM111 and **b.** NCM622 at various SOL (x in $Li_xNi_aCo_bMn_cO_2$) during the second cycle (3.0–4.3 V).

Figure 8.2b shows the sample spectra of NCM622 at several SOL during the first delithiation. At OCP, the spectrum displays the band at 600 cm^{-1}, common of Mn-rich oxides, in addition to a pair of weak bands at 480 cm^{-1} and 550 cm^{-1} that are strengthened progressively during delithiation.

In general, the spectra of both oxides develop two well-defined bands at ~480 and ~550 cm^{-1} at the end of delithiation, which show remarkable resemblance to the bands observed in delithiated Ni-rich oxides (see Figure 7.3). Hence, these bands are provisionally labeled as the E_g and A_{1g} modes of vibration of the $R\bar{3}m$ lattice. The oxygen environment of lithiated Ni-containing oxides is diverse, but seems to rearrange into the C_{3v} environment of the rhombohedral lattice (section 5.1) once a sufficient amount of lithium has been electrochemically extracted. The complete SOL-dependent evolution of these bands will be shown in detail in the following sections.

8.3 Cycling-dependent evolution of NCM111 spectra

Figure 8.3 shows the Raman spectra of NCM111 during the first cycle, along with the constant-current potential profile and the calculated lithium content *x* in the oxide. In general, the spectral profiles and trends of NCM111 are consistent with *ex situ*[264] and *in situ*[161] measurements reported previously. The time-dependent evolution of the spectra during delithiation can be divided into two main stages: i) an initial stage characterized by the weakening of the band centered at 609 cm^{-1} and ii) a later stage displaying the appearance and growth of a band triplet at 480, 555 and 575 cm^{-1}. Note that the band at 575 cm^{-1} is not apparent in the sample spectra of Figure 8.2a, but it can be discerned as an independent band when its cycling-dependent evolution is followed in the surface map representation in Figure 8.3a. During re-lithiation the spectra return back to their initial shape, following reversibly the two-stage spectral evolution. There are no obvious turning points between the two stages as the changes are continuous, but they extend throughout the SOL being characteristic to nickel's two-step charge-compensation process.

In fully lithiated NCM111 all manganese atoms are found in a tetravalent state and all nickel atoms in a divalent state (section 5.5.2). Delithiation of NCM111 is firstly charge-compensated via the $0.33Ni^{2+}$->$0.33Ni^{3+}$ oxidation, which assists the departure of 0.33Li (1.0>x>0.66). Subsequent delithiation (0.66>x>0.33) involves a $0.33Ni^{3+}$-> $0.33Ni^{4+}$ oxidation.[195] The two-staged evolution of the Raman spectra shows a clear correlation to the two-staged charge-compensation process, when observed in the surface map Figure 8.3, along the two-step oxidation lines at *x*=0.66. The spectral profiles of NCM111 seem solely influenced by the oxidation state of nickel. Ni^{2+} is characterized by a strong Raman band at 609 cm^{-1}, while Ni^{3+} promotes a general weakening of all bands, and finally Ni^{4+} is characterized by the band triplet at 480, 555, and 575 cm^{-1} and a residual broad band above 600 cm^{-1}.

More details about the spectral evolution can be revealed if each spectrum is fitted and the fitting parameters are studied versus SOL. However, given the highly overlapping nature of the bands, there are multiple fitting solutions for each spectrum; hence, an automated fitting procedure would unavoidably involve arbitrary parameters not representative of the physical system. Instead of attempting deconvolution into Lorentz-type profiles, a multivariate curve resolution (MCR-ALS) analysis is applied to the *operando* spectra,[163] which decomposes the time-dependent spectra into a linear combination of components, each weighted according to their relative proportion at each SOL (section 4.5.2). Figure 8.3b shows that the two first components — explaining most of the intensity variance — compare well to the experimental Raman spectrum of NCM111 in the lithiated

(component 1) and delithiated (component 2) states. In other words, the evolution of the spectra in Figure 8.3a can be confidently represented as the SOL-dependent proportions of lithiated and delithiated spectral contributions.

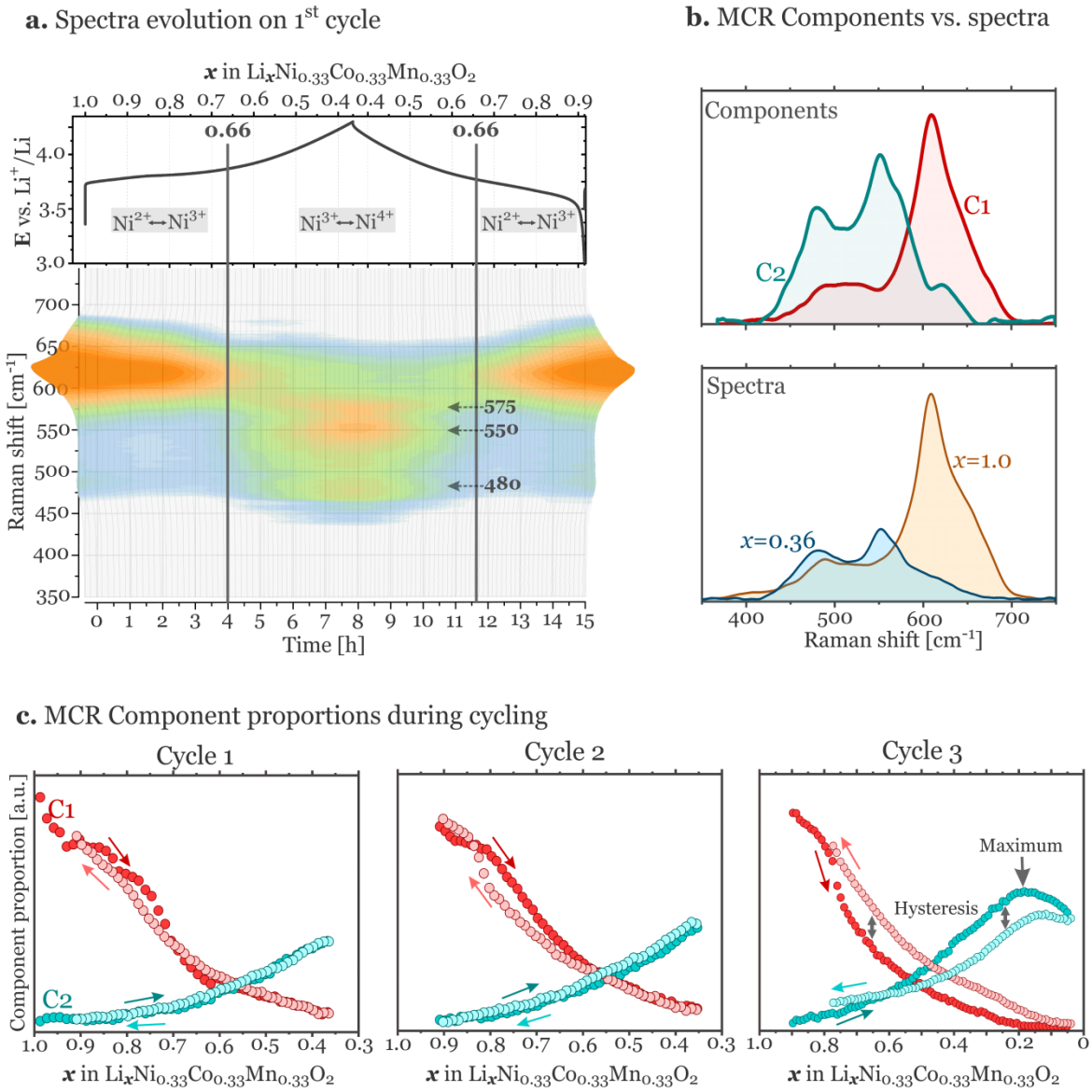

Figure 8.3. **a.** Constant-current profile and colored surface map of the spectral evolution of NCM111 during the first cycle (3.0-4.3 V); the vertical lines highlight the SOL where the nickel redox couples are formally expected to change. **b.** Comparison between the two resulting MCR components and the spectra of lithiated (x=1.0) and delithiated (x=0.36) NCM111. **c.** SOL-dependent evolution of the proportion of both MCR components (component 1 in red, component 2 in blue-green) during two standard cycles (3.0-4.3 V) and a third overcharge cycle (3.0-4.8 V). The colored arrows indicate the directions of delithiation (darker color) and lithiation (lighter color), while the grey arrows highlight particular features of the trends.

Figure 8.3c shows the SOL-dependent trends of the proportions of component 1 (red) and component 2 (blue-green) during two standard cycles as well as during the third overcharge cycle. In general, component 1 fades at the expense of the growth of component 2, a behavior consistent with the previously described interplay between delithiated and lithiated spectral profiles in Figure 8.3a. In the first and second cycles the weakening of component 1 and growth of component 2 are both monotonic and the trends exhibit negligible hysteresis, demonstrating thus high reversibility. During the third cycle, however, the trends of components 1 and 2 exhibit a delithiation/relithation hysteresis, indicating that overcharge has introduced an irreversibility, also reflected on the cycling process (Appendix B12).

In addition, the trends of component 2 undergo a maximum close to x=0.2, analogous to the observed trends in the peak intensity of Ni-rich oxides (section 7.5.2). There are three main reasons justifying a relationship between the proportion trends of component 2 and the variations in electron density around oxygen atoms. First, all Raman-active vibrations predominantly involve the displacement of oxygen atoms (section 5.5.1). Second, component 2 reflects the intensity contributions of both the E_g and A_{1g} bands of delithiated NCM111 (Figure 8.3b). Third, these bands in Ni-rich oxides undergo a similar intensity inflection reflecting electronic structure changes of oxygen atoms (section 7.5.2). While NCM111 does exhibit neither redox couples (Figure 8.1a), nor abrupt lattice contractions at these SOL,[47] the oxide reportedly releases oxygen gas close to x=0.3.[255,265] Therefore, the maximum in the trend of component 2 seems to be related to the transition towards an anionic charge-compensation process at low SOL. Note that during delithiation, oxygen evolution is reported to occur at x=0.3, before the trend of component 2 reaches maximum at x=0.2. The SOL difference between these two events (Δx=0.1) roughly agrees with the rather high amount of Li^+ irreversibly "lost" during the previous two cycles (delithiation starts at x=0.9 in the third cycle, Figure 8.3c). Hence, when the amperometric lithium count used to calculate the SOL (section 4.3.2) is corrected by the Li^+ "loss", both events appear to occur almost simultaneously, confirming that they are indeed related.

Despite having different nickel proportions, the spectral evolution of NCM111 during cycling keeps some parallels to the one of Ni-rich oxides, namely the observed overcharge hysteresis and the inflection of intensities at low SOL. In the next section it is discussed the investigation into the *operando* Raman spectra of NCM622 — with a nickel proportion intermediate to NCM111 and Ni-rich oxides — searching for features dependent not only on the SOL, but also on the nickel content in the oxide.

8.4 Cycling-dependent evolution of NCM622 spectra

Figure 8.4 shows the evolution of Raman spectra of NCM622 along with the corresponding constant-current profile. The spectral profile in the lithiated state, characterized by the band at 600 cm^{-1}, starts fading as soon as delithiation initiates (time=0 h) and disappears soon after x=0.7. The broad band centered at 550 cm^{-1} gains intensity close to x=0.9 and remains of similar height until x=0.55, when it together with the band at 480 cm^{-1} intensify rapidly. In addition, some weaker features at 595 cm^{-1} can be resolved appearing when x<0.45. During re-lithiation the spectrum returns reversibly back into its initial profile. There are no such Raman experiments in the literature to be compared with,[67] but the trends in Figure 8.4a are consistently reproducible in repeated experiments.

This time, the bands are sufficiently defined and separated to confidently perform an automated fitting procedure on all spectra, based on a Lorentz-type three-peaks model with the constraints shown in Figure 8.4b. The peaks are provisionally labelled as *v1, v2* and *v3* as their assignment is not yet certain. The fitted peak positions (Appendix B13) feature some trends during cycling but the scattered nature of them complicates the analysis. The peak intensities as shown in Figure 8.4c are significantly less scattered and can be analyzed in detail. The peak intensity trends show negligible delithiation-lithiation hysteresis, indicating high reversibility during all three cycles. Despite experiencing a moderate *c*-axis contraction on overcharge,[47] the intensity trends of NCM622 do not exhibit signs of irreversibility after severe Li^+ depletion. Both the electrochemical profiles and the intensity trends indicate that NCM622 is less affected by overcharge as compared to NCM111.

The peaks labelled *v1* and *v2* evolve similarly: a slow, linear intensity increase that accelerates when x<0.55. This behavior repeats on cycle 2. During the third (overcharge) cycle the intensities of both peaks saturate: peak I at x=0.3 and peak II slightly earlier (x=0.35). The *I(v1)* and *I(v2)* trends might be also related to the charge-compensation process of NCM622. Due to manganese-to-nickel electron transfer (section 2.1.1), fully lithiated NCM622 formally contains $0.2Ni^{2+}$ and $0.4Ni^{3+}$ per formula unit. Therefore, in analogy to the case of NCM111, delithiation down to x=0.8 is formally expected to be charge-compensated by a $Ni^{2+}\rightarrow Ni^{3+}$ redox couple, whereas delitiation within $0.8 > x > 0.4$ is charge-compensated by a $Ni^{3+}\rightarrow Ni^{4+}$ couple. When all nickel has been oxidized, oxygen anions might participate in charge compensation. In this sense, the saturation of the trends in *I(v1)* and *I(v2)* seems to be a spectral signature of such anionic-redox process, since it occurs at a SOL (x ~ 0.35), when nickel is expected to be fully oxidized. Also at x~0.35, cells with a NCM622-based cathode are reported to evolve CO_2 gas resulting from electrolyte reactions with oxidized oxygen species at the particle's surface[255], indicating again that the intensity trends inflect when oxygen oxidation becomes the charge-compensation process.

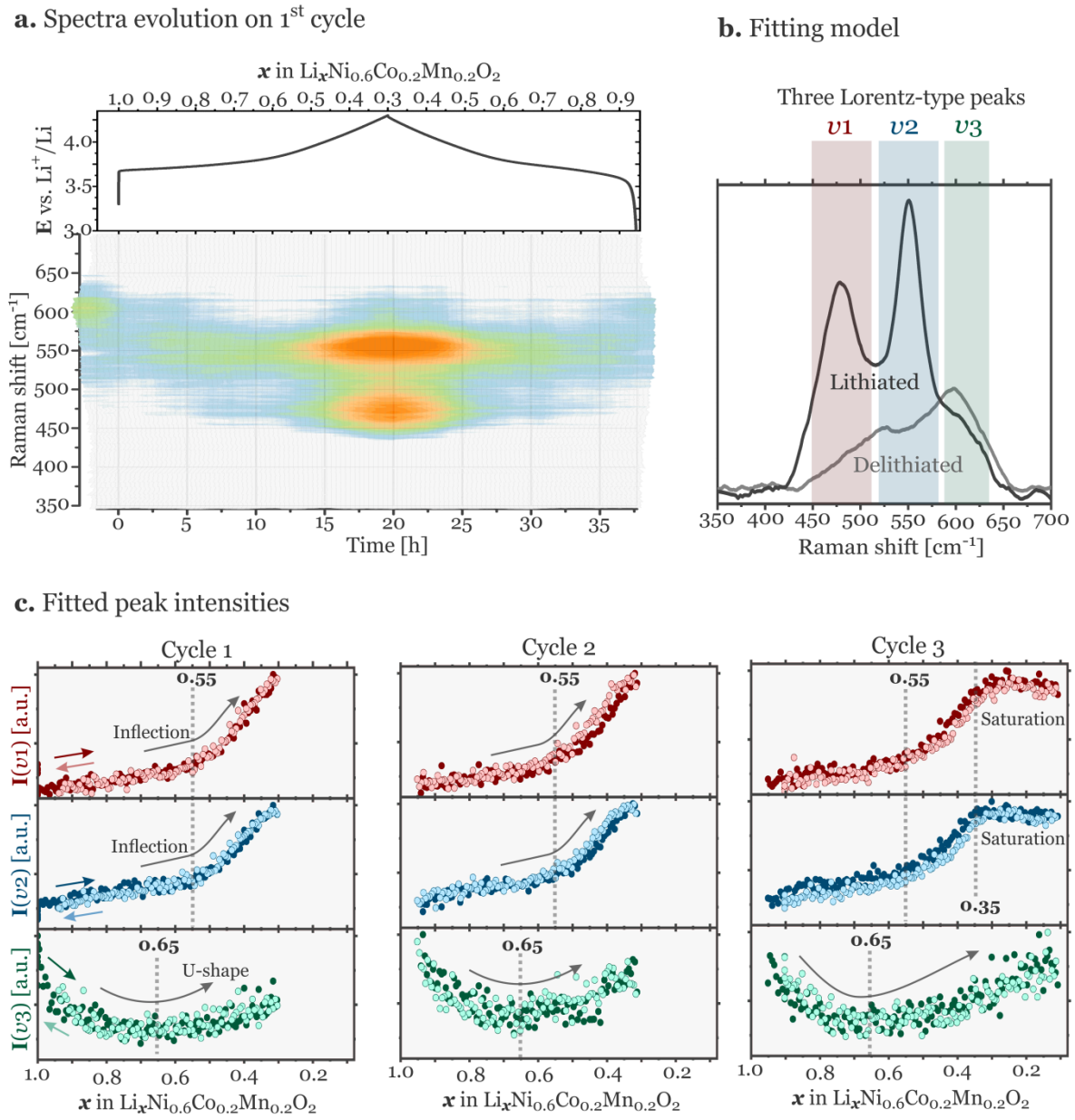

Figure 8.4. **a.** Constant-current profile and colored surface map of the spectral evolution of NCM622 during the first cycle (3.0-4.3 V). **b.** Three-peak model used for automated fitting of the spectra. The three main peaks observed to evolve in NCM622 are labelled *v1*, *v2* and *v3*, which are fitted using Lorentz-type functions constrained to the spectral regions showed in the shadowed rectangles. **c.** Fitted band intensities *I* of *v1* (red), *v2* (blue) and *v3* (green) as a function of SOL, during two standard cycles (3.0-4.3 V) and a third overcharge (3.0-4.8 V) cycle. The intensities are normalized to the highest intensity measured during a cycle. The colored arrows indicate the directions of delithiation (darker color) and lithiation (lighter color), while the grey arrows highlight particular features of the trends.

While the band intensities are clearly sensitive to electronic effects, it is still not fully clear what causes the early inflections of their trends, observed close to 0.55 in Figure 8.4c. It is therefore speculated that NCM622 undergoes some kind of electronic rearrangement close to *x*=0.55, which transfers electron density to oxygen atoms and increases the Raman intensities of *v1* and *v2*.

The band close to 600 cm^{-1} labelled as *v3* exhibits a U-shape trend that reaches minimum between *x*=0.8 and *x*=0.65. The increasing trend of *v3,* that occurs when x<0.65, coincides with the redox peak at 3.73 V, just as in the case of Ni-rich oxides (section 7.4.2). Therefore, the U-shaped trend of *v3* indicates that this spectral region hosts i) Mn-related bands that fade during delithiation within the 1.0 > *x* > 0.8 interval, just as in NCM111 (Figure 8.3a), and ii) lithium vacancy bands just as in Ni-rich oxides, which appear and grow in intensity when delithiation proceeds below *x*=0.65. Supporting this interpretation requires visualizing the contrasting behavior that the bands above 600 cm^{-1} exhibit during cycling of both types of NCM materials. However, the cycling dependent spectral trends of NCM111 have been obtained by the MCR method, which is not directly comparable to the fitted peak trends acquired for NCM622.

An alternative way of comparing the spectral trends is by investigating the correlated changes that the Raman bands undergo during cycling. For this reason, the generalized correlation analysis (section 4.5.3) is applied to the *operando* spectra of NCM111 and NCM622 and also NCA as a Mn-free oxide reference; the resulting synchronous maps are shown in Figure 8.5. Pairs of bands that grow or disappear collectively result in positive correlation zones and likely share physical origin; in contrast, when a band grows at the expense of another band, the pair appears negatively correlated and thus they likely originate from competing processes (Figure 8.5d).

The synchronous map of NCM111 features three cross-correlation zones: two negatively-correlated centered at (609,550) cm^{-1} and (609,475) cm^{-1}, and one positively correlated zone at (550,475) cm^{-1}; i.e., the 475,550 cm^{-1} pair of bands grow at the expense of the band at 609 cm^{-1}, as observed in trends in Figure 8.3. The Mn-free oxide NCA also exhibits three cross-correlation zones but all positively correlated, generated by peaks at 478, 550 and 605 cm^{-1}. Hence, the band ca. 600 cm^{-1} correlates to the (550,475) cm^{-1} pair negatively in NCM111 but positively in NCA, highlighting that Mn-related bands and lithium vacancy bands are decoupled from each other. However, NCM622 despite being a Mn-containing oxide, exhibits a band at 605 cm^{-1} that is weakly but positively correlated to the (479,551) cm^{-1} band pair just as in NCA.

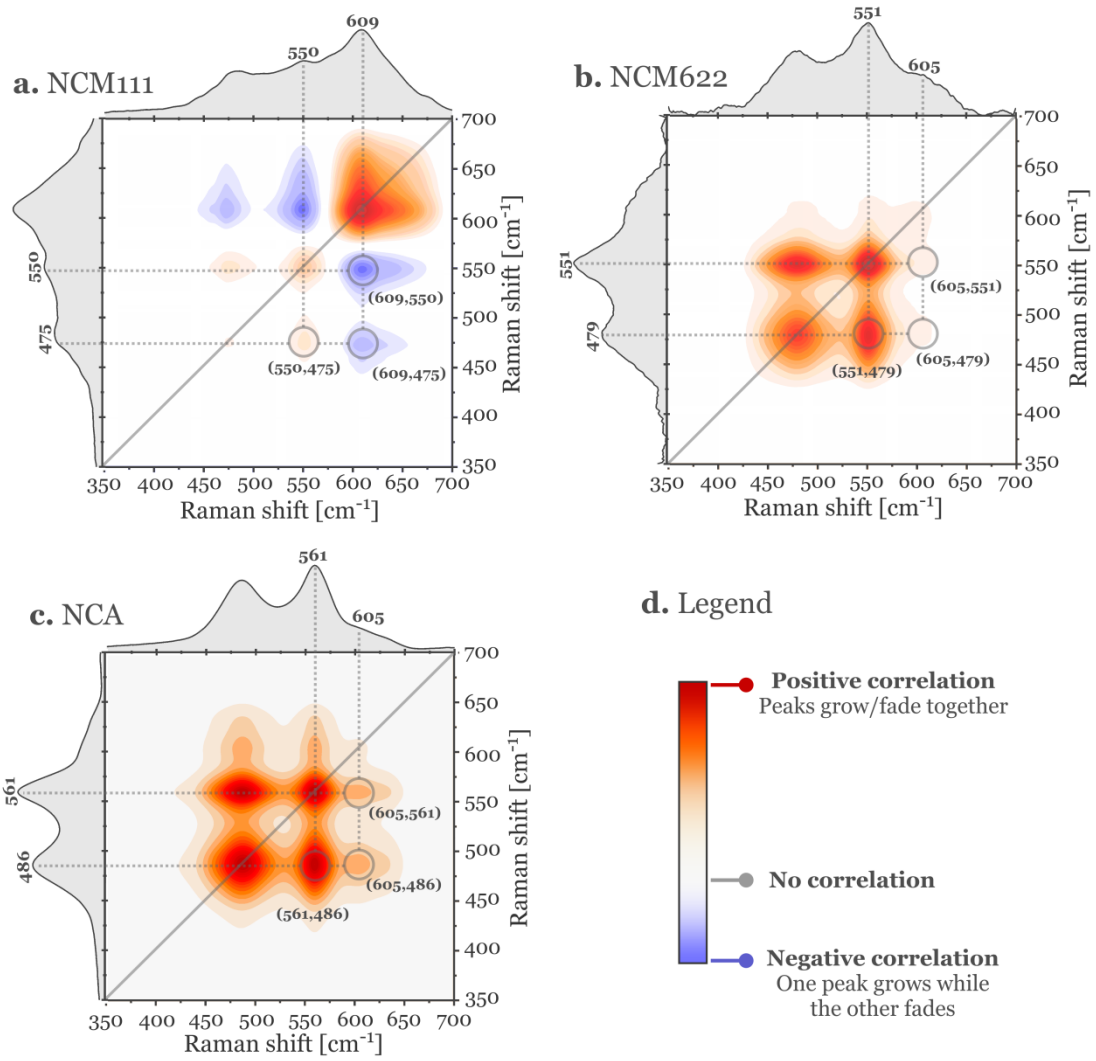

Figure 8.5. Synchronous maps resulting from the generalized bidimensional correlation analysis of **a.** NCM111, **b.** NCM622 and **c.** NCA. The encircled regions highlight correlation zones. **d.** Color code of the correlation maps.

The correlation maps demonstrate that lithium vacancy bands also contribute to the intensity variations of the NCM622 spectra within the 600-630 cm^{-1} region, thus confirming the interpretation that the U-shaped trend of *I(v3)* is a crossover between opposing intensity trends from Mn-related bands and lithium vacancy bands. All NCM622 Raman bands can be now assigned in the same way as those of NCM811 summarized in Table 7.1. Lithium vacancy bands are also expected to occur in the Raman spectrum of delithiated NCM111, however, only in NCM622 the Mn-related bands are weak enough to permit identification of the lithium vacancy bands.

8.5 Summary

In this chapter the *operando* Raman spectra of NCM111 and NCM622 is analyzed using automated peak fitting, multivariate curve resolution (MCR) and the generalized correlation analysis. The trends retrieved were compared to the electrochemical response of the oxide in order to draw conclusions about the occurrence and nature of phase transitions during cycling. The cycling dependent evolution of NCM111 spectra correlates with the two-step charge compensation process of nickel. The Raman intensity trends of both oxides — obtained from NCM111 by MCR analysis and from NCM622 by automated peak fitting — inflect at low SOL and represent a spectral signature of oxygen oxidation at the oxide's bulk. Overcharge aggravates the irreversibility in the potential profiles and intensity trends of NCM111 but much less for the trends of NCM622. Last, both peak fitting and correlation maps demonstrate that the redox peak ca. 3.74 V — common for all Ni-containing oxides — originate from a configurational phase transition between order/disordered lithium vacancy configurations.

Chapter 9 Conclusions and outlook

In lithium-ion battery research, the main goal of any characterization technique is identifying fundamental properties and operating mechanisms of cell components, which can be then eventually translated into principles for improvement. In this thesis work both an advanced *operando* electrochemical cell and a set of data processing routines have been developed for recording and analyzing the Raman spectra of electrode materials under operation. The utility and potential of the developed methodology have been demonstrated on several commercially-relevant $LiMO_2$ Li-ion cathode materials. Here the main research outputs of this work are summarized and classified into technical developments (hardware and data analysis), fundamental understanding (spectrum-property relationships) and diagnostic outreach (meaningful findings about $LiMO_2$ enabled by the developed methodology). In addition, each section discusses potential directions of improvement and multiple perspectives for future work.

9.1 Technical development

9.1.1 *Operando* Raman cell

A new *operando* electrochemical cell has been developed for recording the Raman spectra of electrode materials while they cycle within their operating environment (Figure 9.1a). The cell design conforms to key design principles required to guarantee:

- Optimal electrochemical performance, allowing the accurate estimation and correlation of electrode phenomena to the state of lithiation; the electrochemical performance of the developed cell is benchmarked against the literature.
- High Raman signal quality, facilitating detailed spectral analysis and high time resolution. The cell's signal quality is superior in comparison to the ones found on similar studies in the literature (Table 9.1).

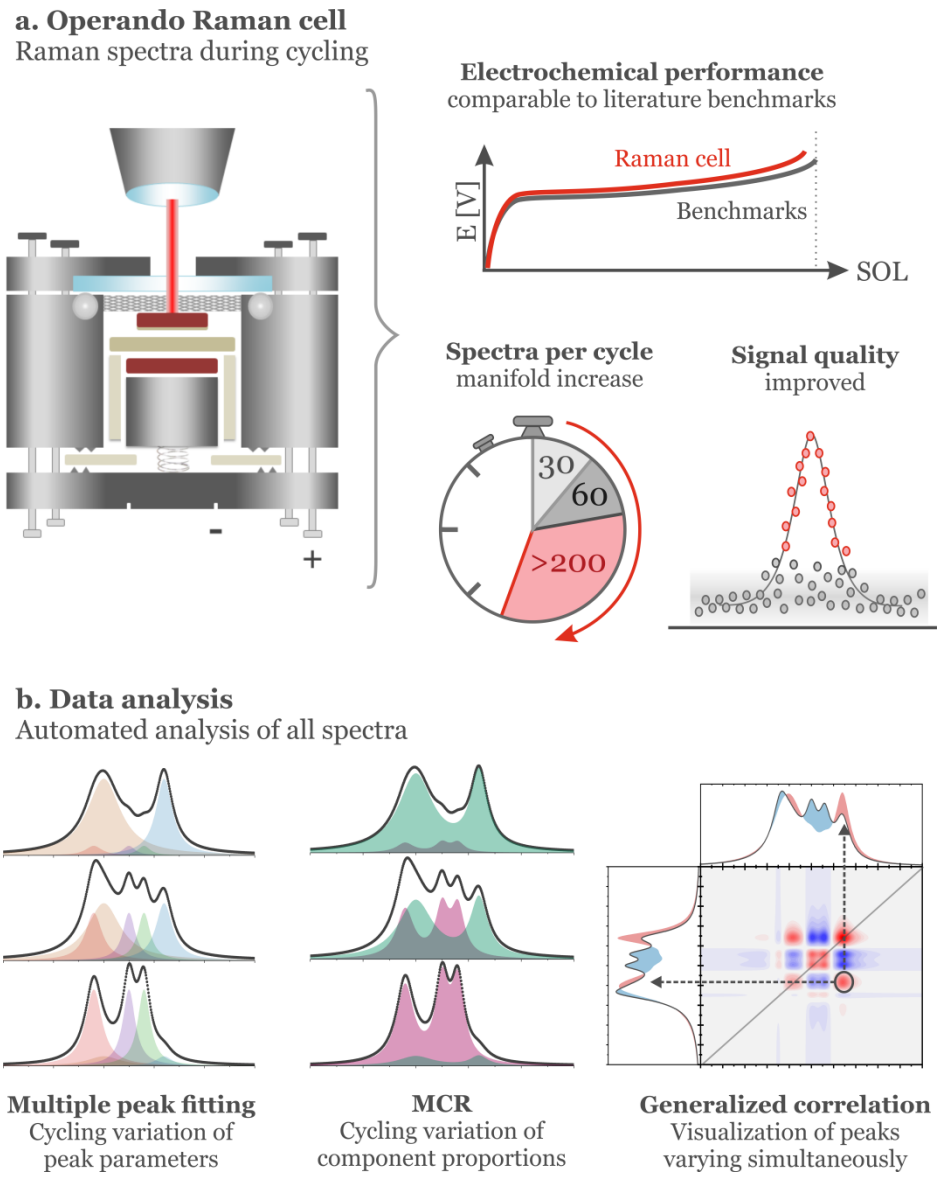

Figure 9.1. Technical development of the thesis work. **a.** The *operando* Raman cell features improved electrochemical performance, signal quality and cycling resolution. **b.** Automated data processing tools implemented for obtaining trends from the spectral data.

Table 9.1. Raman measurement results from the best examples of *in situ*/*operando* experiments found in the literature.

Oxide	Spectra per cycle	Signal quality	Reference
LCO	25		[168]
	550	Comparable	This work
NCA	30		[160]
	240	Improved	This work
NCM111	60		[161]
	100	Improved	This work
NCM811	20		[173]
	190	Improved	This work

The recording at narrow SOL cycling intervals, enabled by the developed cell (more than one spectrum every 0.01 Li^+ per formula), become limited by SOL deviations (up to 0.1 Li^+ per formula) originating from lithium loss and overpotentials. These undesirable processes also introduce discrepancies between repeated experiments using different electrodes. Better SOL accuracy could be achieved by resorting to i) commercially-prepared composite electrode sheets with highly controlled electrode parameters (e.g. thickness, porosity, loading, homogeneity) and ii) a less reactive substitute of the lithium metal anode, e.g. lithium titanate oxide, to minimize interference from electrode crosstalk.[266]

9.1.2 Data analysis

High SOL-resolution comes along with a data-processing challenge. Instead of drawing conclusions from few sample spectra, this work extracts robust and meaningful patterns from all spectra, by implementing several Matlab-based routines and a graphical user interface (GUI). The scripts enable the selection, visual inspection and execution of the mathematical functions applied to automated baseline-correction and peak fitting of the hundreds of spectra retrieved from each *operando* experiment. The resulting fitting parameters outline SOL-dependent trends, characteristic of the cycling behavior of the oxides (Figure 9.1b).

In the case of NCM111, band overlap renders the fitting procedure highly sensitive to the arbitrary constraints of the fitting model. Hence, multivariate curve resolution (MCR) procedure has been applied as an alternative, non-arbitrary way of obtaining cycling-dependent spectral trends. The protocol and a GUI, provided by reference [163], yield robust and insightful SOL-dependent spectral trends of NCM111. In addition, the

generalized correlation analysis (implemented in a script as part of this work) enables visualization of concerted/competing SOL-dependent changes between pair of Raman bands, highlighting thus those bands likely sharing physical origin. All these scripts can be further made accessible to any independent user if they are polished and integrated into an intuitive GUI with a comprehensive protocol of use.

9.2 Fundamental understanding: spectrum-property relationships

Drawing conclusions from the spectral trends requires understanding why (de)lithiation shifts the position of the Raman bands (in wavenumbers), changes their intensities and/or causes new Raman-active bands. In this work, the relationships between spectral trends and fundamental properties of the oxides have been established by applying symmetry base models (i.e. nuclear site group analysis), classical electrodynamics, first-principles (DFT) phonon calculations and complementary experiments. The main spectrum-property relationships found are (Figure 9.2):

- The Raman band intensities of Li_xCoO_2 (LCO) abruptly disappear during the course of a first-order phase transition. Based on a classical model of light attenuation, the sudden change of intensity is attributed to large differences in the photon absorption properties of the two phases coexisting during the transition.

- New bands close to 600 cm^{-1} grow during delithiation of Ni-containing oxides. First-principles phonon calculations indicate that they originate from the modification of the oxygen site symmetry by the ordering of lithium and its vacancies. Complementary experiments discard other possible origins.

- In Ni-rich oxides, the Raman intensity variations in the spectra are likely to originate from changes in the electron density around oxygen atoms, while band shifts reflect the degree of metal-oxygen covalency, as indicated by first-principles phonon calculations.

- The fine structure of the peak-position trends exhibit plateaus that relate to the occurrence of phase transitions. The correlation is explained based on an abstract lattice energy space, relating the electrode potential and the band wavenumber to phase transition events.

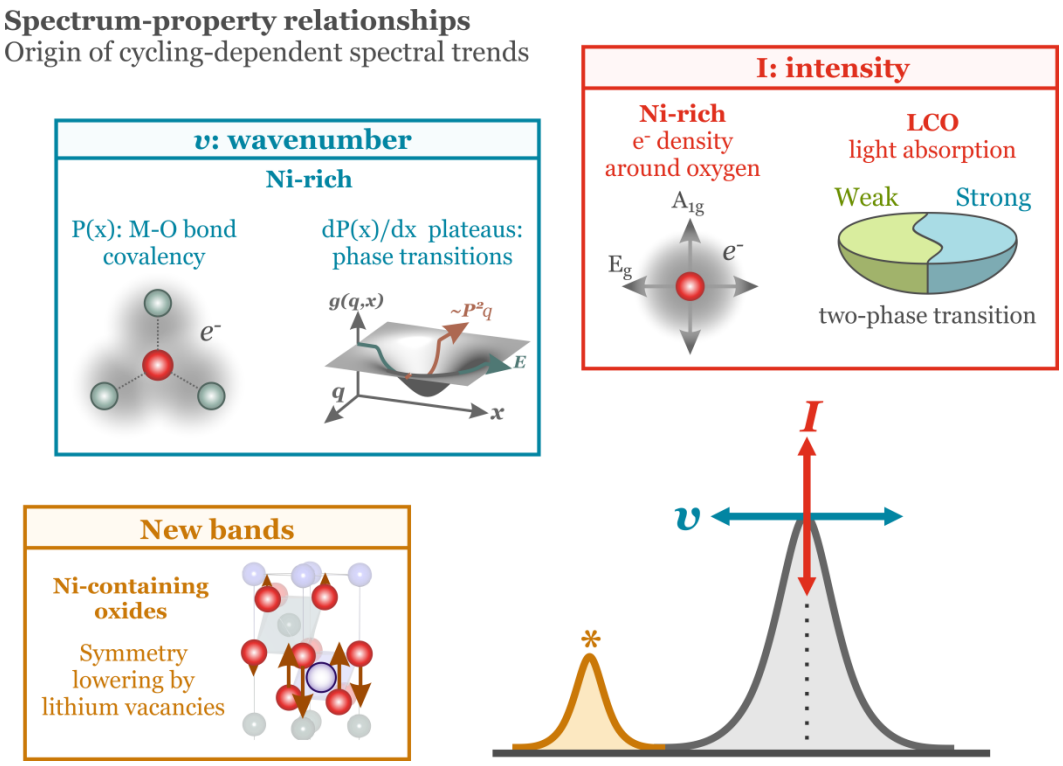

Figure 9.2. Main relationships found between the spectral trends and properties of the oxides.

Further insights into the fundamental relationships between spectral features and material properties require multiple approaches, of which the model substrates, complementary techniques and theoretical modeling deserve emphasis:

- $LiMO_2$ single crystals with sufficiently defect-free lattices can act as model electrodes for investigating the dependence of the Raman bands on crystal size and orientation, temperature, light polarization and wavelength, enabling thus the identification of the symmetry of the modes and their interactions with electronic and magnetic properties of the oxides.[169,170,267] In particular, the demonstrated propensity of $LiMO_2$ to resonance Raman effect opens the door for investigating the electronic structure of the oxides via the wavelength-dependency of the Raman spectra.[139]

- While diffraction-refined structures are the starting point for establishing symmetry-based predictions of the vibrational spectrum, the long-ranged crystallographic changes are not always correlated to the Raman spectral trends during cycling. Therefore, other local probes such as nuclear magnetic resonance[62] and X-ray absorption near-edge spectroscopy[61] are more suitable for complementing the short-range information provided by Raman spectroscopy.

- Simulating the Raman spectra of $LiMO_2$ using first-principles DFT-based calculations is challenging. Reliable predictions of the spectra require modelling of the local structure

accurately and calculating the interatomic interactions with meV-precision.[143] Moreover, the simulation of Raman intensities requires computationally-intensive calculations of the effect that the atomic displacements have on the dielectric properties of the lattice.[133,268] For these reasons, only a few theoretical studies of the Raman spectra of $LiMO_2$ have been reported so far. This work demonstrates the usefulness of such calculations for establishing spectrum-property relationships, justifying thus further efforts towards improving their accuracy and feasibility.

9.3 Diagnostic outreach

The technical development and fundamental understanding achieved in this work had permitted a comprehensive investigation of the structure and dynamics of commercially-relevant cathodes during cycling. The main findings are:

- The band multiplicity in the Raman spectra of $LiMO_2$ (except $LiCoO_2$) indicates that oxygen atoms occupy deformed environments that cannot be described by the long-ranged crystallographic $R\bar{3}m$ lattice.

- The temperature-dependent Raman spectrum of $LiNiO_2$ (LNO) and DFT calculations indicate that this oxide undergoes a rhombohedral-to-monoclinic phase transition when the temperature is lowered below -70 °C (Figure 9.3a). The transition is likely driven by the cooperative alignment of Jahn-Teller distorted Ni-O bonds.

- The agreement between experimental and calculated Raman spectra permitted identification of a short-ranged superlattice ordering of transition metals in $LiNi_{0.33}Co_{0.33}Mn_{0.33}O_2$ (NCM111) (Figure 9.3b), supporting previous observations in the literature. The triangular arrangement of transition metals could be key to the known cycling stability of NCM111.[84]

- Resonance Raman spectroscopy suggests that the *c*-axis parameter length of the $R\bar{3}m$ lattice is controlled by the electron density at the e_g^* anti-bonding states of nickel.

- The sudden disappearance of the Raman-active bands of Li_xCoO_2 during the first-order phase transition evidence that the two coexisting phases exhibit large differences not only in electronic conductivity, but also in their light absorption properties (Figure 9.3c). Preliminary experiments suggest the possibility of investigating the kinetics of the phase transition via the hysteresis in the Raman intensity trends.

- The step-change on the Raman intensity trends of $Li_xNi_{0.8}Co_{0.15}Al_{0.05}O_2$ (NCA) during the first cycle reveals an electrochemically-triggered process occurring ca. 3.76 V, likely

related to the dissolution of a Li^+ blocking $–CO_3$ surface layer that influences mass transport and ohmic overpotentials (Figure 9.3d).[234]

- An inflection in the Raman intensity trends at low SOL indicates that all Ni-containing oxides undergo an electronic transition to a bulk anionic charge-compensation process (Figure 9.3e). Oxygen oxidation at the particles' surface and the associated side reactions results in the evolution of O_2 and CO_2 gases and precedes the abrupt and deleterious *c*-axis contraction of Ni-rich oxide lattices (Figure 9.3f).

- A trend hysteresis of the Raman peak wavenumbers and intensities indicates that NCM811 (Mn-containing oxide) is comparatively more resilient than NCA (Mn-free oxide) against the irreversible mechanical deterioration of the lattice during overcharge.

- The cycling-dependent evolution of Raman-active bands above 600 cm^{-1} indicates that the redox couple at ca. 3.73 V — common for all Ni-containing oxides — originates from a configurational phase transition between lithium-vacancy orderings (Figure 9.3g). The universality of the process supports a theoretically-predicted interaction between the electronic structure of nickel and lithium ordering,[269] and also suggests that such transitions can be tuned by controlling the electronic structure of the oxide.

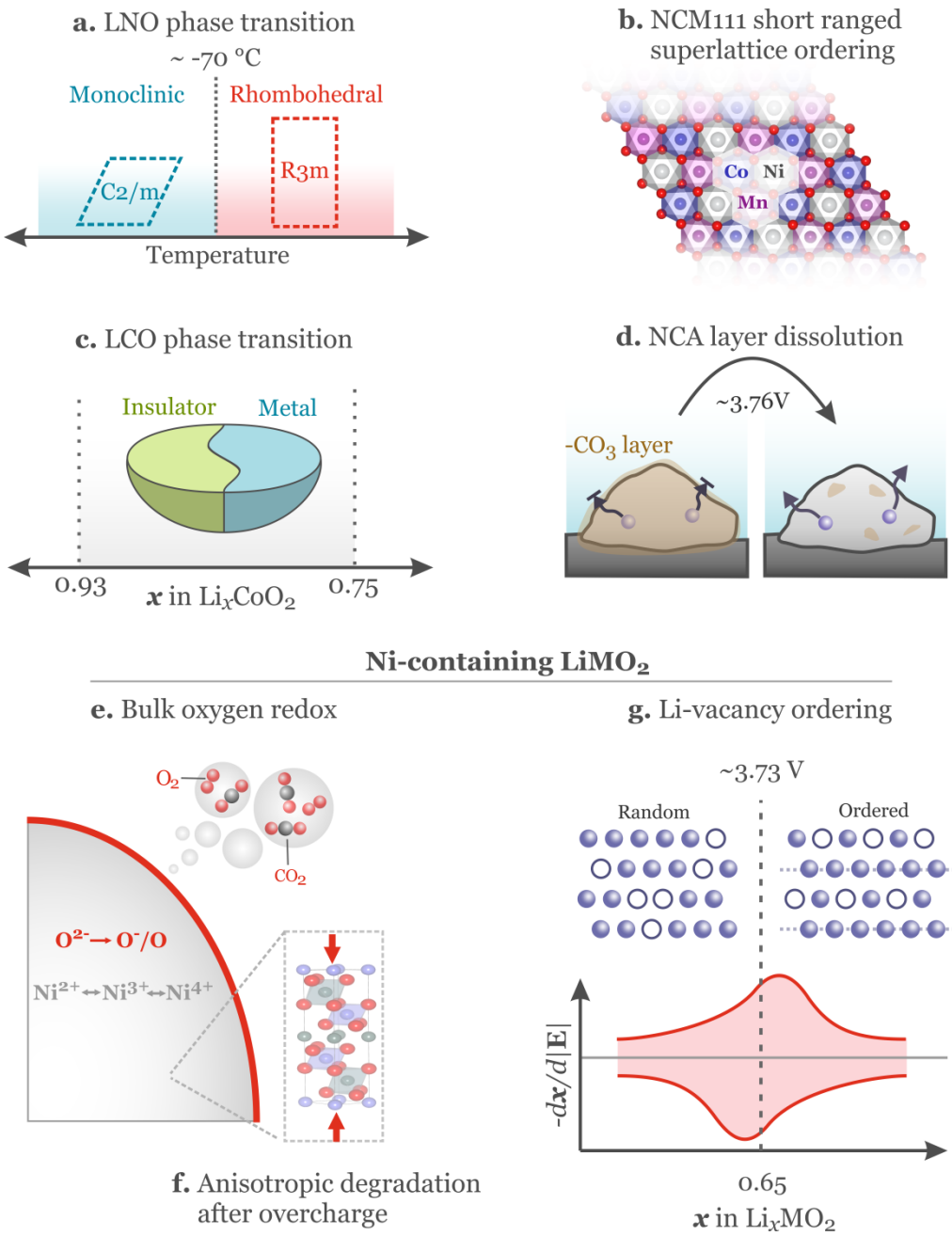

Figure 9.3. Graphical abstract of the main findings enabled by *operando* Raman spectroscopy about the properties and dynamics of $LiMO_2$ oxides. **a.** Low-temperature phase transition of LNO. **b.** Short-ranged superlattice ordering in NCM111. **c.** First-order phase transition of LCO. **d.** Electrochemically-triggered dissolution of a carbonate layer at the surface of NCA. **e.** Bulk oxygen charge-compensation process of Ni-rich oxides, which precedes **f.** the anisotropic and irreversible degradation of the lattice. **g.** Configurational phase transition of all Ni-containing oxides ~ 3.73 V.

The new fundamental insights into the properties and cycling behavior of $LiMO_2$ demonstrate the diagnostic capability of *operando* Raman spectroscopy for the characterization of electrode materials. The technique and methodology developed in this thesis work carry great potential for further application in investigating electrochemical phenomena, key to the overall improvement of Li-ion batteries. Future directions of work could exploit the diagnostic capability of the technique by focusing on:

- *Resolving spatial heterogeneities.* Given the high SOL-resolution, enabled by the developed cell, the detailed dependencies between spectral trends and lithium content can be used for contrasting the SOL of secondary particles within the composite electrode. *In situ* Raman maps have been reported before[182,225,264,270], but the newly developed cell combined with the automated analysis tools are anticipated to yield detailed maps with improved chemical contrast, capable of detecting small SOL heterogeneities (Δx in Li_xMO_2 < 0.1) and their evolution during cycling. The maps could prove useful in guiding, for instance, the optimization of the electrode and material microstructure and preparation.[271]

- *Enhancing time resolution and surface sensitivity.* The robust methodology developed could be used to identify reproducible and meaningful spectral trends from *operando* experiments using surface enhanced Raman spectroscopy (SERS). In SERS the signal from weakly Raman-scattering species is strongly enhanced by the plasmon resonance phenomena that the incident radiation stimulates on metal surfaces with nanometer-sized geometrical features.[272] SERS could potentially provide access to phenomena occurring at the electrode-electrolyte interface and with very fast acquisition times. For instance, the Raman intensity of $LiNi_{0.5}Co_{0.2}Mn_{0.3}O_2$ (NCM523) can be plasmon-enhanced by two orders of magnitude when the particles of active material are electroplated with sub-micron gold clusters[178]; hence, the spectra recording times can be potentially reduced from fractions of hour to a few seconds. However, the highly reactive gold clusters are likely not stable in contact with the electrolyte at high anodic potentials. As a remedy, the plasmonic nanoparticles can be coated with a thin layer of an inert oxide in order to passivate the reactive surfaces (shell-isolated nanoparticle-enhanced Raman spectroscopy i.e. SHINERS).[273] The approach had been used *in situ* to detect the formation of Li_2O at the surface of the Li-rich NCM but the bands were barely above the noise level and the signals from the oxide were not detected.[274] In general SHINERS have been seldom applied on electrode materials because (i) the electrode surface is rough, heterogeneous and difficult to coat uniformly, and (ii) the challenging synthesis required to produce highly controlled shell isolated nanoparticles able to yield reproducible results.[275] However, the promise of resolving second and sub-second electrode dynamics and detecting interface phenomena warrants further development of *operando* SHINERS.

- *Characterizing performance improvement.* The improvement of the electrochemical performance of $LiMO_2$ Li-ion cathodes has been approached via multiple strategies that include cation doping,[276] surface coatings,[51] composition gradients[50] and electrolyte additives[277]. While these strategies do ameliorate performance, the exact mechanisms by which they do remain unclear. Based on the results of this work, *operando* Raman spectroscopy could detect whether these electrode modifications alter the resilience of the oxide against mechanical deterioration, inhibit anionic redox, disrupt/promote cation ordering, etc. The ability to pinpoint the exact mechanism of improvement enables the rational design of new, more efficient methodologies for fabricating better-performing cathode materials.

Appendix A Abbreviations and references

A.1 Abbreviations and symbols

List of Abbreviations

DFT	Density functional theory
DMC	Dimethyl carbonate
EC	Ethylene carbonate
GUI	Graphical user interface
HDPE	High density polyethylene
HF	Hydrofluoric acid
IA	Intra-layer
IE	Inter-layer
JT	Jahn-Teller
LC30	1.0 M $LiClO_4$ in 1:1 (w/w) EC/DMC
LCO	$LiCoO_2$
LE	Lowest-energy
LIB	Lithium-ion battery
LMO	$LiMnO_2$
LNO	$LiNiO_2$
MCR	Multivariate curve resolution
NCA	$LiNi_{0.8}Co_{0.15}Al_{0.05}O_2$
NCM	$LiNi_{1-a-b}Co_aMn_bO_2$
NCM111	$LiNi_{0.33}Co_{0.33}Mn_{0.33}O_2$
NCM523	$LiNi_{0.5}Co_{0.2}Mn_{0.3}O_2$
NCM622	$LiNi_{0.6}Co_{0.2}Mn_{0.2}O_2$
NCM811	$LiNi_{0.8}Co_{0.1}Mn_{0.1}O_2$
NMP	n-methyl pyrrolidone
NMR	Nuclear magnetic resonance
OCP	Open circuit potential
PTFE	Polytetrafluoroethylene
PVdF	Polyvinylidene difluoride
RT	Room temperature
SERS	Surface-enhanced Raman spectroscopy
SHINERS	Shell-isolated nanoparticle-enhanced Raman spectroscopy
SOL	State of lithiation

List of symbols

a.u.	Arbitrary units
α	Electric polarizability
c	Speed of light in vacuum
d	Spot-size diameter
ΔU	Cell voltage
Δ_O	Octahedral-field splitting gap
D_f	Depth of focus
e	Elementary unit of charge
E	Electrode potential
$\boldsymbol{E}$	Electric field
ε	Electric permittivity
ε_0	Electric permittivity of vacuum
F_E	Fermi energy
g	Gibbs free energy per formula unit
γ	Optical absorption coefficient
g_m	Frequency degeneracy
h	Plank's constant
I	Intensity
k	Spring constant
k_B	Boltzmann's constant
λ	Wavelength
m	Mass
μ	Magnetic permeability
$\mu_{electrode}$	Electrode chemical potential
$\boldsymbol{\mu'}$	Electric dipole induced by incident radiation
μ_B	Bohr magneton
μ_m	Electric dipole induced by normal mode
n	Vibrational energy level
NA	Numerical aperture
N_m	Number of normal modes
η	Overpotential
P	Peak position
Ψ	Quantum vibrational state
q	Displacement coordinate
σ	Electronic conductivity
t	Time
T	Temperature

A.2 List of Figures

A.3 List of Tables

A.4 References

1 United Nations Climate Change Secretariat, *The Paris Agreement*, 2018.

2 B. Obama, *Science (80-.).*, 2017, **355**, 126–129.

3 Tsiropoulos I, Tarvydas D and Lebedeva N, *Li-ion batteries for mobility and stationary storage applications Scenarios for costs and market growth*, 2018.

4 Z. Yang, J. Zhang, M. C. W. Kintner-Meyer, X. Lu, D. Choi, J. P. Lemmon and J. Liu, *Chem. Rev.*, 2011, **111**, 3577–3613.

5 E. J. Cairns and P. Albertus, *Annu. Rev. Chem. Biomol. Eng.*, 2010, **1**, 299–320.

6 W. R. McKinnon and R. R. Haering, in *Modern Aspects of Electrochemistry*, Springer US, Boston, MA, 1983, pp. 235–304.

7 P. Atkin and J. Paula, *Physical chemistry*, 2006.

8 R. J. Masaki, Yoshio, Kozawa, Akiya, Brodd, *Lithium-Ion Batteries. Science and Technologies*, Springer New York, New York, NY, 2009.

9 J.-M. Tarascon, *Philos. Trans. A. Math. Phys. Eng. Sci.*, 2010, **368**, 3227–41.

10 R. Robert, C. Villevieille and P. Novák, *J. Mater. Chem. A*, 2014, **2**, 8589.

11 K. Edström, T. Gustafsson and J. O. Thomas, *Electrochim. Acta*, 2004, **50**, 397–403.

12 J. B. Goodenough and Y. Kim, *Chem. Mater.*, 2010, **22**, 587–603.

13 B. Ziv, V. Borgel, D. Aurbach, J.-H. Kim, X. Xiao and B. R. Powell, *J. Electrochem. Soc.*, 2014, **161**, A1672–A1680.

14 G. E. Blomgren, *J. Electrochem. Soc.*, 2017, **164**, A5019–A5025.

15 B. L. Ellis, K. T. Lee and L. F. Nazar, *Chem. Mater.*, 2010, **22**, 691–714.

16 J. W. Fergus, *J. Power Sources*, 2010, **195**, 939–954.

17 J. N. Reimers and J. R. Dahn, *J. Electrochem. Soc.*, 1992, **139**, 2091.

18 X. Lu, Y. Sun, Z. Jian, X. He, L. Gu, Y.-S. Hu, H. Li, Z. Wang, W. Chen, X. Duan, L. Chen, J. Maier, S. Tsukimoto and Y. Ikuhara, *Nano Lett.*, 2012, **12**, 6192–6197.

19 G. G. Amatucci, J. M. Tarascon and L. C. Klein, *Solid State Ionics*, 1996, **83**, 167–173.

20 D. Ensling, G. Cherkashinin, S. Schmid, S. Bhuvaneswari, A. Thissen and W. Jaegermann, *Chem. Mater.*, 2014, **26**, 3948–3956.

21 J. R. Dahn, U. von Sacken, M. W. Juzkow and H. Al-Janaby, *J. Electrochem. Soc.*, 1991, **138**, 2207.

22 Y. Kobayashi, M. Tabuchi, H. Miyashiro and N. Kuriyama, *J. Power Sources*, 2017, **364**, 156–162.

23 T. Ohzuku, A. Ueda, M. Nagayama, Y. Iwakoshi and H. Komori, *Electrochim. Acta*, 1993, **38**, 1159–1167.

24 J. Xu, E. Hu, D. Nordlund, A. Mehta, S. N. Ehrlich, X.-Q. Yang and W. Tong, *ACS Appl. Mater. Interfaces*, 2016, **8**, 31677–31683.

25 P. Kalyani and N. Kalaiselvi, *Sci. Technol. Adv. Mater.*, 2005, **6**, 689–703.

26 I. Saadoune and C. Delmas, *J. Solid State Chem.*, 1998, **136**, 8–15.

27 C. Delmas and L. Croguennec, *MRS Bull.*, 2002, **27**, 608–612.

28 C. H. Chen, J. Liu, M. E. Stoll, G. Henriksen, D. R. Vissers and K. Amine, *J. Power Sources*, 2004, **128**, 278–285.

29 N. Nitta, F. Wu, J. T. Lee and G. Yushin, *Mater. Today*, 2015, **18**, 252–264.

30 S. Hwang, W. Chang, S. M. Kim, D. Su, D. H. Kim, J. Y. Lee, K. Y. Chung and E. a Stach, *Chem. Mater.*, 2014, **26**, 1084–1092.

31 E. Jo, S. Hwang, S. M. Kim and W. Chang, *Chem. Mater.*, 2017, **29**, 2708–2716.

32 J. Cho, H. Jung, Y. Park, G. Kim and H. S. Lim, *J. Electrochem. Soc.*, 2000, **147**, 15.

33 H. F. Xiang, H. Wang, C. H. Chen, X. W. Ge, S. Guo, J. H. Sun and W. Q. Hu, *J. Power Sources*, 2009, **191**, 575–581.

34 L. Wu, K.-W. Nam, X. Wang, Y. Zhou, J.-C. Zheng, X.-Q. Yang and Y. Zhu, *Chem. Mater.*, 2011, **23**, 3953–3960.

35 G. Vitins and K. West, *J. Electrochem. Soc.*, 1997, **144**, 2587.

36 M. S. Whittingham, *Chem. Rev.*, 2004, **104**, 4271–4302.

37 L. Croguennec, P. Deniard and R. Brec, *J. Electrochem. Soc.*, 1997, **144**, 3323.

38 P. G. Bruce, A. R. Armstrong and R. L. Gitzendanner, *J. Mater. Chem.*, 1999, **9**, 193–198.

39 J. Molenda, M. Ziemnicki, J. Marzec, W. Zając, M. Molenda and M. Bućko, *J. Power Sources*, 2007, **173**, 707–711.

40 Y. Idemoto, T. Mochizuki, K. Ui and N. Koura, *J. Electrochem. Soc.*, 2006, **153**, A418.

41 C. M. Julien, A. Mauger, K. Zaghib and H. Groult, *Inorganics*, 2014, **2**, 132–154.

42 D. D. MacNeil, Z. Lu and J. R. Dahn, *J. Electrochem. Soc.*, 2002, **149**, A1332.

43 P. He, H. Yu, D. Li and H. Zhou, *J. Mater. Chem.*, 2012, **22**, 3680–3695.

44 I. Belharouak, Y.-K. Sun, J. Liu and K. Amine, *J. Power Sources*, 2003, **123**, 247–252.

45 K.-S. Lee, S.-T. Myung, K. Amine, H. Yashiro and Y.-K. Sun, *J. Electrochem. Soc.*, 2007, **154**, A971.

46 H. J. Noh, S. Youn, C. S. Yoon and Y. K. Sun, *J. Power Sources*, 2013, **233**, 121–130.

47 L. De Biasi, A. O. Kondrakov, H. Geßwein, T. Brezesinski, P. Hartmann and J. Janek, *J. Phys. Chem. C*, 2017, **121**, 26163–26171.

48 H. H. Ryu, K. J. Park, C. S. Yoon and Y. K. Sun, *Chem. Mater.*, 2018, **30**, 1155–1163.

49 S. Wang, M. Yan, Y. Li, C. Vinado and J. Yang, *J. Power Sources*, 2018, **393**, 75–82.

50 S. T. Myung, F. Maglia, K. J. Park, C. S. Yoon, P. Lamp, S. J. Kim and Y. K. Sun, *ACS Energy Lett.*, 2017, **2**, 196–223.

51 W. Liu, P. Oh, X. Liu, M.-J. Lee, W. Cho, S. Chae, Y. Kim and J. Cho, *Angew. Chemie Int. Ed.*, 2015, **54**, 4440–4457.

52 A. Manthiram, B. Song and W. Li, *Energy Storage Mater.*, 2017, **6**, 125–139.

53 M. Dixit, B. Markovsky, F. Schipper, D. Aurbach and D. T. Major, *J. Phys. Chem. C*, 2017, **121**, 22628–22636.

54 J. Kim, H. Lee, H. Cha, M. Yoon, M. Park and J. Cho, *Adv. Energy Mater.*, 2018, **8**, 1–25.

55 N. Sharma, W. K. Pang, Z. Guo and V. K. Peterson, *ChemSusChem*, 2015, **8**, 2826–2853.

56 L. Vitoux, M. Reichardt, S. Sallard, P. Novák, D. Sheptyakov and C. Villevieille, *Front. Energy Res.*, 2018, **6**, 1–16.

57 M. Balasubramanian, X. Sun, X. . Yang and J. McBreen, *J. Power Sources*, 2001, **92**, 1–8.

58 A. M. Balagurov, I. A. Bobrikov, N. Y. Samoylova, O. A. Drozhzhin and E. V Antipov, *Russ. Chem. Rev.*, 2014, **83**, 1120–1134.

59 S.-C. Yin, Y.-H. Rho, I. Swainson and L. F. Nazar, *Chem. Mater.*, 2006, **18**, 1901–1910.

60 K.-W. Nam, S.-M. Bak, E. Hu, X. Yu, Y. Zhou, X. Wang, L. Wu, Y. Zhu, K.-Y. Chung and X.-Q. Yang, *Adv. Funct. Mater.*, 2013, **23**, 1047–1063.

61 J. McBreen, *J. Solid State Electrochem.*, 2009, **13**, 1051–1061.

62 C. P. Grey and N. Dupré, *Chem. Rev.*, 2004, **104**, 4493–4512.

63 R. Huang and Y. Ikuhara, *Curr. Opin. Solid State Mater. Sci.*, 2012, **16**, 31–38.

64 M. Shao, *J. Power Sources*, 2014, **270**, 475–486.

65 J. Tan, D. Liu, X. Xu and L. Mai, *Nanoscale*, 2017, 19001–19016.

66 R. Baddour-Hadjean and J.-P. Pereira-Ramos, *Chem. Rev.*, 2009, **110**, 1278–1319.

67 E. Flores, P. Novák and E. J. Berg, *Front. Energy Res.*, 2018, **6**, 1–16.

68 C. Delmas, C. Fouassier and P. Hagenmuller, *Phys. B+C*, 1980, **99**, 81–85.

69 M. Park, X. Zhang, M. Chung, G. B. Less and A. M. Sastry, *J. Power Sources*, 2010, **195**, 7904–7929.

70 G.-A. Nazri and G. Pistoia, Eds., *Lithium Batteries. Science and Technology*, Springer US, Boston, MA, 2003.

71 T. Ohzuku and A. Ueda, *Solid State Ionics*, 1994, **69**, 201–211.

72 W. Li, B. Song and A. Manthiram, *Chem. Soc. Rev*, 2017, **3006**, 3006.

73 F. Schipper, E. M. Erickson, C. Erk, J.-Y. Shin, F. F. Chesneau and D. Aurbach, *J. Electrochem. Soc.*, 2017, **164**, A6220–A6228.

74 I. Bersuker, *Structure and Properties of Transition Metal Compounds*, John Wiley & Sons, Inc., Hoboken, NJ, USA, 2nd edn., 2010.

75 M. K. Aydinol, A. F. Kohan, G. Ceder, K. Cho and J. Joannopoulos, *Phys. Rev. B*, 1997, **56**, 1354–1365.

76 D.-H. Seo, J. Lee, A. Urban, R. Malik, S. Kang and G. Ceder, *Nat. Chem.*, 2016, **8**, 692–697.

77 J. B. Goodenough, *Prog. Solid State Chem.*, 1971, **5**, 145–399.

78 C. Liu, Z. G. Neale and G. Cao, *Mater. Today*, 2016, **19**, 109–123.

79 H. A. Jahn and E. Teller, *Proc. R. Soc. A Math. Phys. Eng. Sci.*, 1937, **161**, 220–235.

80 H. Chen, C. L. Freeman and J. H. Harding, *Phys. Rev. B - Condens. Matter Mater. Phys.*, 2011, **84**, 1–7.

81 M. D. Johannes, K. Swider-Lyons and C. T. Love, *Solid State Ionics*, 2016, **286**, 83–89.

82 D. P. Abraham, R. D. Twesten, M. Balasubramanian, J. Kropf, D. Fischer, J. McBreen, I. Petrov and K. Amine, *J. Electrochem. Soc.*, 2003, **150**, A1450.

83 D. D. MacNeil, Z. Lu, Z. Chen and J. R. Dahn, *J. Power Sources*, 2002, **108**, 8–14.

84 C. Liang, F. Kong, R. C. Longo, K. C. Santosh, J. S. Kim, S. H. Jeon, S. A. Choi and K. Cho, *J. Phys. Chem. C*, 2016, **120**, 6383–6393.

85 N. Yabuuchi, Y. Koyama, N. Nakayama and T. Ohzuku, *J. Electrochem. Soc.*, 2005, **152**, A1434.

86 K. Okamoto, K. Shizuka, T. Akai, Y. Tamaki, K. Okahara and M. Nomura, *J. Electrochem. Soc.*, 2006, **153**, A1120.

87 B. Scrosati, K. M. Abraham, W. A. van. Schalkwijk and J. Hassoun, *Lithium Batteries : Advanced Technologies and Applications.*, Wiley, 2013.

88 J. B. Goodenough and K. Park, *J. Am. Chem. Soc.*, 2013, **135**, 1167–1176.

89 A. Van der Ven, J. Bhattacharya and A. A. Belak, *Acc. Chem. Res.*, 2013, **46**, 1216–1225.

90 D. A. Porter and K. E. Easterling, *Phase Transformations in Metals and Alloys*, Springer US, Boston, MA, 2nd edn., 1992.

91 D. Li and H. Zhou, *Mater. Today*, 2014, **17**, 451–463.

92 J. R. Dahn and W. R. McKinnon, *J. Electrochem. Soc.*, 1984, **131**, 1823.

93 G. Ceder and A. Van der Ven, *Electrochim. Acta*, 1999, **45**, 131–150.

94 A. Van der Ven, M. Aydinol, G. Ceder, G. Kresse and J. Hafner, *Phys. Rev. B*, 1998, **58**, 2975–2987.

95 M. E. Arroyo y de Dompablo, A. Van der Ven and G. Ceder, *Phys. Rev. B*, 2002, **66**, 064112.

96 C. A. Marianetti, G. Kotliar and G. Ceder, *Nat. Mater.*, 2004, **3**, 627–631.

97 M. D. Radin, J. Alvarado, Y. S. Meng and A. Van Der Ven, *Nano Lett*, 2017, **17**, 1.

98 A. Van der Ven and M. Wagemaker, *Electrochem. commun.*, 2009, **11**, 881–884.

99 M. D. Radin, S. Hy, M. Sina, C. Fang, H. Liu, J. Vinckeviciute, M. Zhang, M. S. Whittingham, Y. S. Meng and A. Van der Ven, *Adv. Energy Mater.*, 2017, **7**, 1602888.

100 R. Hausbrand, G. Cherkashinin, H. Ehrenberg, M. Gröting, K. Albe, C. Hess and W. Jaegermann, *Mater. Sci. Eng. B*, 2015, **192**, 3–25.

101 J. Vetter, P. Novák, M. R. Wagner, C. Veit, K. C. Möller, J. O. Besenhard, M. Winter, M. Wohlfahrt-Mehrens, C. Vogler and A. Hammouche, *J. Power Sources*, 2005, **147**, 269–281.

102 J. Reed and G. Ceder, *Chem. Rev.*, 2004, **104**, 4513–4534.

103 L. Wang, T. Maxisch and G. Ceder, *Chem. Mater.*, 2007, **19**, 543–552.

104 F. Lin, I. M. Markus, D. Nordlund, T.-C. Weng, M. D. Asta, H. L. Xin and M. M. Doeff, *Nat. Commun.*, 2014, **5**, 1688–1691.

105 Z. Zhang, D. Fouchard and J. R. Rea, *J. Power Sources*, 1998, **70**, 16–20.

106 K. Hoang and M. D. Johannes, *Chem. Mater.*, 2016, **28**, 1325–1334.

107 R. D. Shannon, *Acta Crystallogr. Sect. A*, 1976, **A32**, 751–767.

108 K. Hoang and M. D. Johannes, *J. Mater. Chem. A*, 2014, **2**, 5224–5235.

109 K. Kang, Y. S. Meng, J. Breger, C. P. Grey and G. Ceder, *Science (80-.).*, 2006, **311**, 977–980.

110 D. Aurbach, B. Markovsky, G. Salitra, E. Markevich, Y. Talyossef, M. Koltypin, L. Nazar, B. Ellis and D. Kovacheva, *J. Power Sources*, 2007, **165**, 491–499.

111 D. R. Gallus, R. Schmitz, R. Wagner, B. Hoffmann, S. Nowak, I. Cekic-Laskovic, R. W. Schmitz and M. Winter, *Electrochim. Acta*, 2014, **134**, 393–398.

112 A. Jarry, S. Gottis, Y. S. Yu, J. Roque-Rosell, C. Kim, J. Cabana, J. Kerr and R. M. Kostecki, *J. Am. Chem. Soc.*, 2015, **137**, 3533–3539.

113 R. Jung, M. Metzger, F. Maglia, C. Stinner and H. A. Gasteiger, *J. Electrochem. Soc.*, 2017, **164**, A1361–A1377.

114 J. Hong, H. Lim, M. Lee, S. Kim, H. Kim, S. Oh, G. Chung and K. Kang, *Chem. Mater.*, 2012, **24**, 2692–2697.

115 J. Cho, Y. J. Kim, T.-J. Kim and B. Park, *Angew. Chemie*, 2001, **113**, 3471–3473.

116 L. Mu, R. Lin, R. Xu, L. Han, S. Xia, D. Sokaras, J. D. Steiner, T. C. Weng, D. Nordlund, M. M. Doeff, Y. Liu, K. Zhao, H. L. Xin and F. Lin, *Nano Lett.*, 2018, **18**, 3241–3249.

117 P.-C. Tsai, B. Wen, M. Wolfman, M.-J. Choe, M. S. Pan, L. Su, K. Thornton, J. Cabana and Y.-M. Chiang, *Energy Environ. Sci.*, 2018, **11**, 860–871.

118 H.-H. Ryu, G.-T. Park, C. S. Yoon and Y.-K. Sun, *Small*, 2018, **14**, 1803179.

119 Z. Chen and J. R. Dahn, *Electrochim. Acta*, 2004, **49**, 1079–1090.

120 W. S. Yoon, K. Y. Chung, J. McBreen and X. Q. Yang, *Electrochem. commun.*, 2006, **8**, 1257–1262.

121 M. T. Dove, in *Introduction to Lattice Dynamics*, Cambridge University Press, Cambridge, 1968, pp. 1–17.

122 H. J. Pain, in *The Physics of Vibrations and Waves*, John Wiley & Sons, Ltd, Chichester, UK, 2005, pp. 1–35.

123 P. Atkins and R. Friedman, *Oxford Univ. Press New York*, 2005, 588.

124 J. Greensite, in *An Introduction to Quantum Theory*, IOP Publishing, 2017, vol. 74, pp. 3–19.

125 M. Hargittai and I. Hargittai, *Symmetry through the eyes of a chemist*, Springer US, Boston, MA, Second edi., 2009.

126 H. S. . Coxeter, *Regular Polytopes*, Dover publications, INC., New York, Third., 1973.

127 A. M. Lesk, *Introduction to Symmetry and Group Theory for Chemists*, 2004.

128 N. J. Everall, in *Handbook of Vibrational Spectroscopy*, ed. J. M. Chalmers, John Wiley & Sons, Ltd, Chichester, UK, 2006.

129 W. G. Fateley, N. T. McDevitt and F. F. Bentley, *Appl. Spectrosc.*, 1971, **25**, 155–173.

130 D. L. Rousseau, R. P. Bauman and S. P. S. Porto, *J. Raman Spectrosc.*, 1981, **10**, 253–290.

131 R. C. Powell, in *Symmetry, Group Theory, and the Physical Properties of Crystals*, eds. W. Beiglbock, J. Ehlers, K. Hepp and H. Weidenmuler, Springer New York, New York, 2010, pp. 1–24.

132 M. T. Dove, in *Introduction to Lattice Dynamics*, Cambridge University Press, Cambridge, 2010, pp. 101–131.

133 G. Keresztury, *Handb. Vib. Spectrosc.*, 2006, 71–87.

134 R. P. Feynman, R. B. Leighton and M. Sands, *The Feynman Lectures on Physics, Vol. II: The New Millennium Edition: Mainly Electromagnetism and Matter*, Basic Books, 2011.

135 R. Ikeda, B. Chase and N. J. Everall, in *Handbook of Vibrational Spectroscopy*, ed. N. J. Everall, John Wiley & Sons, Ltd, Chichester, UK, 2007, pp. 283–303.

136 D. Griffiths and R. College, *Introduction to Electrodynamics*, Prentice Hall, New Jersey, Third., 1999.

137 C. N. Bradwell, *Fundamentals of Molecular Spectroscopy*, McGraw-Hill Book Company Europe, London, 3rd ed., 1983.

138 P. R. Griffiths, in *Handbook of Vibrational Spectroscopy*, eds. J. M. Chalmers and P. R. Griffiths, 2006, pp. 33–43.

139 R. J. H. Clark and T. J. Dines, *Angew. Chemie Int. Ed. English*, 1986, **25**, 131–158.

140 A. E. Douglas, *Discuss. Faraday Soc.*, 1963, **35**, 158.

141 J. L. McHale, in *Handbook of Vibrational Spectroscopy*, ed. P. R. Griffiths, John Wiley & Sons, Ltd, Chichester, UK, 2006.

142 D. P. Strommen and K. Nakamoto, *J. Chem. Educ.*, 1977, **54**, 474.

143 H. Matsuura and H. Yoshida, in *Handbook of Vibrational Spectroscopy*, ed. J. M. Chalmers, John Wiley & Sons, Ltd, Chichester, UK, 2006, vol. 3, pp. 216–234.

144 P. J. Hendra, in *Handbook of Vibrational Spectroscopy*, ed. J. M. Chalmers, John Wiley & Sons, Ltd, Chichester, UK, 2006.

145 M. Gussoni, C. Castiglioni and G. Zerbi, in *Handbook of Vibrational Spectroscopy*, 2006, pp. 2040–2077.

146 R. J. Meier, *Vib. Spectrosc.*, 2005, **39**, 266–269.

147 T. W. Hänsch, G. T. Kamiya, T. F. Krausz, G. B. Monemar, L. H. Venghaus, B. H. Weber and B. H. Weinfurter, *Confocal Raman Microscopy*, Springer Berlin Heidelberg, Berlin, Heidelberg, 2011, vol. 158.

148 N. J. Everall and N. J., *Appl. Spectrosc.*, 2009, **63**, 245A–262A.

149 R. H. Webb, *Reports Prog. Phys.*, 1996, **59**, 427–471.

150 D. Griffiths and R. College, in *Introduction to Electrodynamics*, ed. A. Reeves, Prentice Hall, New Jersey, Third., pp. 392–405.

151 V. Stancovski and S. Badilescu, *J. Appl. Electrochem.*, 2014, **44**, 23–43.

152 Z. Li, J. Huang, Y. Liaw, V. Metzler and J. Zhang, *J. Power Sources*, 2014, **254**, 168–182.

153 F. Poli, J. S. Kshetrimayum, L. Monconduit and M. Letellier, *Electrochem. commun.*, 2011, **13**, 1293–1295.

154 P. Lanz, C. Villevieille and P. Novák, *Electrochim. Acta*, 2013, **109**, 426–432.

155 R. M. Kostecki and F. McLarnon, *Electrochem. Solid-State Lett.*, 2004, **7**, A380.

156 R. E. Ruther, A. F. Callender, H. Zhou, S. K. Martha and J. Nanda, *J. Electrochem. Soc.*, 2014, **162**, A98–A102.

157 K. Tagawa and R. J. Brodd, in *Lithium-Ion Batteries*, Springer New York, New York, NY, 2009, pp. 1–14.

158 K. S. Nanjundaswamy, H. D. Friend, C. O. Kelly, D. J. Standlee and R. L. Higgins, in *IECEC-97 Proceedings of the Thirty-Second Intersociety Energy Conversion Engineering Conference (Cat. No.97CH6203)*, IEEE, vol. 1, pp. 42–45.

159 S. Piller, M. Perrin and A. Jossen, *J. Power Sources*, 2001, **96**, 113–120.

160 J. Lei, F. McLarnon and R. M. Kostecki, *J. Phys. Chem. B*, 2005, **109**, 952–957.

161 P. Lanz, C. Villevieille and P. Novák, *Electrochim. Acta*, 2014, **130**, 206–212.

162 D. Chen, M. A. Mahmoud, J.-H. Wang, G. H. Waller, B. Zhao, C. Qu, M. A. El-Sayed and M. Liu, *Nano Lett.*, 2019, **19**, 2037–2043.

163 J. Felten, H. Hall, J. Jaumot, R. Tauler, A. de Juan and A. Gorzsás, *Nat. Protoc.*, 2015, **10**, 217–240.

164 I. Noda, A. E. Dowrey, C. Marcott, G. M. Story and Y. Ozaki, *Appl. Spectrosc.*, 2000, **54**, 236A–248A.

165 I. Noda, *Biomed. Spectrosc. Imaging*, 2015, **4**, 109–127.

166 M. I. Aroyo, J. M. Perez-Mato, C. Capillas, E. Kroumova, S. Ivantchev, G. Madariaga, A. Kirov and H. Wondratschek, *Zeitschrift fur Krist.*, 2006, **221**, 15–27.

167 C. Julien, *Solid State Ionics*, 2000, **136**–**137**, 887–896.

168 M. Inaba, Y. Iriyama, Z. Ogumi, Y. Todzuka and A. Tasaka, *J. Raman Spectrosc.*, 1997, **28**, 613–617.

169 J. D. Perkins, M. L. Fu, D. M. Trickett, J. M. McGraw, T. F. Ciszek, P. A. Pariila, C. T. Rogers and D. S. Ginley, *MRS Proc.*, 1997, **496**, 329.

170 H. L. Liu, T. Y. Ou-Yang, H. H. Tsai, P. A. Lin, H. T. Jeng, G. J. Shu and F. C. Chou, *New J. Phys.*, 2015, **17**, 103004.

171 E. Flores, N. Vonrüti, P. Novák, U. Aschauer and E. J. Berg, *Chem. Mater.*, 2018, **30**, 4694–4703.

172 A. O. Kondrakov, A. Schmidt, J. Xu, H. Geßwein, R. Mönig, P. Hartmann, H. Sommer, T. Brezesinski and J. Janek, *J. Phys. Chem. C*, 2017, **121**, 3286–3294.

173 C. Ghanty, B. Markovsky, E. M. Erickson, M. Talianker, O. Haik, Y. Tal-Yossef, A. Mor, D. Aurbach, J. Lampert, A. Volkov, J.-Y. Shin, A. Garsuch, F. F. Chesneau and C. Erk, *ChemElectroChem*, 2015, **2**, 1479–1486.

174 X. Zhang, A. Mauger, Q. Lu, H. Groult, L. Perrigaud, F. Gendron and C. M. Julien, *Electrochim. Acta*, 2010, **55**, 6440–6449.

175 K. Ben-Kamel, N. Amdouni, A. Mauger and C. M. Julien, *J. Alloys Compd.*, 2012, **528**, 91–98.

176 H. Koga, L. Croguennec, P. Mannessiez, M. Ménétrier, F. Weill, L. Bourgeois, M. Duttine, E. Suard and C. Delmas, *J. Phys. Chem. C*, 2012, **116**, 13497–13506.

177 G. Gouadec and P. Colomban, *Prog. Cryst. Growth Charact. Mater.*, 2007, **53**, 1–56.

178 A. Tornheim, V. A. Maroni, M. He, D. J. Gosztola and Z. Zhang, *J. Electrochem. Soc.*, 2017, **164**, A3000–A3005.

179 X. Wang, I. Loa, K. Kunc, K. Syassen and M. Amboage, *Phys. Rev. B*, 2005, **72**, 224102.

180 U. Aschauer and N. A. Spaldin, *J. Phys. Condens. Matter*, 2014, **26**, 122203.

181 M. Otoyama, Y. Ito, A. Hayashi and M. Tatsumisago, *J. Power Sources*, 2016, **302**, 419–425.

182 T. Nishi, H. Nakai and A. Kita, *J. Electrochem. Soc.*, 2013, **160**, A1785–A1788.

183 T. Gross and C. Hess, *J. Power Sources*, 2014, **256**, 220–225.

184 T. Itoh, N. Anzue, M. Mohamedi, Y. Hisamitsu, M. Umeda and I. Uchida, *Electrochem. commun.*, 2000, **2**, 743–748.

185 T. Itoh, H. Sato, T. Nishina, T. Matue and I. Uchida, *J. Power Sources*, 1997, **68**, 333–337.

186 M. Okubo, E. Hosono, J. Kim, M. Enomoto, N. Kojima, T. Kudo, H. Zhou and I. Honma, *J. Am. Chem. Soc.*, 2007, **129**, 7444–7452.

187 J.-H. Chung, T. Proffen, S. Shamoto, A. M. Ghorayeb, L. Croguennec, W. Tian, B. C. Sales, R. Jin, D. Mandrus and T. Egami, *Phys. Rev. B*, 2005, **71**, 064410.

188 F. Reynaud, D. Mertz, F. Celestini, J.-M. Debierre, A. M. Ghorayeb, P. Simon, A. Stepanov, J. Voiron and C. Delmas, *Phys. Rev. Lett.*, 2001, **86**, 3638–3641.

189 M. D. Radin and A. Van der Ven, *Chem. Mater.*, 2018, **30**, 607–618.

190 I. Nakai, K. Takahashi, Y. Shiraishi, T. Nakagome and F. Nishikawa, *J. Solid State Chem.*,

1998, **140**, 145–148.

191 A. Rougier, C. Delmas and A. V. Chadwick, *Solid State Commun.*, 1995, **94**, 123–127.

192 C. A. Marianetti, D. Morgan and G. Ceder, *Phys. Rev. B*, 2001, **63**, 224304.

193 A. Hirano, R. Kanno, Y. Kawamoto, Y. Takeda, K. Yamaura, M. Takano, K. Ohyama, M. Ohashi and Y. Yamaguchi, *Solid State Ionics*, 1995, **78**, 123–131.

194 G. X. Wang, S. Zhong, D. H. Bradhurst, S. X. Dou and H. K. Liu, *J. Power Sources*, 1998, **76**, 141–146.

195 Y. W. Tsai, B. J. Hwang, G. Ceder, H. S. Sheu, D. G. Liu and J. F. Lee, *Chem. Mater.*, 2005, **17**, 3191–3199.

196 E. A. Wood, *Cit. J. Appl. Phys.*, 1964, **35**, 1306.

197 H. Sun and K. Zhao, *J. Phys. Chem. C*, 2017, **121**, 6002–6010.

198 Y. Koyama, H. Arai, I. Tanaka, Y. Uchimoto and Z. Ogumi, *Chem. Mater.*, 2012, **24**, 3886–3894.

199 Y. Koyama, N. Yabuuchi, I. Tanaka, H. Adachi and T. Ohzuku, *J. Electrochem. Soc.*, 2004, **151**, A1545.

200 D. Zeng, J. Cabana, J. Bréger, W. Yoon and C. P. Grey, *Chem. Mater.*, 2007, **19**, 6277–6289.

201 E. Levi and D. Aurbach, *Solid State Ionics*, 2014, **257**, 1–8.

202 C. Julien, *Solid State Ionics*, 2002, **148**, 53–59.

203 K. Dokko, M. Mohamedi, N. Anzue, T. Itoh and I. Uchida, *J. Mater. Chem.*, 2002, **12**, 3688–3693.

204 K. Kushida and K. Kuriyama, *Solid State Commun.*, 2001, **118**, 615–618.

205 J. N. Reimers, *J. Electrochem. Soc.*, 1992, **139**, 2091.

206 M. Ménétrier, I. Saadoune, S. Levasseur and C. Delmas, *J. Mater. Chem.*, 1999, **9**, 1135–1140.

207 N. Imanishi, M. Fujiyoshi, Y. Takeda, O. Yamamoto and M. Tabuchi, *Solid State Ionics*, 1999, **118**, 121–128.

208 L. Mendoza, R. Baddour-Hadjean, M. Cassir and J. P. Pereira-Ramos, *Appl. Surf. Sci.*, 2004, **225**, 356–361.

209 M. Nishizawa and S. Yamamura, *Chem. Commun.*, 1998, 1631–1632.

210 R. Baddour-Hadjean and J.-P. Pereira-Ramos, in *Lithium Ion Rechargeable Batteries*, Wiley-VCH Verlag GmbH & Co. KGaA, Weinheim, Germany, 2009, pp. 103–162.

211 P. Novák, J. C. Panitz, F. Joho, M. Lanz, R. Imhof and M. Coluccia, *J. Power Sources*, 2000, **90**, 52–58.

212 B. Andriyevsky, K. Doll and T. Jacob, *Phys. Chem. Chem. Phys.*, 2014, **16**, 23412–23420.

213 S. Kikkawa, S. Miyazaki and M. Koizumi, *J. Solid State Chem.*, 1986, **62**, 35–39.

214 V. R. Galakhov, V. V. Karelina, D. G. Kellerman, V. S. Gorshkov, N. A. Ovechkina and M. Neumann, *Phys. Solid State*, 2002, **44**, 266–273.

215 J. Molenda, A. Stokłosa and T. Bąk, *Solid State Ionics*, 1989, **36**, 53–58.

216 S. Levasseur, M. Menetrier, E. Suard and C. Delmas, *Solid State Ionics*, 2000, **128**, 11–24.

217 J. D. Perkins, C. S. Bahn, J. M. McGraw, P. a. Parilla and D. S. Ginley, *J. Electrochem. Soc.*, 2001, **148**, A1302.

218 N. Kuwata, K. Ise, Y. Matsuda, J. Kawamura, T. Tsurui and O. Kamishima, *Solid State Ionics*, 2012, 138–143.

219 K. Kushida and K. Kuriyama, *Solid State Commun.*, 2001, **118**, 615–618.

220 H. Fukumitsu, M. Omori, K. Terada and S. Suehiro, *Electrochemistry*, 2015, **83**, 993–996.

221 Y. Park, Y. Kim, S. M. Kim, S. Jin, I. K. Han, S. M. Lee and Y. M. Jung, *Bull. Korean Chem. Soc.*, 2017, **38**, 511–513.

222 C. M. Julien and A. Mauger, *AIMS Mater. Sci.*, 2018, **5**, 650–698.

223 C. Snyder, C. Apblett, A. Grillet, T. Beechem and D. Duquette, *J. Electrochem. Soc.*, 2016, **163**, A1036–A1041.

224 Y. Matsuda, N. Kuwata, T. Okawa, A. Dorai, O. Kamishima and J. Kawamura, *Solid State Ionics*, 2019, **335**, 7–14.

225 J. A. Gilbert, V. A. Maroni, Y. Cui, D. J. Gosztola, D. J. Miller and D. P. Abraham, *Adv. Mater. Interfaces*, 2018, **5**, 1701447.

226 Y. Xu, E. Hu, K. Zhang, X. Wang, V. Borzenets, Z. Sun, P. Pianetta, X. Yu, Y. Liu, X.-Q. Yang and H. Li, 2017, **2**, 52.

227 A. Basch, L. de Campo, J. H. Albering and J. W. White, *J. Solid State Chem.*, 2014, **220**, 102–110.

228 G. K. Singh, G. Ceder and M. Z. Bazant, *Electrochim. Acta*, 2008, **53**, 7599–7613.

229 Z. Wang, Z. Wang, W. Peng, H. Guo, X. Li, J. Wang and A. Qi, *Ionics (Kiel).*, 2014, **20**, 1525–1534.

230 X.-Y. Qiu, Q.-C. Zhuang, Q.-Q. Zhang, R. Cao, P.-Z. Ying, Y.-H. Qiang and S.-G. Sun, *Phys. Chem. Chem. Phys.*, 2012, **14**, 2617.

231 F. Sauvage, J.-M. Tarascon and E. Baudrin, *J. Phys. Chem. C*, 2007, **111**, 9624–9630.

232 G. Yang, J. Shi, C. Shen, S. Wang, L. Xia, H. Hu, H. Luo, Y. Xia and Z. Liu, *RSC Adv.*, 2017, **7**, 26052–26059.

233 R. Jung, R. Morasch, P. Karayaylali, K. Phillips, F. Maglia, C. Stinner, Y. Shao-Horn and H. A. Gasteiger, *J. Electrochem. Soc.*, 2018, **165**, A132–A141.

234 A. Grenier, H. Liu, K. M. Wiaderek, Z. W. Lebens-Higgins, O. J. Borkiewicz, L. F. J. Piper, P. J. Chupas and K. W. Chapman, *Chem. Mater.*, 2017, **29**, 7345–7352.

235 W. Li, J. N. Reimers and J. R. Dahn, *Solid State Ionics*, 1993, **67**, 123–130.

236 J. H. Hibben, *Chem. Rev.*, 1936, **18**, 1–232.

237 H.-J. Peng, S. Urbonaite, C. Villevieille, H. Wolf, K. Leitner and P. Novák, *J. Electrochem. Soc.*, 2015, **162**, A7072–A7077.

238 H.-J. Peng, C. Villevieille, S. Trabesinger, H. Wolf, K. Leitner and P. Novák, *J. Power Sources*, 2016, **335**, 91–97.

239 M. Hirayama, K. Sakamoto, T. Hiraide, D. Mori, A. Yamada, R. Kanno, N. Sonoyama, K. Tamura and J. ’ Ichiro Mizuki, *Electrochim. Acta*, 2007, **53**, 871–881.

240 J. Lei, L. Li, R. Kostecki, R. Muller and F. McLarnon, *J. Electrochem. Soc.*, 2005, **152**, A774.

241 C. M. Julien and M. A. Camacho-Lopez, *Mater. Sci. Eng. B*, 2004, **108**, 179–186.

242 S.-M. Bak, K.-W. Nam, W. Chang, X. Yu, E. Hu, S. Hwang, E. A. Stach, K.-B. Kim, K. Y. Chung and X.-Q. Yang, *Chem. Mater.*, 2013, **25**, 337–351.

243 P. Arora, R. E. White and M. Doyle, *J. Electrochem. Soc.*, 1998, **145**, 3647.

244 R. Robert and P. Novák, *J. Electrochem. Soc.*, 2015, **162**, A1823–A1828.

245 D. P. Abraham, R. D. Twesten and M. Balasubramanian, *Electrochem. commun.*, 2002, **4**, 620–625.

246 C. Julien, M. Massot, C. Perez-Vicente, E. Haro-Poniatowski, G. A. Nazri and A.

Rougier, *MRS Proc.*, 1997, **496**, 415.

247 H. Liu, H. Liu, I. D. Seymour, N. Chernova, K. M. Wiaderek, N. M. Trease, S. Hy, Y. Chen, K. An, M. Zhang, O. J. Borkiewicz, S. H. Lapidus, B. Qiu, Y. Xia, Z. Liu, P. J. Chupas, K. W. Chapman, M. S. Whittingham, C. P. Grey and Y. S. Meng, *J. Mater. Chem. A*, 2018, **6**, 4189–4198.

248 W. Li, X. Liu, H. Celio, P. Smith, A. Dolocan, M. Chi and A. Manthiram, *Adv. Energy Mater.*, 2018, **8**, 1703154.

249 J. Peres, F. Weill and D. C., *Solid State Ionics*, 1999, **116**, 19–27.

250 R. Amin, D. B. Ravnsbaek and Y.-M. Chiang, *J. Electrochem. Soc.*, 2015, **162**, A1163–A1169.

251 J. Molenda, P. Wilk and J. Marzec, *Solid State Ionics*, 2002, **146**, 73–79.

252 L. Boulet-Roblin, C. Villevieille, P. Borel, C. Tessier, P. Novák and M. Ben Yahia, *J. Phys. Chem. C*, 2016, **120**, 16377–16382.

253 M. Balasubramanian, X. Sun, X. Q. Yang and J. McBreen, *J. Electrochem. Soc.*, 2000, **147**, 2903.

254 A. O. Kondrakov, H. Geßwein, K. Galdina, L. de Biasi, V. Meded, E. O. Filatova, G. Schumacher, W. Wenzel, P. Hartmann, T. Brezesinski and J. Janek, *J. Phys. Chem. C*, 2017, **121**, 24381–24388.

255 D. Streich, C. Erk, A. Guéguen, P. Müller, F.-F. Chesneau and E. J. Berg, *J. Phys. Chem. C*, 2017, **121**, 13481–13486.

256 C. Tian, D. Nordlund, H. L. Xin, Y. Xu, Y. Liu, D. Sokaras, F. Lin and M. M. Doeff, *J. Electrochem. Soc.*, 2018, **165**, A696–A704.

257 W. S. Yoon, K. Y. Chung, J. McBreen, D. A. Fischer and X. Q. Yang, *J. Power Sources*, 2007, **174**, 1015–1020.

258 K. Kleiner, J. Melke, M. Merz, P. Jakes, P. Nagel, S. Schuppler, V. Liebau and H. Ehrenberg, *ACS Appl. Mater. Interfaces*, 2015, **7**, 19589–19600.

259 R. Robert, C. Bünzli, E. J. Berg and P. Novák, *Chem. Mater.*, 2015, **27**, 526–536.

260 X. Yang, J. Chen, Q. Zheng, W. Tu, L. Xing, Y. Liao, M. Xu, Q. Huang, G. Cao and W. Li, *J. Mater. Chem. A*, 2018, **6**, 16149–16163.

261 N. V Faenza, Z. W. Lebens-Higgins, P. Mukherjee, S. Sallis, N. Pereira, F. Badway, A. Halajko, G. Ceder, F. Cosandey, L. F. J. Piper and G. G. Amatucci, *Langmuir*, 2017, **33**, 9333–9353.

262 R. Qiao, J. Liu, K. Kourtakis, M. G. Roelofs, D. L. Peterson, J. P. Duff, D. T. Deibler, L. A.

Wray and W. Yang, *J. Power Sources*, 2017, **360**, 294–300.

263 J. Eom, M. G. Kim and J. Cho, *J. Electrochem. Soc.*, 2008, **155**, A239.

264 M. Kerlau, M. Marcinek, V. Srinivasan and R. M. Kostecki, *Electrochim. Acta*, 2007, **52**, 5422–5429.

265 R. Jung, M. Metzger, F. Maglia, C. Stinner and H. A. Gasteiger, *J. Phys. Chem. Lett.*, 2017, **8**, 4820–4825.

266 P. K. Allan, N. Louvain and L. Monconduit, in *Prospects for Li-ion Batteries and Emerging Energy Electrochemical Systems*, 2018, pp. 1–55.

267 R. E. Dietz, G. I. Parisot and A. E. Meixner, *J. Appl. Phys.*, 1971, **42**, 1484.

268 L. Maschio, B. Kirtman, M. Rérat, R. Orlando and R. Dovesi, *J. Chem. Phys.*, 2013, **139**, 164102.

269 M. E. A. De Dompablo, C. Marianetti, A. Van Der Ven and G. Ceder, 2001, **63**, 1–9.

270 R. M. Kostecki, J. Lei, F. McLarnon, J. Shim and K. Striebel, *J. Electrochem. Soc.*, 2006, **153**, A669.

271 M. Ebner, D.-W. Chung, R. E. García and V. Wood, *Adv. Energy Mater.*, 2014, **4**, 1301278.

272 L. Jensen, C. M. Aikens and G. C. Schatz, *Chem. Soc. Rev.*, 2008, **37**, 1061–1073.

273 J. F. Li, Y. F. Huang, Y. Ding, Z. L. Yang, S. B. Li, X. S. Zhou, F. R. Fan, W. Zhang, Z. Y. Zhou, D. Y. Wu, B. Ren, Z. L. Wang and Z. Q. Tian, *Nature*, 2010, **464**, 392–395.

274 S. Hy, F. Felix, J. Rick, W.-N. Su and B. J. Hwang, *J. Am. Chem. Soc.*, 2014, **136**, 999–1007.

275 X. M. Lin, Y. Cui, Y. H. Xu, B. Ren and Z. Q. Tian, *Anal. Bioanal. Chem.*, 2009, **394**, 1729–1745.

276 F. Schipper, M. Dixit, D. Kovacheva, M. Talianker, O. Haik, J. Grinblat, E. M. Erickson, C. Ghanty, D. T. Major, B. Markovsky and D. Aurbach, *J. Mater. Chem. A*, 2016, **4**, 16073–16084.

277 A. M. Haregewoin, A. S. Wotango and B.-J. Hwang, *Energy Environ. Sci.*, 2016, **9**, 1955–1988.

278 G. Kresse and J. Hafner, *Phys. Rev. B*, 1994, **49**, 14251–14269.

279 G. Kresse and J. Furthmüller, *Comput. Mater. Sci.*, 1996, **6**, 15–50.

280 G. Kresse and J. Hafner, *Phys. Rev. B*, 1993, **47**, 558–561.

281 J. P. Perdew, K. Burke and M. Ernzerhof, *Phys. Rev. Lett.*, 1996, **77**, 3865–3868.

282 P. E. Blöchl, *Phys. Rev. B*, 1994, **50**, 17953–17979.

283 D. Joubert, *Phys. Rev. B - Condens. Matter Mater. Phys.*, 1999, **59**, 1758–1775.

284 V. I. Anisimov, J. Zaanen and O. K. Andersen, *Phys. Rev. B*, 1991, **44**, 943–954.

285 S. L. Dudarev, G. A. Botton, S. Y. Savrasov, C. J. Humphreys and A. P. Sutton, *Phys. Rev. B*, 1998, **57**, 1505–1509.

286 A. Togo, F. Oba and I. Tanaka, *Phys. Rev. B - Condens. Matter Mater. Phys.*, 2008, **78**, 1–9.

287 A. Fonari and S. Stauffer, *vasp_raman.py*, https://github.com/raman-sc/VASP/, 2013.

288 J. Dahn, U. von Sacken and C. A. Michal, *Solid State Ionics*, 1990, **44**, 87–97.

289 K. Kleiner, D. Dixon, P. Jakes, J. Melke, M. Yavuz, C. Roth, K. Nikolowski, V. Liebau and H. Ehrenberg, *J. Power Sources*, 2015, **273**, 70–82.

Appendix B Supplementary information

B.1 DFT phonon calculations

The density functional theory (DFT) calculations were carried at University of Bern with the VASP code[278–280], using the Perdew-Burke-Ernzerhof exchange correlation functional.[281] Electron-core interactions were described by PAW potentials[282,283] with Li(1s, 2s), Ni(4s, 3p, 3d), Co(4s, 3p, 3d), Mn(4s, 3p, 3d) and O(2s, 2p) and wavefunctions were expanded in plane waves up to a cutoff energy of 500 eV. A Hubbard U[284,285] was applied to the transition metal *d* states with U_{Ni} = 6.70 eV, U_{Co} = 4.91 eV and U_{Mn} = 4.89 eV.[106] The reciprocal space of the 8-atoms-cell of LCO and LNO was sampled using Γ-centred meshes with dimensions 6×6×6 for the rhombohedral structure and 10×10×2 for the monoclinic structure. NCM111 was modelled with an antiferromagnetic order with up spins on Ni and down spins on Mn, and using a 108-atom hexagonal cell with a = b = 8.68 Å and c = 14.35 Å, for which the reciprocal space was sampled with a Γ-centred 2x2x1 mesh. All internal and cell degrees of freedom were relaxed until forces converged below 10^{-3} eV/Å and stresses below $5 \cdot 10^{-3}$ eV/Å^3. Phonon frequencies were computed using the frozen phonon method as implemented in the *phonopy* package.[286] The mode intensities were computed from the mode-dependent change in dielectric constant[287] evaluated via finite differences for mode amplitudes of ±0.01 Å and dielectric constants computed using density functional perturbation theory.

B.2 Temperature-dependent Raman spectra of $LiNiO_2$ powder

The low-temperature Raman spectra of the $LiNiO_2$ powder (Sigma-Aldrich, Germany) was recorded using a Renishaw inVia Raman microscope and a LINKAM heating/freezing stage equipped with a heat-conducting silver block and an optically-transparent glass window. Once the powder was introduced in the cooling stage, the stage was closed and purged with N_2 gas for avoiding vapor water freezing during the experiment. The stage was placed below the microscope lenses and connected to an electronic controller and a cryogenic container with liquid-nitrogen. The controller stabilizes the flow of liquid nitrogen to the silver block in order to attain the desired temperature. The temperature at the powder was reduced in multiple steps. After several minutes at each targeted temperature, the Raman spectrum of the powder was recorded using an x50 (0.50 NA) objective lens, 633 nm excitation laser and a grating with 1800 lines/mm grove density. All temperature-dependent spectra were recorded on the same particle.

B.3 Geometry of oxygen's coordination shell from the LE-DFT structure

The bond distances and angles between angles via a custom-made Matab-based script using as inputs the Cartesian positions of atoms in the optimized LE-DFT structure. All the calculated values are shown in Figure B3.

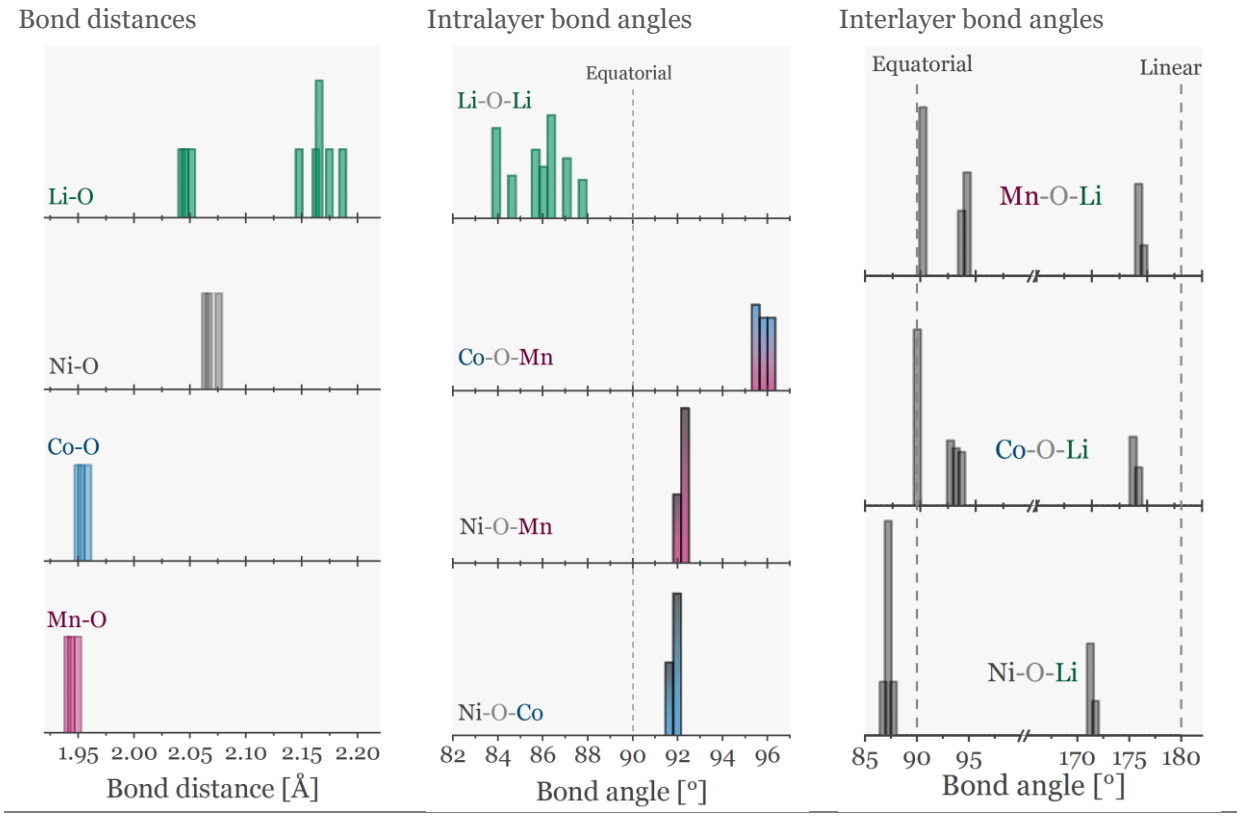

Figure B3. Bond distances and angles computed from the LE-DFT structure.

The Ni-O, Co-O and Mn-O distances feature narrow distributions centered on 2.07, 1.95 and 1.94 Å, respectively. The Li-O distances distribute bimodally with a narrow portion at 2.04 Å and a broader portion centered around 2.17 Å. An analysis of the unit cell shows that Li are 2.04 Å away from the O linearly connected to Ni, while they are 2.17 Å away from O linearly connected to Co and Mn. The emerging trend suggests that the Li-O bonds attempt keeping the linear M-O-Li distances constant. The intralayer angles — formed between oxygen and a pair of atoms within the same layer — are obtuse (>90 °) when subtended between M-O-M, and all Li-O-Li angles are acute (< 90°). In addition, the Co-O-Mn angles centred at 96° are significantly wider than the rest. In general, wider angles are found for atoms more proximal to oxygen. The intralayer angles — subtended between oxygen and an atoms in the upper and another in the lower layer — feature the same trends: long Ni-O distances result into acute (<90°) Ni-O-Li equatorial angles while short Mn-O and Co-O distances result into

obtuse (>90°) Co-O-Li and Mn-O-Li equatorial angles. In the same plot, the angles close to 180° are subtended between atoms at opposite sides of oxygen, and so they are not perfectly linear. Opposing Ni-O-Li are the most deformed as their angles center at 171°.

B.4 Wavelength-dependent Raman spectra of $LiMO_2$ powders

The wavelength-dependent Raman spectra of $LiMO_2$ powders (Table 4.3) were acquired with a Renishaw inVia confocal microscope with an x50 (0.50 NA) objective lens. Excitation laser wavelengths of 785, 633 and 532 nm were used with gratings of 1200, 1800, and 1800 lines/mm grove density, respectively. Each measurement was performed using the attenuation filter where no sample burning occurred (typically above 95% attenuation). The spectra of an oxide at the three excitation wavelengths were recorded from the same particle.

B.5 Diffuse-reflectance UV-Vis spectra of $LiMO_2$ powders

The spectra of the powder samples (Table 4.3) were acquired in diffuse-reflectance mode using a Varian Cary 4000 UV-Vis spectrophotometer, scanning within the 300-800 nm range at 300 nm/min. All spectra were referenced against a $BaSO_4$ powder standard.

B.6 Electrochemical profiles of Ni-rich oxides composite electrodes

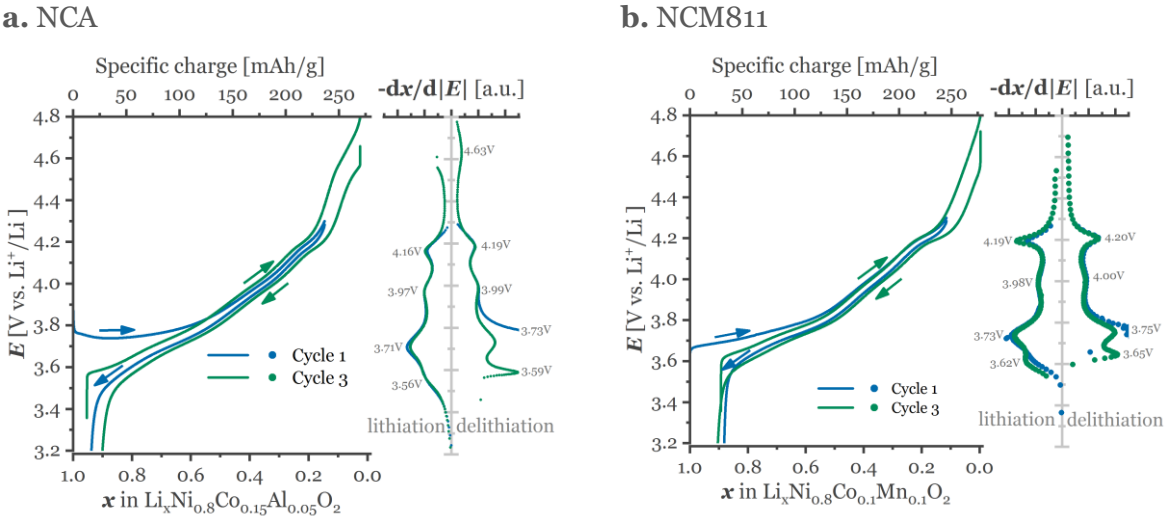

Figure B6. Constant-current and differential charge profiles of **a.** NCA and **b.** NCM811 during the first (3.0–4.3 V *vs.* Li^+/Li) and third overcharge cycle (3.0–4.8 V *vs.* Li^+/Li).

B.7 Raman spectrum of spinel-like surface layers

The characterization of delithiated and thermally treated $LiMO_2$ oxides was performed neither with binder nor conductive additives, since the thermal decomposition of these additives introduce measurement artefacts. An approximated amount of 20 mg of powder of active material was homogeneously distributed in the bottom of the cell, forming a powder disc limited by the cell walls. A first Celgard separator (Ø17 mm) was carefully placed on top of the powder disc avoiding displacing the powder, followed by the addition of a second Celgard separator. Subsequently, 200 µl of LC30 electrolyte were slowly added near the cell bottom and next to the cell wall, ensuring that the droplets adhere to the wall before soaking the powder. Later, the insulating cylinder and the Li-metal disc (0.2 mm thick, Ø12 mm) were slowly pushed onto the wet separator. The cell was closed and the powders were galvanostatically delithiated at 200 µA until reaching 190 mAh/g, which represents around 70% Li^+ per formula depending on the oxide. Subsequently, the cell was disassembled leaving the delithiated powder inside. The powder was washed with DMC solvent and the resulting suspension was taken out from the cell, poured onto a watch-glass, and left for some minutes until the powder precipitated. The excess DMC was removed and the powder was left drying for some minutes before recovery and storing for characterization or pre-treatment.

The washed powder was heated in a thermogravimetric analysis equipment up to 500 °C with a heating rate of 10 °C/min. Figures B7a and b show the spectrum of the pristine and electrochemically polarized powders, respectively. The strong and sharp Raman bands of the polarized powder sample (Figure B7b) confirm that it has been successfully delithiated despite the absence of electrode additives. When the delithiated powder is heated to 500 °C its Raman spectrum transforms dramatically, as shown in Figure B7c. The spectral envelope appears intense, broad and features a maximum at 530 cm^{-1}. The asymmetric shape of the envelope suggests the existence of several, highly convoluted bands that require at least three Lorentz-type profiles for good fitting. Notably, there are no features in the 600 cm^{-1} spectral region that can be compared to the bands that appear during cycling in Figure 7.3. For this reason, the supplementary characterization of the heated sample is further pursued for confirming whether it has actually transformed into the oxygen-deficient phases. Figure 7.4d shows the powder X-ray diffraction pattern of the heated sample, indexed according to Dahn et al.[288] The $I_{006/102}/I_{101}$ intensity ratio evidences severe cation disorder (25% Ni in Li sites), while the merging of the 10$\underline{8}$ and 110 peaks at 2θ=64.15° confirms the formation of a disordered, spinel-like phase.[242] Therefore, we discard that the Raman bands of delithiated NCA above 600 cm^{-1} originate from a surface spinel-like interphase, after demonstrating that their Raman bands are not comparable.

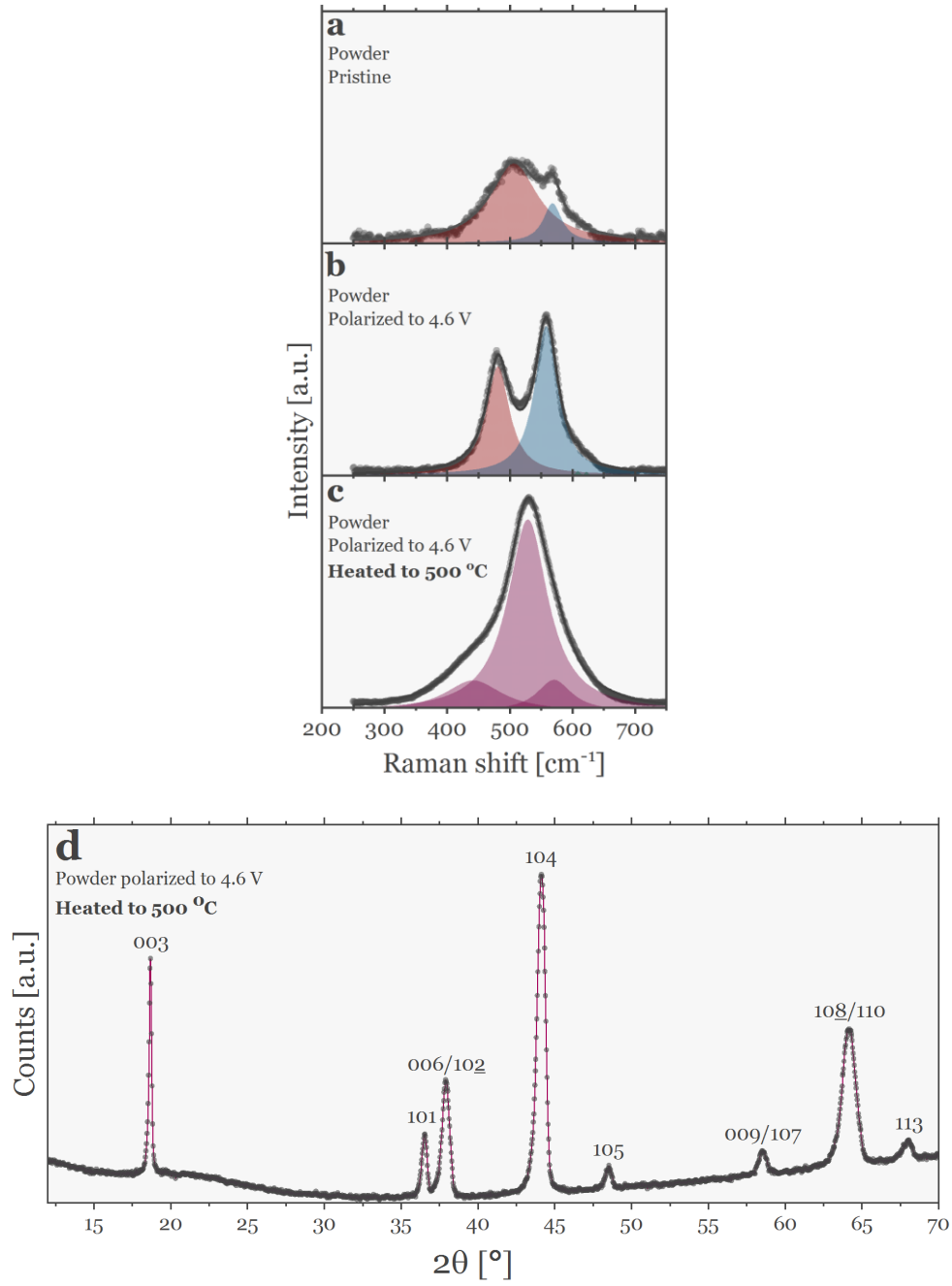

Figure B7. Thermally-induced degradation of NCA. Raman spectrum of **a.** pristine NCA powder, **b.** the same powder electrochemically polarized to 4.6 V *vs.* Li^+/Li, **c.** the polarized powder heated at 500 °C. **e.** XRD pattern of the polarized and heated powder.

B.8 DFT calculations on delithiated Li_xMO_2

DFT calculations on lithiated and partially delithiated $LiMO_2$ are performed employing the same methodology specified in section B1. Ideally, the phonons and their Raman activity should be calculated from a DFT-relaxed NCA lattice. Recreating NCA's random distribution

of 80% nickel, 15% cobalt and 5% aluminium would require the use of big unit cells demanding a prohibitively high computational cost. The next best substitute lattice to model is $LiNiO_2$; given the high Ni content of NCA the two lattices are expected to be chemically comparable. However, $LiNiO_2$ relaxes to a monoclinic $C2/m$ lattice (section 5.4.1) that does not represent the one experimentally found on NCA. Even if $LiNiO_2$ is constrained to relax to a $R\bar{3}m$ lattice symmetry with higher energy, the electronic structure becomes metallic; i.e. adopts an inherently different bonding that deviates from the semiconductor nature of NCA. $LiCoO_2$ is another unsubstituted oxide that could potentially serve as a lattice model of NCA. The DFT-calculated LCO lattice naturally relaxes to a $R\bar{3}m$ space group with a non-zero band gap; hence, agreeing structurally and electronically with the properties of NCA.

B.9 Crystallographic lattice parameters and Raman band frequencies of NCA

Figure B9 compares the trends in the E_g and A_{1g} peak positions with crystallographic and electronic-related parameters that evolve during cycling. The *operando* crystallographic lattice parameters were obtained from reference [259]. The distances and angles were computed from the crystallographic lattice parameters assuming that the space group and the *z*-position of oxygen in NCA remain constant during charge. Those assumptions are supported by experimental data.[244,259] Using a developed Matlab script, the Wyckoff positions of each atom expressed in terms of the *a* and *c* lattice parameters are transformed to Cartesian coordinates using an appropriate transformation matrix. Then, the differences in Cartesian atomic positions r(O) – r(M) are computed, and the norm of the resulting vectors yield the M-O distances. Likewise, the O-M-O angles are computed using the inner product formula. The calculated (Ni/Co)-O bond distances agree very well with the values and trends obtained by other XRD and EXAFS measurements,[289] which also validate the computed O-M-O angles form which there is no reference data.

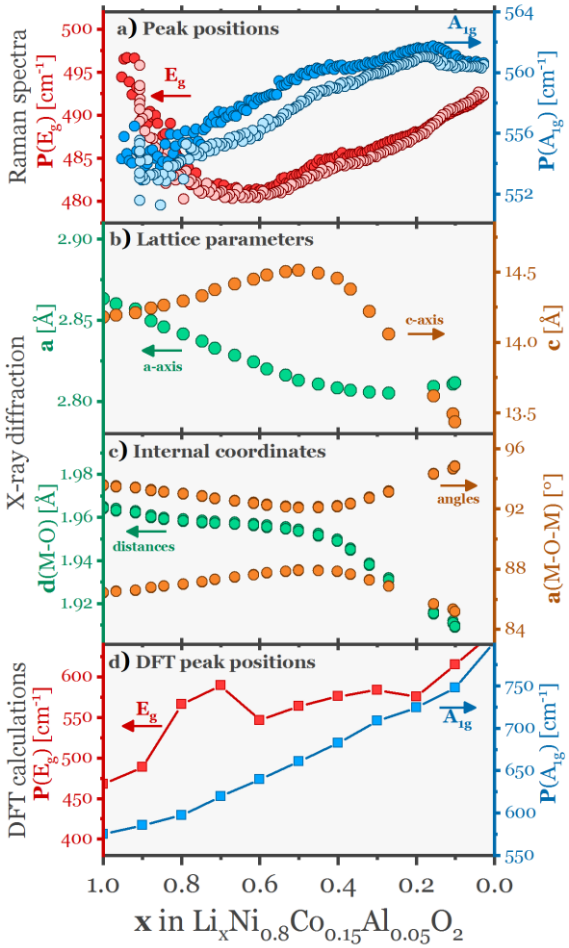

Figure B9. **a.** *Operando* trends of the E_g and A_{1g} peak positions (Figure 10.2a) compared with **b.** the *operando* crystallographic lattice parameters of NCA, **c.** the internal coordinates computed from the crystallographic data, and **d.** the DFT-phonon frequency changes resulting from the artificial oxidation of the lattice.

Delithiation of NCA causes the general increase of $P(A_{1g})$ up to x=0.2 and an U-shape $P(E_g)$ trend with minimum at x=0.7. In contrast, the lattice parameters inflect at different SOL. The c-axis parameter trend changes slope at x=0.5 and the a-parameter trend reaches minimum at x=0.3. Furthermore, there is no clear correlation between lattice expansion/contraction and frequency shifts to lower/higher wavenumbers. The vibrational modes can be alternative expressed as displacements along internal coordinates,[125] i.e. the A_{1g} mode as a M-O stretching and the E_g mode as a M-O-M bending.[202] Figure B9c shows that delithiation promotes the continuous contraction of the M-O distances, and thus the trend can be tentatively related to the increase of $P(A_{1g})$. However, at x=0.5 such contraction accelerates dramatically without leaving any noticeable signature in the $P(A_{1g})$ trends. Also at x=0.5 the M-O-M angles reach their maximal approach to the ideal 90°, but at this x the $P(E_g)$ trends do not feature any inflection. Therefore, we demonstrate that the vibrational frequencies

are unrelated to the crystallographic trends, and thus they rather reflect short-ranged variations of the oxygen environment.

Since the crystallographic lattice parameters fail in describing the trends on *P*, the lattice models based on DFT phonon calculations are used, which make explicit consideration of interatomic forces. During delithiation, the oxygen environment experiences the depletion of neighbouring Li^+ and the oxidation of neighbouring M. In the physical system these processes occur simultaneously in order to keep the lattice electroneutral. However, the DFT calculations enable the possibility of artificially oxidize M without removing Li^+, and thus explore the individual effect that electron depletion alone has on $P(E_g)$ and $P(A_{1g})$. Figure B9d shows that artificial oxidation promote a frequency increase of both E_g and A_{1g} modes. Considering the Ni-rich nature of these oxides, the Fermi level is expected to be at antibonding eg^* states (section 2.1). Hence, electron removal from these states strengthen the M-O bonds,[81] and thus the displacements of oxygen atoms are restored more strongly, resulting in higher vibration frequencies.

However, Figure 7.4 shows that when $LiMO_2$ is oxidised and delithiated, $P(E_g)$ decreases by 18 cm^{-1} between $1.0 > x > 0.5$, roughly agreeing with experimental observations ($\sim$16 cm^{-1}, Figure 7.4). In the same SOL range the experimental trends and the calculations agree: $P(A_{1g})$ barely changes. In brief, DFT calculations show that M oxidation raises $P(E_g)$ but a concomitant delithiation lowers $P(E_g)$ and correctly predict the extent of the wavenumber shift. Consequently, we believe that the U-shaped $P(E_g)$ trend experimentally observed in Figure 7.5 results from a crossover of two phenomena: an initial bond softening due to V_{Li} formation ($x > 0.7$) and a later continuous bond hardening due to the oxidation of M. Interpreting variations on vibrational frequency requires an explicit consideration of the material's electronic structure defining bonding and interatomic interactions.

B.10 Fitted peak intensities of NCA bands above 600 cm^{-1}

The fitted peak heights of the two NCA bands observed above 600 cm^{-1} (Figure 7.3) are shown in Figure B10. There is negligible peak height for $x>0.6$; after, they grow following a sigmoidal-like trends which are highly reversible during the first cycle but develop hystereses during the following cycles.

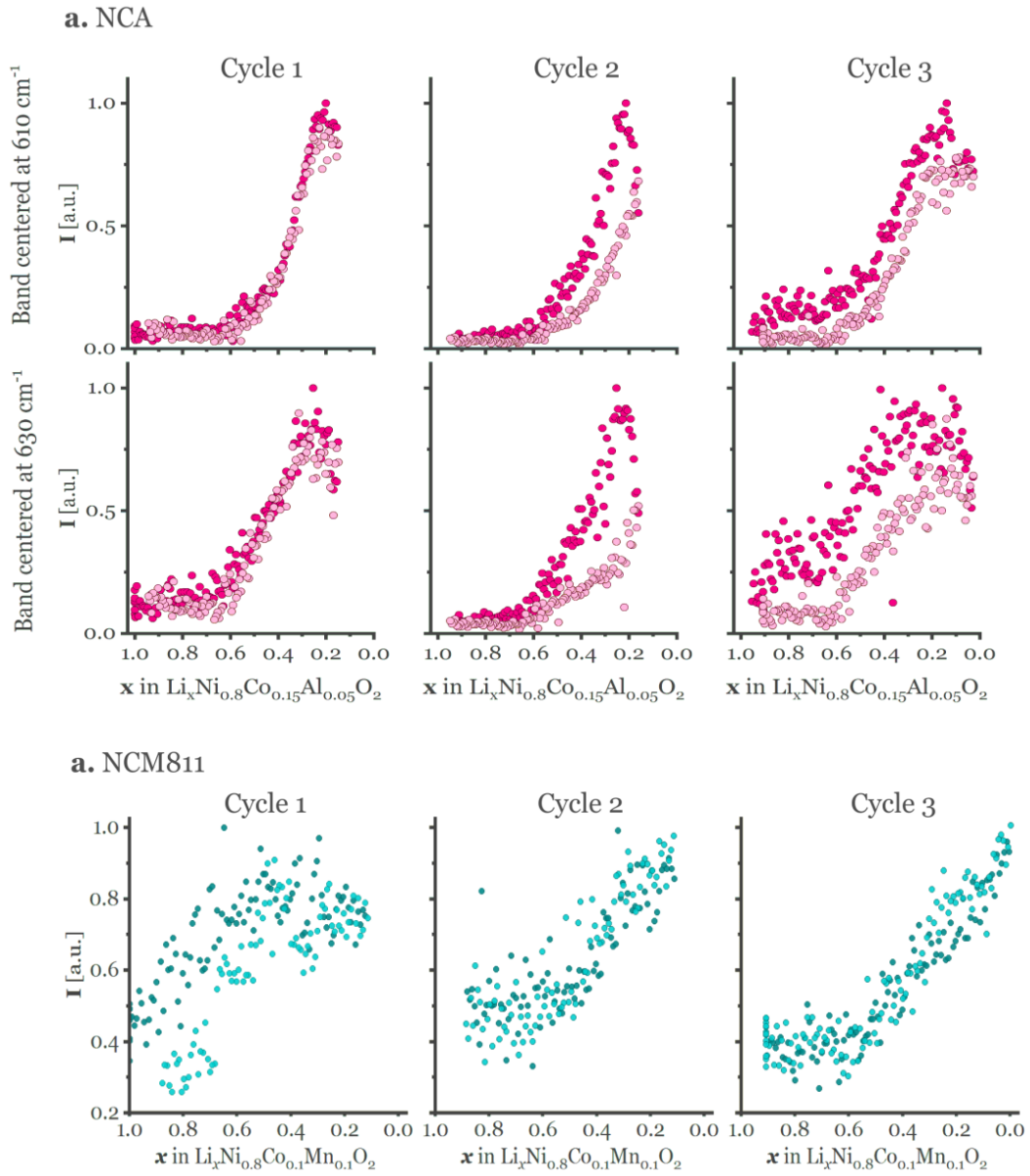

Figure B10. Peak intensities of **a.** NCA and **b.** NCM8111 bands above 600 cm^{-1} during three full cycles. Dark dots draw the spectral tend during delithiation, while light dots during re-lithiation.

B.11 Online electrochemical mass spectrometry (OEMS)

The OEMS setup operated with a quadrupole mass spectrometer (QMS 200, Pfeiffer) for partial pressure measurements, a pressure transducer (PAA-33X, Keller Druck AG) for total cell pressure, temperature, and internal volume determination, stainless steel gas pipes and Swagelok fittings (3-mm compression tube fittings, Swagelok) to connect the OEMS cell, a set of solenoid valves (2-way magnetic valve, Series 99, silver-plated nickel seal, Parker), and a scroll pump (nXDS15i, EDWARDS GmbH) for efficient flushing. The magnetic valves were

electronically controlled with a solid state relay module (NI 9485 measurement System, National Instruments) connected to a computer with a LabView Software (NI Labview 2013, National Instruments). For partial pressure and gas evolution rate analysis 1.3 mL of gas was extracted from the headspace (~4 mL) of the cell and replaced by pure Ar (quality 5.0). Calibration gas bottles were utilized to relate the MS ion-current signals at m/z = 32 and 44 to known concentrations of O_2 and CO_2 (1000 ppm in Ar), respectively, before and after the measurement.

B.12 Electrochemical profiles of NCM111 and NCM622 composite electrodes

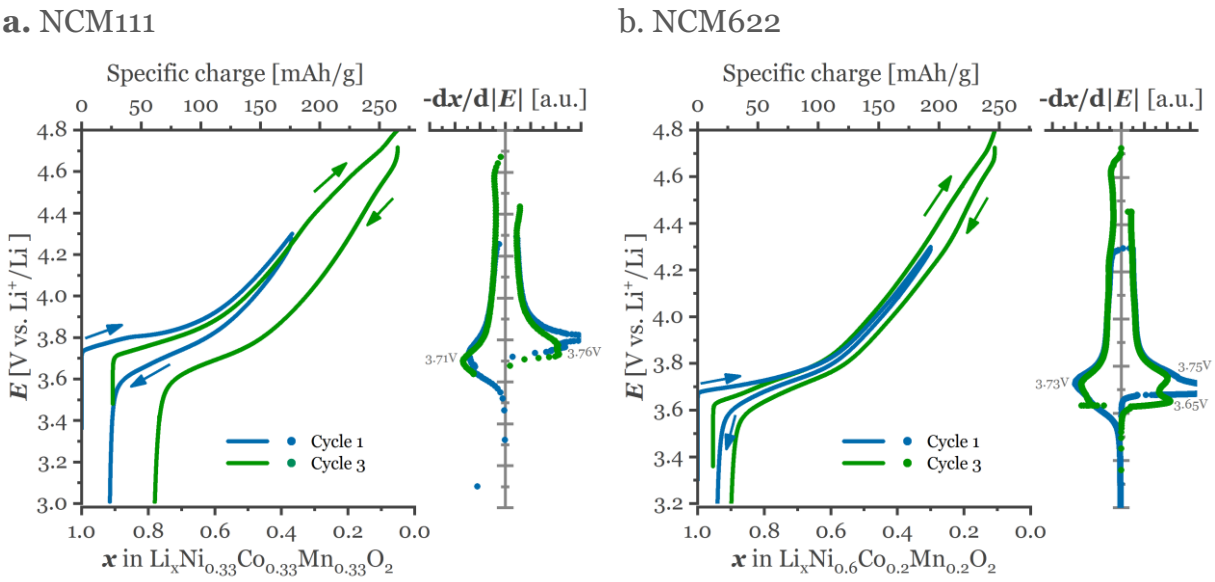

Figure B12. Constant-current and differential charge profiles of **a.** NCM111 and **b.** NCM622 during the first (3.0–4.3 V *vs.* Li⁺/Li) and third overcharge cycle (3.0–4.8 V *vs.* Li⁺/Li).

B.13 Fitted peak positions of NCM622

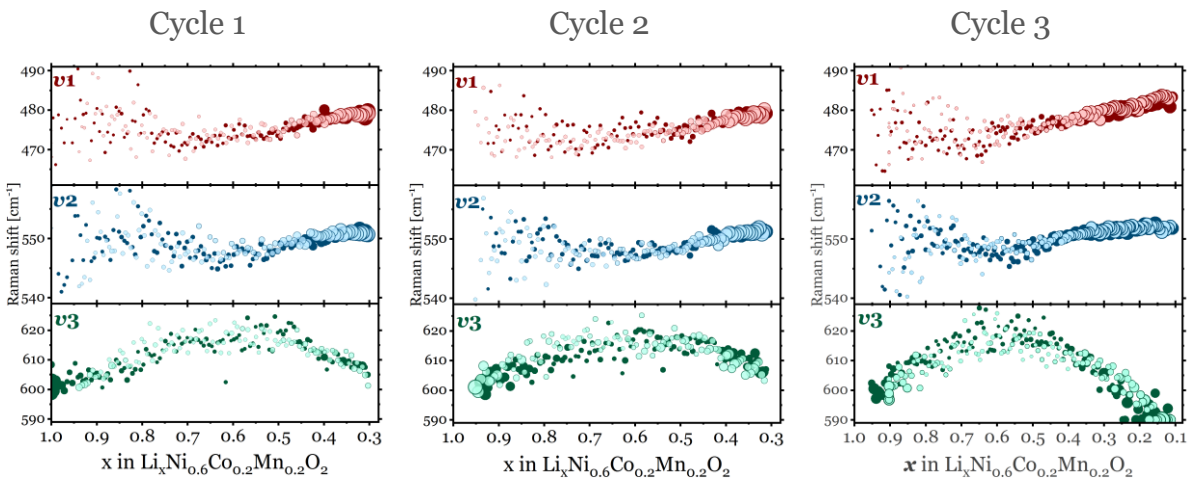

Figure B13. Fitted band positions of *v1* (red), *v2* (blue) and *v3* (green) bands of NCM622 as a function of SOL, during two standard cycles (3.0-4.3 V) and a third overcharge (3.0-4.8 V) cycle. The size of the dots is scaled to the intensity of the band, highlighting thus regions of weak peak intensity that result in scattered peak position trends.